



UNIVERSITY OF
LIVERPOOL

School of Engineering

PhD Thesis

Polarisation dependent NUV femtosecond laser Inscription
of high grade Volume Bragg Gratings in
poly(methyl)methacrylate
with a spatial light modulator

Thesis submitted in accordance with the requirements of
the University of Liverpool for the degree of Doctor of Philosophy

By

Lingyi Ye

School of Engineering

University of Liverpool

Brownlow Street

Liverpool

L69 3GH

UK

October 2014

Abstract

Parallel near-ultraviolet (NUV) beam, 387nm femtosecond laser pulses with linear and circular polarisations were used to inscribe high efficiency Volume Bragg Gratings (VBGs) in clinical grade poly(methyl)methacrylate (PMMA) with the aid of a Spatial Light Modulator (SLM). Large, high quality VBGs with dimensions of 5mm x 5mm in size with (1-7)mm thickness and 20 μ m pitch were created at high speed, fabricated in 36 minutes, showing a first order diffraction efficiency $\eta_1 > 94\%$ with 4mm thickness. This is the highest diffraction efficiency observed to date in the undoped polymer, PMMA. Linear polarisation produced a higher refractive index contrast than circular polarisation, was found to be due to polarisation dependent non-linear filamentation, initiated through self-focusing. Using the threshold for supercontinuum, the ratio of critical power for self-focusing in PMMA was measured to be $P_c^{\text{lin}}/P_c^{\text{circ}} \sim 1.5$, in accord with theoretical expectations.

The pulse energy uniformity of the multiple beams was also dramatically improved by a camera based feedback system which was integrated into a LabVIEW based hologram calculation and display system, reducing the non-uniformity of parallel NUV and NIR beams significantly, thus improving the inscription process.

Declaration

I hereby declare that all of the work contained within this dissertation has not been submitted for any other qualification.

Signed:

Date:

Acknowledgements

I am using this opportunity to express my gratitude to everyone who supported me throughout the time of my PhD.

Above all, I would like to thank my parents for their selfless financial support and endless encouragement. My girlfriend, Doris Lu, has given me her unequivocal support throughout the four years to my daily life.

I sincerely acknowledge my supervisors, Prof. Ken Watkins, Dr. Geoffrey Dearden and Dr. Stuart Edwardson from the University of Liverpool. This work would not have been possible without their help and support. I am thankful to Dr. Walter Perrie, sophisticated in laser micro-processing, for his advice and patience for this research and thesis. I also gratefully acknowledge Dr Dun Liu, former PhD student in Laser Group, enlightened me with new research ideas.

I would like to acknowledge everyone from the laser group of the University of Liverpool and Lairdside Engineering Centre who helped me for this research, particularly, Dr Eamonn Fearon, Dr. Zheng Kuang, Mr Doug Eckford, Dr Liwei Fu, Mr Yang Jin and Mr. Jinglei Ouyang.

List of publications to date

Journal papers:

1. L.Ye, W. Perrie, O. Allegre, Y. Jin, Z. Kuang, P. Scully, E. Fearon, D.Eckford, S. Edwardson and G.Dearden, "NUV femtosecond laser inscription of volume Bragg gratings in poly (methyl) methacrylate with linear and circular polarisations" *Laser Physics*, December 2013, 23(12)

Conference contributions:

1. Dun Liu, L. Ye, Walter Perrie, Olivier Allegre, E. Fearon, S. P. Edwardson, and G. Dearden "Ultrafast laser internal structuring of materials with a spatial light modulator" *International Laser Applications Symposium 2013*, Nottingham UK, Micro-processing session.
2. Lingyi Ye, Walter Perrie, O. Allegre, E. Fearon, S. P. Edwardson, and G. Dearden , "Femtosecond Inscription of Volume Phase Gratings in Poly(methyl)methacrylate and Effects of Polarisation Inscription" *Advanced Solid-State Lasers, A*, Paris France, October 27, 2013 - November 1, 2013, Poster Session III (JTh2A)
3. Lingyi Ye, G Zhu, W Perrie, Z Zhai, D Liu, O. Allegre, E. Fearon, P. Scully and G.Dearden "Filamentation in poly(methyl) methacralate with linear, circular, radial and azimuthal polarization with vortex wavefronts" *Photon 2014*, London UK, September 2014, Poster Session II(p.18).

Contents

List of figures	IX
List of tables.....	XV
List of symbols.....	XVI
List of abbreviations	XVIII
Chapter 1 Introduction.....	1
1.1 Background and motivation.....	2
1.2 Contributions of this thesis.....	4
1.3 Overview of this thesis.....	5
Chapter 2 Literature review.....	7
2.1 Introduction.....	8
2.2 Laser-material processing by femtosecond laser.....	9
2.2.1 Femtosecond laser machining of metals.....	9
2.2.2 Femtosecond laser machining semiconductors.....	11
2.2.3 Femtosecond laser internal processing dielectrics.....	11
2.2.3.1 Femtosecond laser induced refractive index modification.....	15
2.2.3.2 Femtosecond laser induced filamentation.....	16
2.3 Effects of processing conditions.....	20
2.3.1 Laser parameters.....	20
2.3.2 Focusing conditions.....	27
2.3.3 Material Properties.....	32
2.4 Femtosecond laser producing Volume Bragg Gratings(VBGs)	33
2.4.1 Introduction to VBGs.....	33
2.4.2 Traditional methods of femtosecond laser inscription of VBGs.....	35

2.4.3 Femtosecond laser writing Bragg grating in PMMA.....	39
2.5 Laser parallel processing technique.....	40
2.5.1 Introduction to spatial light modulator (SLM)	40
2.5.2 Algorithms for calculating computer generated hologram (CGHs).....	42
2.5.3 Parallel Femtosecond laser internal structuring with SLM.....	45
2.5.4 Optimization of CGHs.....	48
2.5.4.1 Improvement of algorithms.....	48
2.5.4.2 Asymmetric beam designs.....	50
2.5.4.3 Camera based optimisation.....	52
2.6 Polarisation dependent filamentation.....	54
2.6.1 Critical Power for Self-focusing (SF) and Supercontinuum (SC)	54
2.6.2 Polarisation dependent critical power.....	57
2.6.3 Numerical Solution of SF.....	57
 Chapter 3 – NUV multiple laser beam parallel writing of VBGs in	
PMMA.....	60
3.1 Introduction.....	61
3.2 Equipment.....	62
3.3 Material.....	65
3.4 Experimental setup.....	66
3.5 Diffraction efficiency measurement for VBGs.....	66
3.6 Multiple Laser Beam Direct Writing of VBGs.....	68
3.7 Measured Diffraction efficiency.....	71
3.8 Thickness dependence of volume gratings.....	73
3.9 Bragg angular envelope of volume grating	76
3.10 Time dependence of volume gratings.....	77
3.11 Creation of VBGs with high density	79

3.12 Summary.....	80
Chapter 4 Polarisation dependent filamentation.....	82
4.1 Introduction.....	83
4.2 Effect of polarisations on writing VBGs at 387nm.....	83
4.3 Experimental setup.....	88
4.3.1 Femtosecond laser polarisation modulation.....	89
4.3.2 Measurement of white light continuum.....	91
4.4 Polarisation dependent critical pulse energy for SC.....	92
4.5 Effects of polarisation on transmitted energy in internal processing.....	96
4.6 Effects of polarisation on transmitted pulse energy through PMMA at 775nm.. ..	98
4.7 Polarisation dependent critical power for filamentation in fused silica at 387nm.....	100
4.8 Effects of polarisation on transmitted pulse energy through fused silica at 387nm.....	101
4.9 Discussion.....	102
4.10 Summary.....	106
Chapter 5 Optimisation of energy uniformity of multiple laser beams.....	104
5.1 Introduction.....	109
5.2 Equipment.....	109
5.2.1 CCD Camera.....	109
5.2.2 Modification of LabVIEW software.....	111
5.3 Experimental setup.....	112
5.4 Introduction to the software.....	113

5.4.1 Creation of beam arrays.....	114
5.4.2 Calculation of holograms.....	116
5.4.3 Methods of feedback	116
5.4.4 Algorithm of optimisation.....	117
5.4.5 Critical value.....	119
5.4.6 Factor m.....	120
5.5 Optimisation of 10 × 10 beam array.....	121
5.6 Auto-tracking of multiple beams.....	125
5.7 Pulse energy optimisation at NUV wavelength for filamentation in PMMA.....	130
5.8 Pulse energy optimisation at NIR wavelength for surface ablation.....	132
5.9 Discussion.....	134
5.10 Summary.....	135
Chapter 6 Conclusions and future work.....	136
6.1 Conclusion.....	137
6.2 Recommendations for future work.....	138
References.....	140

List of figures

Fig. 2.2-1 Laser material interactions for nanosecond and ultrashort pulse lasers

Fig. 2.2-2 Schematic of the multiphoton excitation in PMMA and in fused silica

Fig. 2.2-3 CCD images of the accumulated laser scattering and plasma fluorescence signals

Fig. 2.2-4 Induced structures in PMMA by NUV (387 nm) and NIR (775 nm) laser pulses

Fig 2.3-1: (a) Effects of the pulse duration on the refractive index change threshold and the breakdown threshold. (b) Effects of the pulse energy on the refractive index change at the different pulse duration. (c) Effects of the pulse duration on the filament length

Fig. 2.3-2: Dependence of grating diffraction efficiency on pulse duration and number of pulses per spot

Fig. 2.3-3 Length of filamentary refractive index change and position of filamentary refractive index change in PMMA for different pulse energies

Fig. 2.3-4 Thresholds of induced refractive-index change in fused silica at different repetition rates.

Fig. 2.3-5 Schematic of the damage processes induced by (a) focussing and (b) internal self-focussing

Fig. 2.3-6: Focussing through an air/dielectric interface with a high NA objective.

Fig. 2.3-7 Calculated maximum axial intensity I_{max} as a function of focusing depth for different NA's.

Fig. 2.3-8(a) Width and (b) Depth of the cross-sectional structures as a function of the focusing depth below the PMMA surface

Fig. 2.4-1 Schematic of a readout beam passing through a grating

Fig. 2.4-2 Schematic diagram of femtosecond laser focused by a pair of cylindrical lenses

Fig. 2.4-3 Schematic setup for inscription of VBGs using a cylindrical lens and a phase mask

Fig. 2.5-1 Typical structure of a LCSLM.

Fig. 2.5-2 Generation of a phase hologram with the GS Algorithm

Fig. 2.5-3 Experimental setup for femtosecond laser parallel processing by using SLM

Fig. 2.5-4 (a) Original and (f) optimized MPFL. (b), (g) Respective computer reconstructions. (c), (h) Respective optical reconstructions. (d), (i) Transmission microscope and (e), (j) AFM images of the fabricated area.

Fig.2.5-5 10 Diffraction efficiency of a series of gratings of varying thickness and comparison with Kogelnik's theory

Fig. 2.5-6: Cross sections of the gratings written by 16 beams with symmetric pattern and asymmetric pattern showing improved uniformity.

Fig.2.5.7. Holographic femtosecond laser processing system

Fig. 2.5.8. Changes of the uniformity and the total SH intensity

Fig. 2.6-1 Seed beam , white-light continuum spectra of sapphire and fused silica

Fig. 2.6-2 Plasma emission images recorded for various pump pulse durations and various polarisation states

Fig. 2.6.3 Cross-section of the femtosecond laser induced filaments with pulse energy

Fig. 3.1-1 Asymmetric multi-beam pattern for parallel processing.

Fig. 3.2-1 Output Beam profile of the femtosecond laser system, Clark-MXR CPA 2010.

Fig. 3.2-2: (a) Labview interface (b) The CGH generated using the GS algorithm

Fig. 3.4-1 Schematic of the experimental setup for NIR parallel processing

Fig. 3.5-1 Schematic of measuring the diffraction efficiency of volume gratings

Fig. 3.6-1 Schematic of multi-beam modification to create continuous volume phase grating by stitching filamentary modifications

Fig. 3.6-2 (a) (b) Front view and (c) cross-sectional view of a thick VBG written with 10 parallel NUV beams.

Fig. 3.7-1 Image of Bragg diffraction at $\lambda = 532 \text{ nm}$

Fig. 3.8-1(a) Diffraction efficiency of gratings with various thickness and developing time (b) theoretical fit based on Kogelnik Theory with fit parameter Δn .

Fig. 3.9-1 The Bragg angular envelope of the 5mm thick VBG measured at 532nm.

Fig. 3.10-1 The time dependence of the refractive index modification

Fig. 3.11-1 Parallel writing inside PMMA.

Fig. 4.2-1 Time dependence of ratio $\eta_1(|V\rangle)/\eta_1(|R\rangle)$

Fig. 4.2-2 Image of (a) the cross-section of polarisation dependent filamentation in PMMA inscribed by 387nm with various polarisation states (b) filament length induced by laser with linear $|V\rangle$ and circular $|R\rangle$ polarisation states

Fig. 4.3-1 Schematic of the experimental setup for NIR parallel processing at various polarisation states

Fig. 4.3-2 Selection of hologram and waveplate orientations for generating 6 polarisation states.

Fig. 4.3-3. Spectrum of the 775nm femtosecond laser ($1\mu\text{J}$) detected by the spectrometer.

Fig. 4.3-4 Experimental setup for the analysis of the continuum generation by 775 nm pulses at various polarisations.

Fig. 4.4-1 Spectrum of 775nm femtosecond laser $|V\rangle$ (black) and the induced SC in PMMA at 2000nJ pulse energy (red)

Fig. 4.4-2 Left wing of the spectrum of the SC

Fig. 4.4-3 Integrated pulse energy, distributed from 750nm to 760nm in the spectrum of the SC

Fig.4.5-1 Cross-section of the filaments in PMMA induced by 775nm fs laser

Fig. 4.6-1 Absorption rate of focused NIR femtosecond laser by PMMA

Fig.4.6-2 Comparison of filament length and pulse energy absorption

Fig.4.7-1 Cross-section of filaments induced by 387nm fs laser in fused silica

Fig. 4.8-1 Absorption rate of focused NIR fs laser (387nm) by fused silica with various pulse energy and polarisations states

Fig. 5.2-1 Interface of the Beamgage software

Fig. 5.2-2 The reprogrammed LabView interface

Fig. 5.3-1 Schematic of the experimental setup for NUV parallel processing with camera based feedback and optimization system

Fig. 5.4-1 The flowchart of the software, composed of three main modules

Fig. 5.5-1 The design and optimisation results of 100 NIR beams in LabView software

Fig. 5.5-2 Charts showing the pulse energy uniformity with time.

Fig. 5.5-3 The Standard Deviation/Mean of the theoretical uniformity and experimental uniformity before and after the utilisation of feedback system

Fig. 5.6-1 The demonstration of auto-tracking function

Fig. 5.6-2 Optimisation of dynamic beam designs changing every 20-30 seconds

Fig.5.7.1 (a)(b) and (c)(d) illustrate the pulse energy of the 100 diffracted NIR beam array before and after optimisation both in 2D and 3D format. (e) and (f) show the Surface micro-machining of a stainless steel substrate.

Fig. 5.8-1 (a) Geometric and orientation of the filaments (b) the internal micro-machining inside PMMA clearly demonstrates the improvement in uniformity with the 10 spot array

List of tables

Table 2.3-1 Diffraction efficiencies of gratings fabricated under various conditions

Table 2.3-2 Femtosecond laser refractive index modification in various glass with different compositions and properties

Table 2.5-1 Summary of theoretical performances of investigated algorithms.

Table 2.5-2 Summary of experimental performances of investigated algorithms

Table 2.6-1 Anti-stokes broadening and key data measured at $P=1.1P_{th}$: minimum beam diameter at focus d_{min} , maximum fluence F_{max} and energy loss E_{loss} . P_{th} is accurate within $\pm 20\%$

Table 3.2-1 Specifications of the SLM

Table 4.2-1 1st order diffraction efficiencies 9 days after inscription with different polarisations

Table 5.2-1 Specifications of the CCD camera

List of symbols

T_e	K	Electron temperature
k	cm^2s^{-1}	Diffusivity
F	Jcm^{-2}	Laser fluence
E_b	eV	Bandgap energy
E_p	J	Focal length
I	Wcm^{-2}	Laser intensity
$\alpha(\lambda)$	cm^{-1}	Absorption coefficient
λ	nm	Wavelength
$\chi^{(3)}$	esu	Third order susceptibility
n_0	n/a	Refractive index of material
E_p	J	Focal length
n_2	cm^2/W	Nonlinear Refractive index
k	cm^{-1}	Wave number
L	mm	Grating thickness
ρ_e	cm^{-3}	Plasma density
NA	n/a	Numerical Aperture
n_e	cm^{-3}	Electron density
P	W	Laser power
P_c	W	Critical power
Q	n/a	Grating thickness parameter
θ_b	degree	Bragg angle
Δn	n/a	Refractive index change

ΔX	μm	Offset in X direction
$\Delta\theta$	degree	Angular sensitivity of volume gratings
φ	radians	desired phase
ψ	n/a	light field
η	n/a	Diffraction efficiency
η_1	n/a	1 st order diffraction efficiency
Λ	μm	Grating Period
Z_f	μm	Self-focusing length

List of abbreviations

BBO	beta- BaB ₂ O ₄
CGH	Computer Generated Hologram
DE	Diffractive efficiency
FWHM	Full Width Half Maximum
GS	Gerchberg-Saxon
MPA	Multiphoton absorption
NA	Numerical Aperture
NIR	Near Infrared
NUV	Near Ultra-violet
RI	Refractive index
VBGs	Volume Bragg Gratings
SF	Self-focusing
SC	Supercontinuum
SDM	Standard deviation over mean
SLM	Spatial light modulator
RMR	Range to Mean Ratio

Chapter 1

Introduction

1.1 Background and motivation

Femtosecond lasers offer unique advantages during the internal structuring of transparent materials through ultrahigh intensity induced nonlinear multi-photon absorption. Due to the localized refractive index modification with limited thermal effect on the surrounding material, ultrafast lasers are widely used to fabricate various photonic devices such as waveguides and splitters with flexible 3D structures. For example, the bulk refractive index modification of the polymeric material, poly(methyl methacrylate), PMMA, is attractive for potential applications in clinical biology and chemistry since PMMA is harmless in the human body. While milli-joule pulse energy is typically available with commercial kilohertz Ti:sapphire femtosecond laser systems, only submicro-joule pulse energy is required for the refractive index modification process, resulting in a very low pulse energy utilization $< 0.1\%$. In order to increase the throughput and efficiency, multi-beam parallel processing with the aid of a Spatial Light modulator (SLM) is proposed and demonstrated.

A Spatial Light Modulator, (SLM), addressed with Computer Generated Holograms (CGH's) can be used to correct wave-front aberrations, alter temporal pulse shape, modify an intensity distribution or split an energetic laser beam into many diffracted spots with arbitrary designs in 2D or 3D. By using the CGHs to create a large number of diffracted beams of the requisite pulse energy, processing efficiency can be significantly increased by more than an order of magnitude. In this research, a Liquid Crystal on Silicon (LCoS) phase only SLM is

used to generate parallel beam arrays for direct, fast inscription of high efficiency Volume Bragg Gratings (VBGs) inside clinical grade PMMA. Therefore, the fabrication time is significantly reduced while the utilization of available laser pulse energy increases accordingly.

However, the pulse energy uniformity of the multi-beams can still be unsatisfactory due to the limitations of the algorithms for calculating CGHs. High quality device fabrication demands good multiple beam uniformity. To optimize this uniformity, a feedback system has been developed within a LabVIEW environment by measuring and analysing the pulse energy of each diffracted beam collected by a camera and applying an error signal based on the energy differences in real time.

The incident polarization of the inscribing femtosecond laser beam has been previously shown to have significant effect in the laser internal structuring of transparent dielectric materials such as fused silica but has not been studied in polymers. Consequently, we have investigated the effects of polarization on the laser-matter interaction in PMMA and glasses, studying effects such as self-focusing (SF), filamentation and refractive index change.

The main objectives of this thesis are:

- 1) To apply SLM generated multiple NUV beams for femtosecond laser internal refractive index (RI) structuring of PMMA to rapidly create a range of VBGs with diffraction efficiency approaching unity.

- 2) To investigate the effect of laser beam polarization on filamentation and hence refractive index (RI) modification in PMMA and other transparent materials.
- 3) To optimise the pulse energy uniformity of SLM generated multi-beams by using a new feedback system to optimise CGH's and hence improve inscription.

1.2 Contributions of this thesis

This thesis is the first study to produce high quality, high efficiency, device level VBGs in pure PMMA using uniform parallel NUV femtosecond laser beams inscribed with different polarisations. As diffraction efficiency depended on inscription polarisation, the effects of laser polarisation on laser Supercontinuum (SC), self-focusing (SF) and refractive index modification were investigated thoroughly in PMMA.

Since CGH's, generated within a LabVIEW program still suffer from significant beam non-uniformity, a method of real-time feedback and optimization system was developed in LabVIEW to improve the pulse energy uniformity of multi-beams generated by an SLM. The original multi-beam profile was collected by a camera integrated within LabVIEW to recalculate the energy weight of each diffracted beam and thus create new, optimised holograms which significantly improved the uniformity of multi-beams.

1.3 Overview of this thesis

Chapter 2 commences with the introduction of relevant background regarding femtosecond laser-matter interaction inside transparent materials and mechanisms of refractive index modification, followed by a review of the application of multiple beam processing by using an SLM. The effects of polarisation on laser induced refractive index modification in different materials are discussed and demonstrated.

Chapter 3 focuses on producing high quality VBGs using optimized multiple NUV beams generated by the SLM. Detailed optical analysis and theoretical modelling are also presented.

Chapter 4 presents experimental results of the polarization dependent filamentation in PMMA using linear and circular polarization states by measuring the critical power for SC and SF and the observed length of induced filaments. The effect of polarisation on refractive index inscription and hence device efficiency can thus be explained.

Chapter 5 begins with the illustration of the flow chart relevant to the software package for calculating and optimizing holograms by analysing beam profile image captured by the camera, followed by a demonstration of the multi-beam auto-tracking system. The optimization of uniformity of NIR and NUV multiple beams are presented with ablation test on stainless steel and internal processing inside PMMA.

Finally, Chapter 6 states the novelties and the contributions of his research and concludes with suggestions for potential improvements and ideas for future work.

Chapter 2

Literature review

This chapter presents the literature review relating to this research project. Firstly, the basic theory and the mechanisms of internal structuring transparent material by femtosecond laser are explained followed by the effects of different process parameters including the laser parameter, focus conditions and the material effects. Then, the parallel processing technique by using a spatial light modulator (SLM) and its applications in femtosecond laser based internal structuring will be demonstrated after an introduction to the calculation algorithm of computer generated holograms (CGH) and the related optimization techniques will be shown. The final part will discuss the effects of laser polarization in femtosecond induced SF in transparent material.

2.1 Introduction

Since the invention of the laser in 1960 by Theodore Maiman^[1], there has been a constant development in laser technology towards shorter temporal pulse lengths. The introduction of the intracavity Q switch allowed pulse lengths around 10ns ^[2,3] while the technique of cavity mode-locking brought down pulse lengths to the picosecond and femtosecond region^[4,5]. Today, commercial picosecond (ps) and femtosecond (fs) laser systems are routinely used in the laboratory. Precision laser micromachining is usually carried out with short-pulse lasers with nanosecond (ns), as well as ps and fs laser pulses. Recently, sub-femtosecond optical pulses, termed attosecond (10^{-15} s) have also been developed for applications such as strobing real-time electron motion in plasma^[6]. Other micro-structuring that involves material conditioning (annealing,

surface texturing, hardening, etc.) and laser assisted growth are typically carried out with longer pulses or with CW lasers.

Ultra short pulse laser micro-structuring of materials is a relatively new research field which emerged in the middle of 1990s. One of the earliest applications of fs laser pulses to processing was carried out by P.P.Pronko et al^[7] who used a Ti: sapphire laser with a pulse length of 200fs and wavelength of 800nm to drill holes with a diameter of 300nm on thin metal films. Following this demonstration, the significance of ultra-short pulse lasers for applications in micro-structuring of materials was further recognized by researchers throughout the world.

2.2 Laser-material processing by femtosecond laser

Femtosecond lasers are widely applied not only to surface structuring and ablation but also to internal inscription of transparent materials, which is initiated by multi-photon absorption. This technique has extended internal micro-structuring of optical materials to almost all transparent dielectrics including glasses ^[8-12] and polymers ^[13-22].

2.2.1 Femtosecond laser machining of metals

Metals have high conduction band electron densities ($n_e \sim 10^{23} \text{cm}^{-3}$), hence have high absorption coefficient $\alpha \sim 10^6 \text{cm}^{-1}$ so that absorption occurs in the skin layer with depth $d \sim 1/\alpha \sim 10 \text{nm}$. Metals absorb laser energy due to inverse

bremstrahlung phenomenon. During inverse Bremsstrahlung, a free electron at the bottom of the conduction band is accelerated and moves to the conduction band with higher energy states. Following the inverse bremsstrahlung, energy is fast relaxed within the electronic subsystem. Then, electrons couple the energy through electron-phonon collisions leading to lattice heating followed by heat diffusion on longer timescales. With fs pulses, the electron temperature T_e can exceed the lattice temperature greatly at short timescales, much shorter than electron-phonon coupling time (\sim few ps), before the temperatures of electron and lattice converge to thermal equilibrium.

As shown in Fig. 2.2-1, ns laser melts and evaporates the material, yielding a rough ablated surface while surface exposure is also complicated by plasma absorption. For femtosecond laser, as heat diffusion is limited during the pulse to a distance $D = (2k\tau_{e-ph})^{1/2}$, (k = diffusivity, $0.1 - 1\text{cm}^2\text{s}^{-1}$ in metals), ultrashort pulse ablation minimises heat diffusion during the pulse, and avoids plasma absorption. Thus, more energy is transmitted to the surface leading to higher temperatures and lower ablation threshold than with ns pulses, generating more evaporation and less melt. Therefore, the shape of the ablation conforms to the beam with negligible melt provided the fluence is maintained in the low regime, typically $F < 10 F_{th}$.

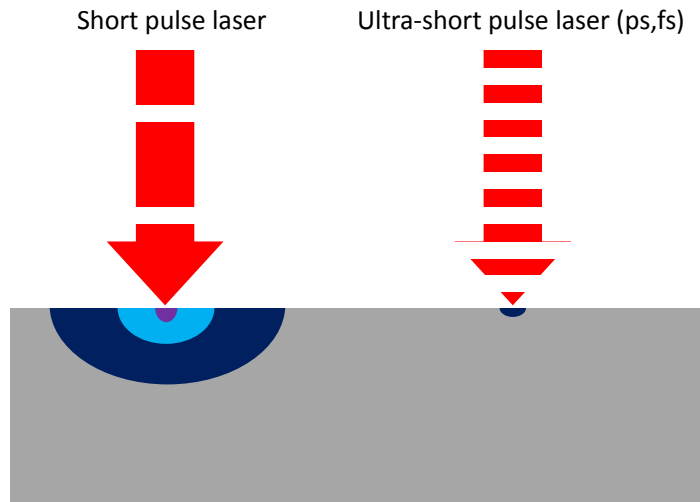


*Fig. 2.2-1 Laser material interaction basic for ns and ultrashort pulse lasers
(heating effect: purple>blue>dark blue)*

2.2.2 Femtosecond laser machining semiconductors

Semi-conductors typically have low density of free electrons in the conduction band. If the photon energy $h\nu > E_b$, the bandgap, one photon absorption is sufficient to raise the electron to the conduction band. When illuminated by femtosecond laser, the leading edge of a pulse generates large number of electrons in the conduction band causing the material to behave as a metal. As a result, the processing for these materials is similar to that for metals. On the other hand, if the photon energy $h\nu < E_b$, absorption can still take place at ultrahigh intensity $I > 10^{12} \text{Wcm}^{-2}$ by non-linear multi-photon absorption, multi-photon absorption (MPA) where $n h\nu > E_b$, where n is the quantity of photons. Competition between linear and non-linear absorption can also occur.

2.2.3 Femtosecond laser internal processing dielectrics

The dielectrics have a large electronic band gap E_b hence no free electrons in the conduction band. The optical bandgaps of transparent materials, a critical property in femtosecond laser transparent material inscription which range from 2.2-2.4 eV for chalcogenide glasses^[24] to 9eV for fused silica^[25]. Based on Ti-sapphire wavelength operating near 800nm (peak of the gain), the photon energy $h\nu(800\text{nm}) \sim 1.5\text{eV} < E_b$ so dielectrics are transparent to incoming fs pulses. Therefore, only MPA is generally involved in this process while linear absorption is essentially negligible. At ultrahigh intensity, MPA is the relevant mechanism to create electrons in the conduction band.

For a photon energy lower than the band-gap energy E_g , a femtosecond laser with low intensity transmits through the material without energy absorption. On the other hand, at high laser intensities ($I > 10^{12}\text{W}/\text{cm}^2$), nonlinear absorption of photons takes place via multi-photon^[25] or tunnelling effects^[26], followed by an avalanche mechanism^[27] leading to strong ionization.

Multi-photon absorption is the simultaneous absorption of n identical photons where $n h\nu > E_b$ exciting an electron from the valance band to the conduction band. The multi-photon ionization is a high order effect, several orders of magnitude weaker than linear absorption which strongly depends on the laser intensity^[28].

The absorption coefficient can be expanded as ,

$$\alpha(\lambda) = \alpha_1(\lambda) + \alpha_2(\lambda)I + \alpha_3(\lambda)I^2 + \dots + \alpha_n(\lambda)I^{n-1} \quad \text{Eq. 2-1}$$

where $\alpha_n(\lambda)$ is the n-photon absorption coefficient. Linear absorption is proportional to $\alpha_1(\lambda)$, when the material is transparent, $\alpha_1(\lambda) \sim 0$. 2-photon absorption proportional to $\alpha_2(\lambda)I^2$, is relevant when the energy of 2 photons $2E_p$ exceeds the band-gap. If $2E_p$ is not enough to get over band-gap, $\alpha_3(\lambda)I^3$ may be relevant and so on. As non-linearity grows, higher $\alpha_n(\lambda)I^n$ couples the valence to conduction band. For example, in fused silica (band-gap $\sim 9\text{eV}$), MPA was shown to be proportional to I^6 at 800nm wavelength. As shown in Fig 2.2-2, the band gap of the PMMA $E_g = 4.58\text{eV}$ needs simultaneously absorption of 3 photons at a wavelength $\lambda = 775\text{ nm}$ (1.55eV) or 2 photons at $\lambda = 387\text{ nm}$ (3.2eV) in order to be promoted to the conduction band.

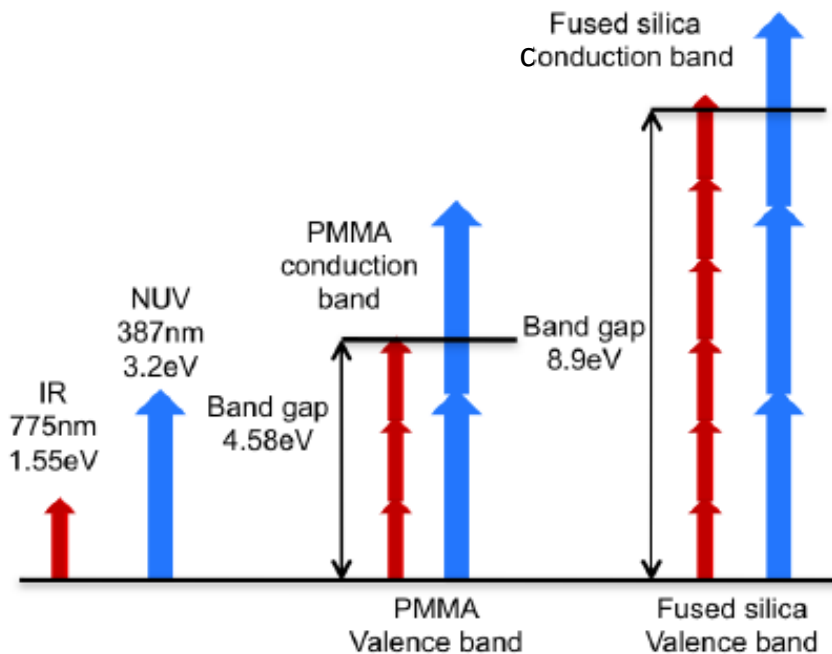


Fig. 2.2-2 Schematic of the multiphoton excitation of an electron in PMMA and fused silica from the valence to the conduction band.

In tunnelling ionisation, the strong electric field of the laser pulse reduces the Coulomb potential energy barrier and allows an electron to quantum mechanically tunnel from the valance band to the conduction band. Although these two nonlinear processes compete at ultra-high intensities, multiphoton ionisation generally dominates over tunnelling in femtosecond laser interaction with transparent materials.

In avalanche ionisation, laser energy is absorbed by electrons through the inverse Bremsstrahlung followed by impact ionisation. During inverse Bremsstrahlung, a free electron at the bottom of the conduction band is accelerated and moves to the conduction band with higher energy states. When its total energy exceeds the bandgap energy E_b plus the conduction band minimum, this electron can ionise another one from the valance band, producing two electrons near the conduction minimum. These electrons can be accelerated by the intense field and repeat the process, resulting in an avalanche in which the free electron density increases exponentially with time. The transparent material becomes locally absorbing, when the electron density exceeds a critical value^[41].

With a femtosecond laser pulse, the peak intensity is ultra-high, which leads to significant multi-photon ionisation. When the intensity exceeds a threshold value, unbound electrons are produced in the focal volume and act as seeds for avalanche ionisation in a deterministic manner^[29]. Hence, the energy deposition process and subsequent structural change are well controlled and highly reproducible, thus enabling precision material modification at a sub-micron

scale.

The other important property of the transparent material related to the laser – matter interaction is the comparatively low thermal diffusion coefficient typically $10^{-4}\text{cm}^2/\text{s}$ while it is $0.1 - 1\text{cm}^2/\text{s}$ for metals ($1\text{cm}^2/\text{s}$ for gold).

2.2.3.1 Femtosecond laser induced refractive index modification

With pulse energy higher than the laser material damage threshold, a focused fs laser induces permanent damage such as voids or cracks in the focus volume, where micro-cracks or voids form. The permanent voids in bulk transparent materials have attracted special attention for their potential applications in three-dimensional optical storage, photonic crystal and integrated optics^[30-32]. With lower laser pulse energy, refractive index modification can be produced and the material keeps the original optical quality. The localized refractive index modification through nonlinear multi-photon absorption gives rise to the fabrication of a wide range of optical devices such as VBGs, optical couplers and optical storage ^[30,33,34]. The formation of the refractive index modification in crystalline materials is attractive and still under investigation.

In PMMA, A. Baum et al^[35] have shown that the refractive index change induced by a 387nm femtosecond laser in PMMA involves direct cleavage of the polymer backbone and propagation via chain unzipping under formation of monomers. Depending on the writing conditions, both positive ^[35] and negative^[14] refractive index change can be produced.

In fused silica, the formation of refractive index change likely derives from the mechanisms such as rearrangement of the network of chemical bonds^[36], heat accumulation with melting and subsequent re-solidification^[37] and colour centre formation^[38]. However, the relative contribution of these and other unknown mechanisms is still under investigation.

2.2.3.2 Femtosecond laser induced filamentation

Filamentation or self-guiding by intense femtosecond laser pulses has been observed in various transparent bulk material^[22], liquids^[39], and gases^[40]. The filament induced by femtosecond lasers involves complex non-linear processes including SF, multi-photon absorption, pulse steepening and self-phase modulation and generally leads to a super-continuum, depending on the material band-gap^[41]. Self-guiding is the result of the dynamic balance between SF and plasma defocusing while effects such as chromatic dispersion are expected to be much less important^[42]. This leads to spatial confinement over distances much greater than the characteristic Rayleigh length. When a Gaussian laser pulse of peak intensity I (Wcm^{-2}) with a plane wavefront passes through a transparent dielectric (Kerr) medium, the refractive index n_0 is modulated instantaneously to $n = n_0 + n_2 I$ where n_2 is the non-linear RI component generated through the third order susceptibility $\chi^{(3)}$. As the pulse propagates, the phase delay on axis is greater than at the pulse edge hence an instantaneous lens is formed, leading to SF if the peak power exceeds the critical power, given by^[135],

$$P_c = \left[\frac{\pi(0.61)^2 \lambda_0^2}{8n_0 n_2} \right] \quad \text{Eq. 2-2}$$

overcoming diffraction. Theoretically, SF would lead to a singularity but is prevented from doing so by plasma de-focusing. As the intensity increases, non-linear MPI generates seed electrons in the conduction band, followed by impact ionization, hence a free electron plasma with density $\rho_e(t)$ grows exponentially (highest density ρ_e on axis). This creates a negative lens which balances the SF, leading to confinement of the radiation in a filament, where the ultrahigh intensity is clamped.

For example, filamentation was investigated in fused silica by Salimina et al^[43]. A fs laser with 810nm wavelength, 45 fs pulse length and 1 kHz repetition rate was focused by various lenses with different NAs ranging from 0.03 to 0.83. Referring to Fig. 2.2-3 with low NA, the starting point of the refractive index change moved towards the laser source with the pulse energy increasing. Filaments with length up to 2 mm were observed. However, with a high NA lens of 0.85, no filamentation was generated, thus a high NA focusing defeats filamentation.

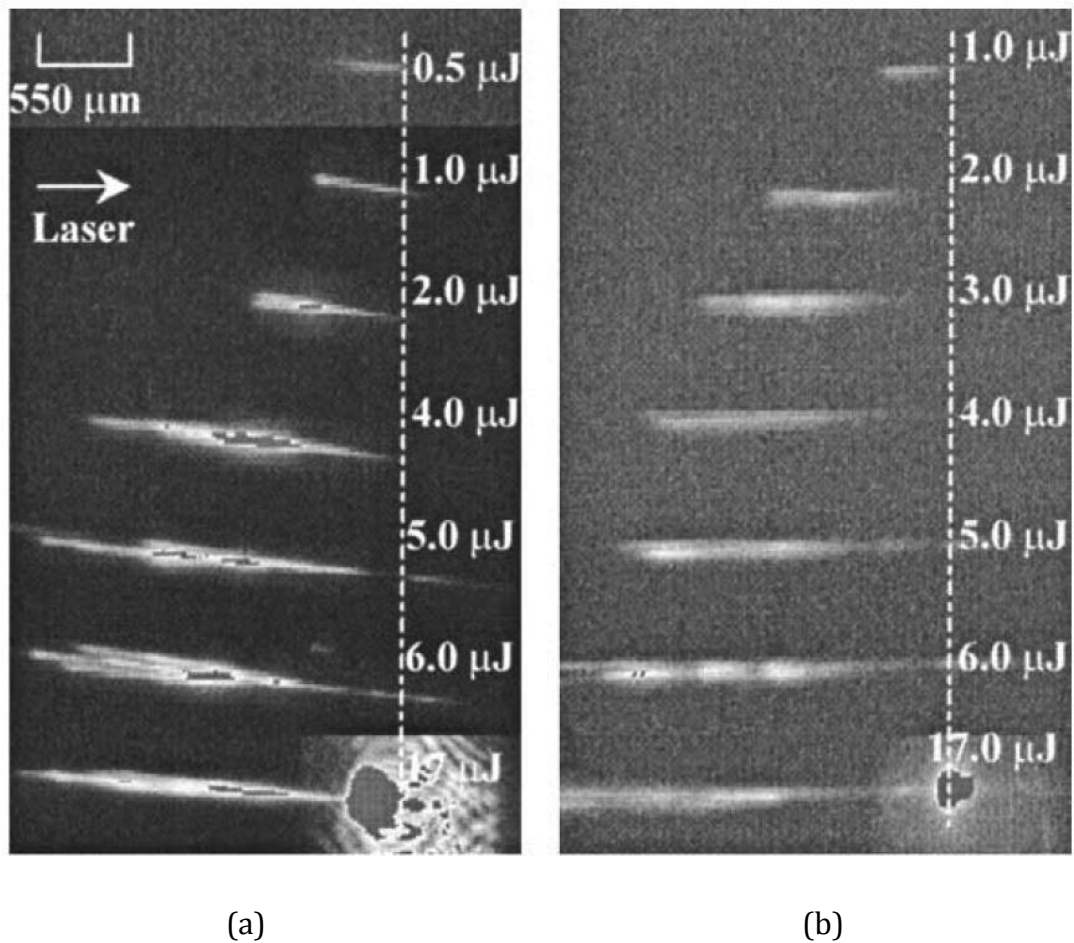
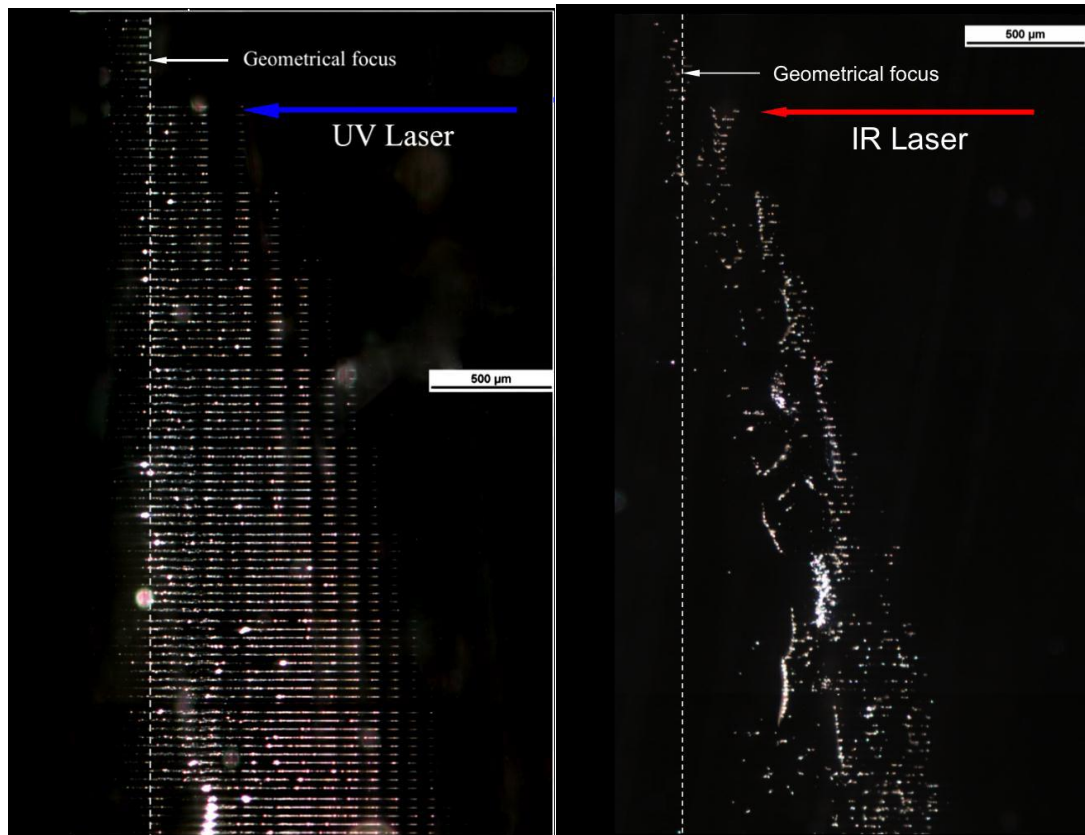


Fig. 2.2-3 CCD images of the accumulated laser scattering and plasma fluorescence signals at different pulse energies. An objective lens with $f = 73.5$ mm, $NA=0.03$ was used to focus the beam inside the glass. The sample was irradiated by roughly (a) 10,000 shots and (b) 10 shots. *from [43]*

Filamentation has also been generated in PMMA ^[15] by a fs laser with 100 fs pulse length, 800nm wavelength and 1kHz repetition rate. Focused by an objective with 0.1 NA, a laser beam with pulse energy from 0.8-1.8 μ J induced filaments from 200-450 μ m long. Fs laser pulses with 180 fs, 775nm (also frequency doubled to wavelength of 387nm) wavelength and 1kHz repetition rate was employed by Dun Liu et al^[44,45] to produce filaments in PMMA (see Fig. 2.2-4). No scanning of the substrate was involved here and so periodic

re-focusing was observed during filamentation. These were much clearer at 387nm than at 775nm.



(a)

(b)

Fig. 2.2-4 Induced structures in PMMA by (a) NUV (387 nm) laser pulses with various pulse energies (0.1 – 1 μJ) and 0.5s exposure time (500 pulses). (b) NIR (775 nm) laser pulses with various pulse energies (1 – 5.5 μJ) and 0.5s exposure time.

The dotted line denotes the geometrical focal position. The re-focusing during filamentation is very clear at 387nm.^{from [45]}

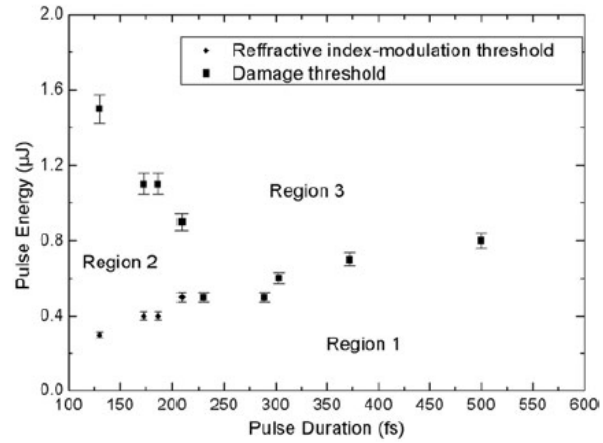
2.3 Effects of processing conditions

2.3.1 Laser parameters

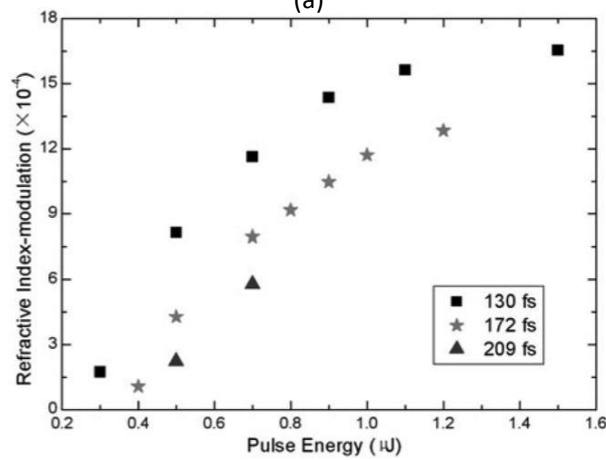
Femtosecond laser induced refractive index modification has been shown to strongly depend on the laser parameters: pulse energy [21,22,43], pulse duration^[46,14], wavelength [19], scanning speed [43], repetition rate^[47, 48], polarization^[49,50], and number of overscans [19]

a) Pulse duration

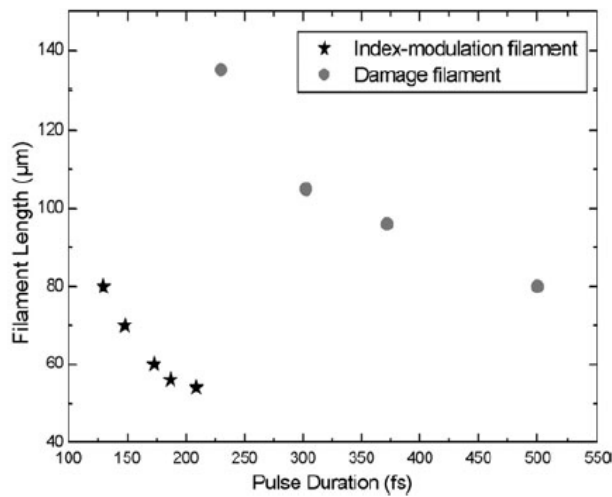
Guo et al^[51] investigate the effects of pulse duration of a femtosecond laser pulse on the refractive index modification in fused silica. A femtosecond laser with pulse durations from 130 fs to 500 fs, a repetition rate of 1 kHz and wavelength of 800nm was focused into fused silica by a 0.8 NA objective. In Fig.2.3-1 (a), region 2, the triangular region, with pulse duration from 130 fs to 230 fs and pulse energy of 0.35 μ J proved to be the processing window for refractive index modification under this focus condition. Outside this region, either material breakdown in region 3 or nothing modified in region 1 were observed. Moreover, the pulse duration also determined the refractive index change and the filament length as well, shown in Fig.2.3-1 b and Fig. 2.3-1c.



(a)



(b)



(c)

Fig 2.3-1: (a) Effects of the pulse duration on the refractive index change threshold and the breakdown threshold with scan speed of $10 \mu\text{m/s}$. (b) Effects of the pulse energy on the refractive index change at the different pulse duration. (c) Effects of the pulse duration on the filament length at the pulse energy of $5 \mu\text{J}$ (star) and $12 \mu\text{J}$ (round). from [51]

For the case of PMMA, Baum^[21] employed a Ti:sapphire femtosecond laser with 800 nm wavelength, 1 kHz repetition rate and duration down to 40 fs to explore the effect of femtosecond laser pulse length in refractive index modification. By minimising the pulse duration together with a high number of over scans using fluences just below the damage threshold provided optimal refractive index modification. Gratings with a period Λ of 40 μm were directly written using a 0.15 NA focal lens. Higher grating diffraction efficiency (inferring higher refractive index change) was obtained with shorter pulse duration. In addition, more scans could deposit more energy into the local area, hence producing higher refractive index change (see Fig 2.3-2) ^[14]. Clearly, NIR fs pulses below 100fs pulselength provide a major improvement in inscription RI modification. Below 100fs, the degree of MPA (proportional to I^3) relative to impact ionisation should increase, allowing higher RI modification before the laser fluence (unit J/m^2) reaching material damage threshold.

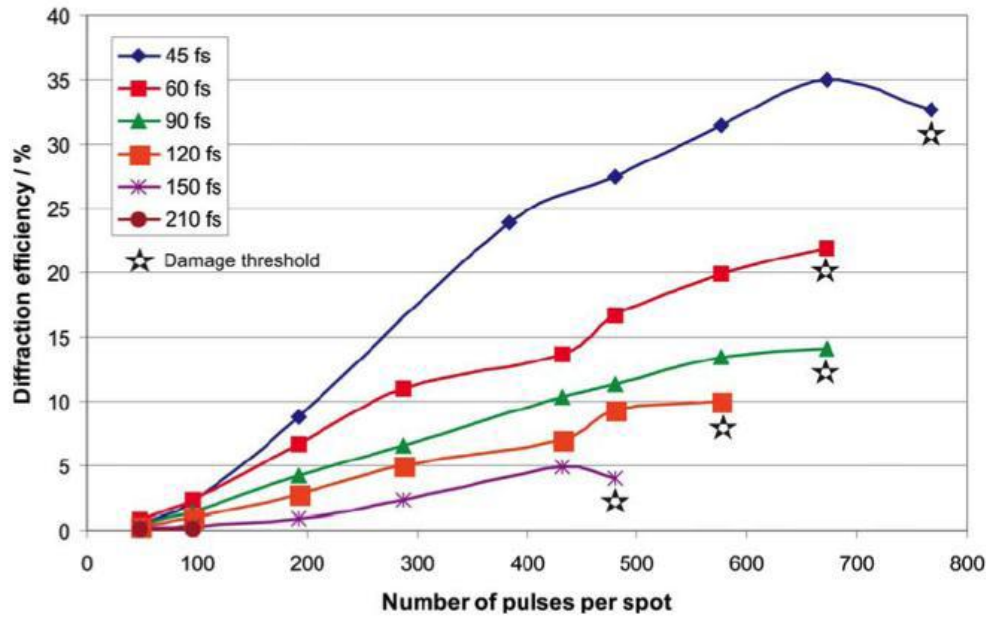


Fig. 2.3-2: Dependence of grating diffraction efficiency on pulse duration and number of pulses per spot (converted from number of over-scans) for a fluence of 0.14 J/cm^2 , from [14]

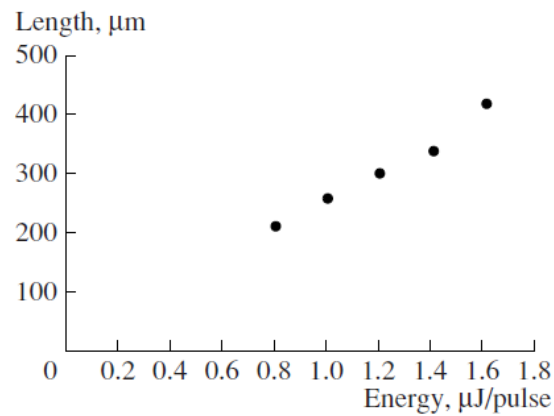
b) Pulse energy

Guo et al^[51] also demonstrated the role of pulse energy in femtosecond laser induced filamentation. As can be seen in Fig. 2.3-1(a), only when the laser pulse energy is between the damage threshold and the modification threshold, can the laser beam induce a filament in the material. Fig. 2.3-1(b) indicates the dependence of refractive index change on pulse energy. The filaments were generated closer to the laser source with higher laser pulse energy.

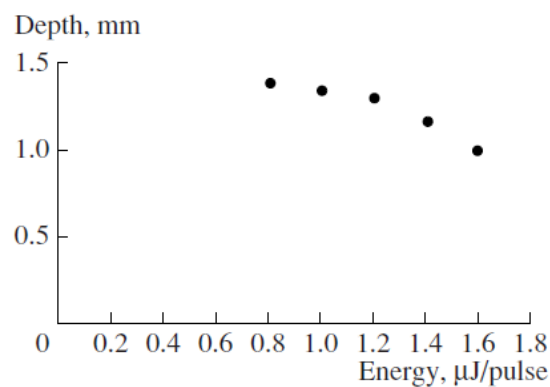
In PMMA, W. Watanabe^[15] used 100fs pulse at a central wavelength of 800nm and 1kHz repetition rate to generate filaments. Laser beams with various pulse energies ranging from 0.8-1.6 μJ were focused by an objective with 0.1 NA into

bulk PMMA. Fig. 2.3-3(a) demonstrates the increasing filament lengths with increasing pulse energy while filament starting depth decreases with increasing pulse energy as shown in Fig. 2.3-3(b).

Therefore, the optimised pulse energy, which must be carefully controlled to be below the material damage threshold, is essential for generating a maximum refractive index change with a certain filament length.



(a)



(b)

Fig. 2.3-3 (a) Length of filamentary refractive index change and (b) position of filamentary refractive index change in PMMA for different pulse energies with

100fs NIR pulses from [15]

c) Wavelength

The wavelength of the laser is a critical parameter for laser internal processing which must be within the transmission window of the material, an essential condition to induce multi-photon absorption. On the other hand, significant linear absorption would prevent the radiation reaching the focus, leading to damage of the material surface.

The laser wavelength determines the quantity of photons required for multi-photon absorption in a certain material. In pure PMMA, which has a bandgap energy of 4.58 eV^[35], three simultaneously absorbed photons at 775nm can provide sufficient energy to excite electron transitions, whereas two photons cannot (see Fig 2.2-2). However, at 387 nm, a single photon has 3.2 eV, and the energy of two photons is thus above the band-gap. The modification of PMMA by Scully et al. ^[52] using NIR (800 nm), sub-100 fs, 1 kHz laser pulses showed that 40 fs pulses created phase gratings with a refractive index change of $\Delta n = 5 \times 10^{-5}$, while 85 fs pulses produced waveguides with $\Delta n = 4.6 \times 10^{-4}$. When 180 fs NIR (775 nm) pulses were used, only very small refractive index changes could be produced with similar writing parameters. In contrast, an 180 fs frequency-doubled NUV beam (387nm) generated gratings with relatively high diffraction efficiency $\sim 40\%$, corresponding to $\Delta n = 4.6 \times 10^{-3}$, which is significantly higher than that obtained with NIR pulses.

d) Effect of pulse repetition rate (PRR)

The thermal accumulation in laser material internal processing depends on the repetition rate of the laser pulses [47]. When the pulse interval is longer than the thermal diffusion time, the thermal expansion of the material can enhance the refractive index modification. At low repetition rate, longer pulse length laser >200fs causes scattering damage^[53] in fused silica while refractive index change can be induced with pulses below 400fs at higher repetition rate^[54]. T. Tamaki et al^[48] drew a processing window for filamentation in fused silica as a function of repetition rate and input energy as shown in Fig. 2.3-4. The pulse energy required for modification drops with the increasing repetition rate. Outside the process window, scattering damage was produced above the threshold energy. No structural modification was induced below the threshold energy. At these high repetition rates higher inscription rates can be achieved leading to a higher processing efficiency.

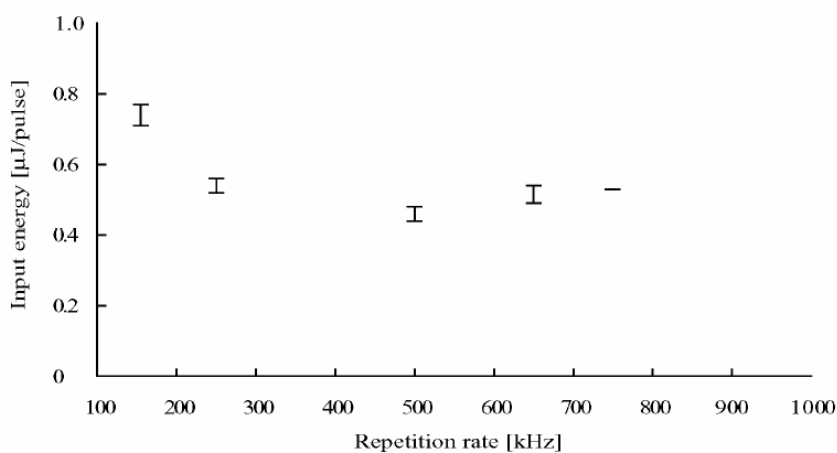


Fig. 2.3-4 Thresholds of induced refractive-index change in fused silica at different repetition rates and NA = 0.55 from [48]

2.3.2 Focusing conditions

(a) Effect of numerical aperture (NA)

The most important focusing condition for femtosecond laser internal structuring is the numerical aperture, NA of the lenses, which determines the width and the length of filaments. A wide range of NAs have been adopted for RI inscription depending on the application, while experimentally a $NA > 0.002$ is generally used to optimize the modifications^[55]. At low NA, from 0.01 to 0.5 the length of the modification is not limited by the Rayleigh length. Self-guiding will occur before the focus as shown in Fig.2.3-5(b) as the result of the dynamic balance between SF (Kerr lensing) and plasma defocusing.

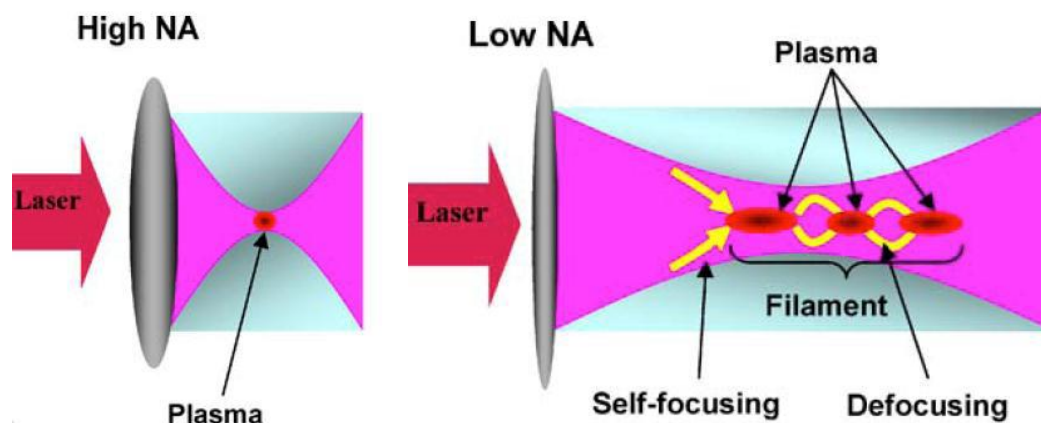


Fig. 2.3-5 Schematic of the damage processes induced by (a) high NA focussing and (b) low NA internal self-focussing

Yamada et al^[56] produced a series of VBGs composed of periodic self-guided long filaments by femtosecond laser (800nm, 1kHz, 130fs) in fused silica samples. As shown in Table 2.3-1, three objective lenses of 0.05, 0.10 and 0.3 NA were

used to fabricate several $300\mu\text{m} \times 300\mu\text{m}$ gratings by varying the thickness and period. The thickness of the gratings determined by the length of the filaments is reduced as the NA increased. Generally, at a low NA < 0.6 , the induced filaments were asymmetric and elongated along the optical axis. At high NA > 0.6 , the modified region will be localized near the focal point, forming a nearly spherically symmetric modification [55]

Table 2.3-1 Diffraction efficiencies of VBGs fabricated under various conditions from [56]

NA of Lens	Thickness of grating	Polarization state of reading beam	Period of grating		
			5 μm	4 μm	3 μm
0.05	200 μm	TE	31.6%	37.0%	39.6%
		TM	18.3%	21.9%	23.7%
0.10	150 μm	TE	63.6%	72.1%	74.8%
		TM	48.4%	58.8%	59.2%
0.30	32.5 μm	TE	4.1%	6.6%	8.9%
		TM	3.0%	4.7%	5.9%

(b) Effect of focusing depth

The position of the focal depth for a given NA is also important to consider. As shown in Fig.2.3-6, the difference of the refractive index on either side of the interface between air and material will induce spherical aberration which stretches the focus along the optical axis, resulting in higher modification thresholds with increasing depth.

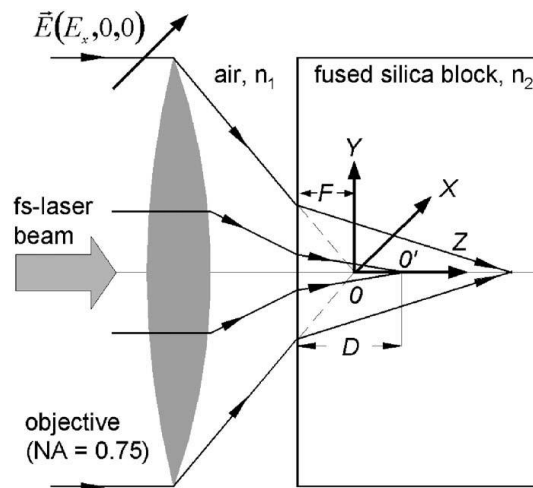


Fig. 2.3-6: Focussing through an air/dielectric interface with a high NA objective.

(Marginal rays focus at a different depth than paraxial rays, which elongates the focal spot, thus inducing a spherical aberration) from [56]

Hnatovsky et al.^[57] demonstrated the depth dependence of the pulse energy required to initiate modification of the irradiated zones near the threshold. Referring to Fig2.3-7, with a dry objective of low NA = 0.2, it is possible to write at a depth of nearly 10mm without a significant intensity drop due to spherical aberration. On the other hand, with a high NA= 0.9 objective, the processing was limited below the surface unless the laser pulse power was increased.

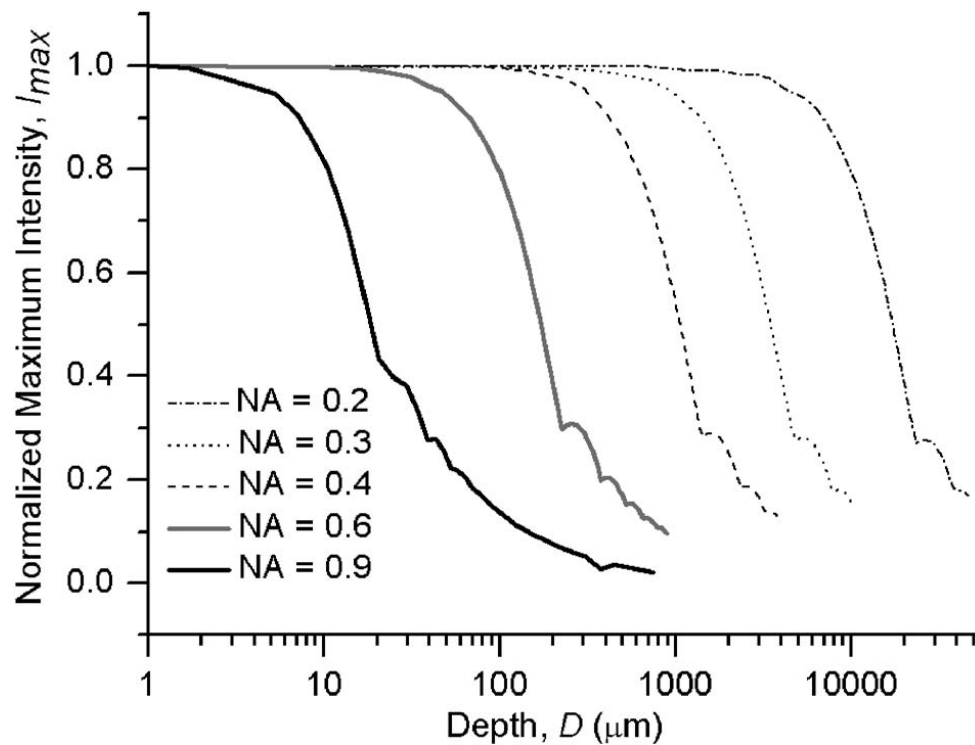
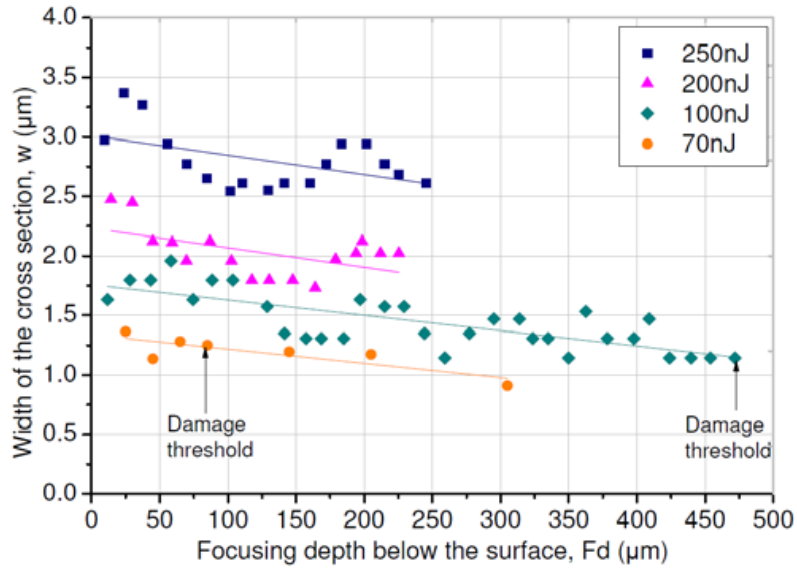


Fig. 2.3-7 Calculated maximum axial intensity I_{max} as a function of focusing depth for different NA's from [57]

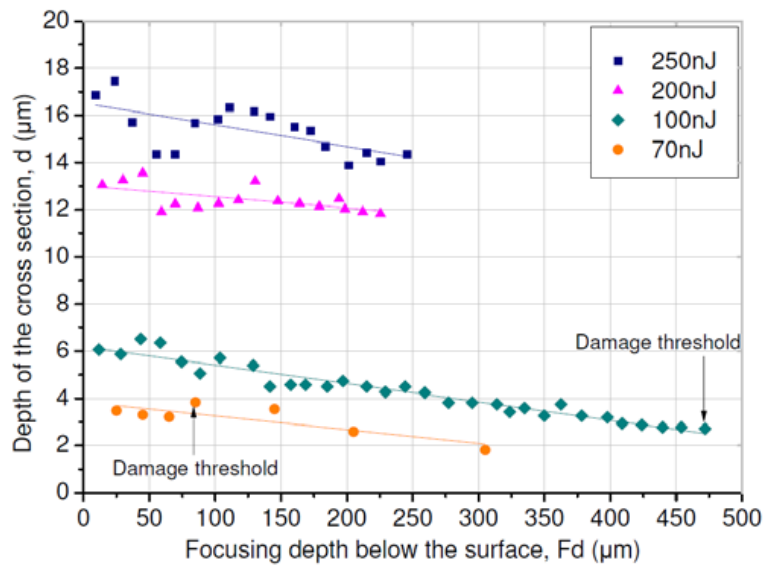
Similarly, D Liu et al [58] also reported that when writing waveguides in fused silica by femtosecond laser, the thresholds for refractive index modification or breakdown increased with the focusing depth. Therefore, the effects of focusing depth should be taken into consideration when producing multi-layer thick devices and clearly, low NA < 0.2 should be advantageous for VBGs to increase the depth.

For PMMA, Liang et al [59] also demonstrated the effects of focusing depth in generating refractive index modification in PMMA by femtosecond laser (100fs, 400nm, 1kHz, NA=0.45). At the focus depth from 0-500 μm below the PMMA surface, a series of refractive index modification structures with different pulse

energies and a constant scanning speed at 1mm/s were inscribed. As shown in Fig. 2.3-8, the width and length of the modified volume decreases with the focal depth, which indicates that for thick 3D structures, laser pulse energy should be slightly increased when processing deep structures.



(a)



(b)

Fig. 2.3-8(a) Width and (b) Depth of the cross-sectional structures as a function of the focusing depth below the PMMA surface from [59]

2.3.3 Material Properties

The refractive index change in a given material is due to both chemical and physical changes so is highly material dependent. The band-gap of materials determines the number of photons required for MPI. As introduced in Chapter 2.2.3, with 800nm fs laser, PMMA needs 3-photons while fused silica requires 6 photons for MPI. With objective NA=0.1, D.Liu et al reported the generation of filaments with the length up to 110 μ m [44] and 220 μ m by using fs laser with 775nm and 387nm respectively[45]. Filaments were created with RI change up to 3×10^{-3} by 378nm femtosecond laser with 0.5NA[60]. In addition, the different refractive index changes produced in various glasses with different properties were studied by Ehrt et al. [50] as shown in Table 2.3-2.

Table 2.3-2 Femtosecond laser refractive index modification in various glass with different compositions and properties from [50]

	Composition (mol%)						
	SiO ₂ (100SiO ₂)	UBK7 (74SiO ₂ 10B ₂ O ₃ 15Na ₂ O/K ₂ O 1BaO)	UV-DURAN (82SiO ₂ 12B ₂ O ₃ 5Na ₂ O/K ₂ O 1Al ₂ O ₃)	BAP (74B ₂ O ₃ 9Al ₂ O ₃ 17PbO)	BB (50B ₂ O ₃ 50Bi ₂ O ₃)	FP10 (10Sr(PO ₃) ₂ 35AlF ₃ 30CaF ₂ 15SrF ₂ 10MgF ₂)	FP20 (20Sr(PO ₃) ₂ 30AlF ₃ 22CaF ₂ 18SrF ₂ 10MgF ₂)
T_m (°C)	CVD	1500	1620	1300	1250	1000	1050
T_g (°C)	1120	560	530	480	420	440	480
α ($10^{-7}K^{-1}$)	6	75	33	60	110	160	155
n_e	1.4602	1.5146	1.4733	1.6160	2.065	1.4602	1.5042
ν_c	68	64	66	44	19	90	80
ρ (g/cm ³)	2.20	2.53	2.22	3.14	6.63	3.45	3.52
UV-edge (nm)	150	195	175	300	400	160	165
band gap (eV)	8.2	6.3	7.0	4.1	2.0	7.8	7.5
Δn^* (nm)	+50	-100	+60	100	45	-120	-190
$\sim \Delta n$ (10^{-4})	+10	-5	+6			-10	-50

Δn^* fs-laser induced difference of optical path length.

Δn fs-laser induced refractive index change measured with different methods.

Yang et al. [61] observed a material dependent effect, which was non-reciprocal ultrafast laser writing (150 fs, 800 nm, 250 kHz) in a z-cut LiNbO₃ crystal, induced by a tightly focussed ultrafast laser beam. They concluded that the effect was due to light pressure, photon drag effect and the associated light-induced thermal current in crystalline media. A significant directional effect of the RI inscription in PMMA at 775nm has also been reported and attributed to pulse front tilt.[62] The scan direction during inscription is therefore important.

2.4 Femtosecond laser producing Volume Bragg Gratings(VBGs)

Femtosecond laser induced refractive index modification in transparent material have been applied widely to integrated optics such as the formation of waveguides[63] couplers[64], gratings [11,212] and 3D storage[30] while the femtosecond laser induced structure breakdown has also been used in three-dimensional storage[65] and microfluidic devices [66]. Among these applications, the creation of VBGs are investigated in this thesis.

2.4.1 Introduction to VBGs

VBGs are used in a wide range of interesting applications, such as astronomical spectroscopy, ultrafast laser compressors and wavelength division multiplexing[67], wavelength stabilization of high power laser diodes[68] and narrowband filters for Raman spectroscopy[69]. Further, chirped VBGs have been used in the stretching and compression of ultrafast laser pulses in fibre laser

Chirped Pulse Amplification (CPA) systems, eliminating dispersion mis-match of the stretcher/compressor [70]. VBGs are generally produced holographically in photo-sensitive materials such as DiChromated Gelatine films (DCG) typically 10-30 μm thick with refractive index (RI) modulation $\Delta n \sim 0.02 - 0.1$ [71] or Photo-Thermorefractive (PTR) glass where modified thickness can be several mm's with $\Delta n \sim 0.001$ [72]. Such gratings are remarkably stable and in the case of PTR material, can handle high average laser powers exceeding 100Watts with damage thresholds $F \sim 10 \text{Jcm}^{-2}$ [73]. Careful design can result in devices with high diffraction efficiency close to unity combined with line densities $>1000 \text{lines/mm}$.

Kogelnik theory (Coupled Wave Theory) [74] is the most commonly used model for theoretical analysis of thick gratings. A grating thickness parameter, Q, is generally used as a criterion to determine whether the grating is thick or thin [75].

Q is given by

$$Q = \frac{2\pi\lambda L}{n\Lambda^2} \quad \text{Eq. 2-3}$$

where, λ is the readout wavelength, L is the grating thickness, n is the refractive index of the bulk material, and Λ is the grating period, as depicted in Fig. 2.4-1.

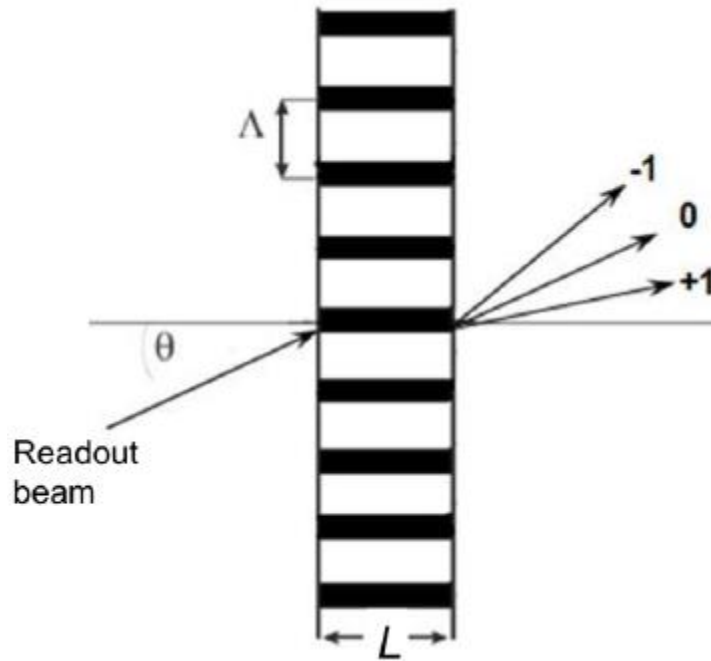


Fig. 2.4-1 Schematic of a readout beam passing through a VBG inscribed at normal incidence

For a thick grating with thickness parameter $Q > 10$ under the Bragg condition, according to Kogelnik theory, the first order diffraction efficiency η depends on the refractive index change, Δn , and the thickness of grating:

$$\eta = \sin^2\left(\frac{\pi\Delta nL}{\lambda\cos\theta_b}\right) \quad \text{Eq. 2-4}$$

where λ is the incident laser wavelength and θ_b is the Bragg angle.

2.4.2 Traditional methods of femtosecond laser inscription of VBGs

Commonly, a thick VBG is built layer by layer from the bottom to the surface^[45]. Single beam VBG direct writing by fs laser usually requires a long processing time to build a thick grating due to the limited scanning speed and long processing distance ^[76]. To improve the processing efficiency, several methods

have been reported.

One approach to rapid fabrication of VBG is to increase the repetition rate which allows a higher scanning speed. Domas Paipulas et al^[11] demonstrate a comparatively fast grating writing technique by using high repetition rate Yb:KGW femtosecond laser (1030nm, 300kHz, 300fs). They produced a grating with 1mm by 1 mm area, 2 μ m period and up to 60 μ m depth in less than an hour, reaching 57% diffraction efficiency. In 2003, Yamada K et al.^[56] proposed to reduce the processing time by taking advantage of the self-trapped long filament of the femtosecond laser pulses. They produced 10-500 μ m long filaments in fused silica to build multi-layer gratings. However, it still took 5-9 hours to fabricate a grating with the period of 3 μ m and volume of 300 μ m \times 300 μ m \times 150 μ m (thick). In 2009, cylindrical lenses were adopted by Fei He et al^[77] to produce large volume grating in foturan glass with an area of 2mm \times 3mm, a thickness of 2mm and a period of 15 μ m. A laser beam was focused to a long elliptical shape (2 μ m \times 1800 μ m) by using a pair of cylindrical lenses as shown in Fig. 2.4-2. Unfortunately, accompanied with the increased processing efficiency, the modified region inside the material was non-uniform due to the uneven filamentation. (Fig.2.2.2)

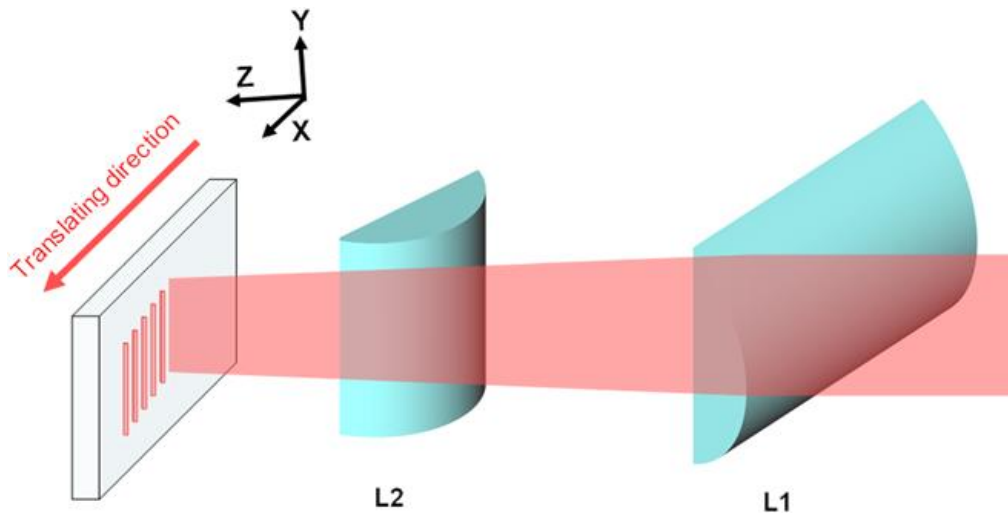


Fig. 2.4-2 Schematic diagram of femtosecond laser focused by a pair of cylindrical lenses^{from [77]}

The application of femtosecond laser to writing grating by two-beam interference was first demonstrated by Kawamura ^[78] et al. Two beams split from a Ti:sapphire laser (10 Hz, 180 fs, 800 nm) were focused at an angle 10-30 degrees by two lenses to generate interference at the focus. One of the two beams passed through a delay line to achieve the temporal overlapping with the other beam. The resulting interference fringes were used to produce permanent grating structures inside diamond with a period of 2.5 μ m. After that, the same technique was also presented by other groups ^[18]. However, the accurate temporal overlapping of the two beams is technically difficult to achieve because a very precise adjustment is required. In addition, the spatial overlapping of the two beams is not easy to achieve as well due to the very small focus size. Furthermore, considering the processing efficiency, the interference fringes were all limited within the focus so that long scan time is required, along with varying uniformity and so unsatisfactory for processing ^[60].

A recent improvement of two beam interference technique is reported by Christian Voigtländer et al^[79] in 2010. A VBG with a period of 1.075 μm was inscribed in fused silica with a femtosecond laser which is focused by a cylindrical lens and passing through a phase mask, as shown in Fig.2.4-3 The first order diffractive efficiency reached 80% with a 1mm thick grating. This technique has a very simple optical setup and the processing results were quite uniform. The grating period was fixed by the mask period and could only be changed by fabricating a new mask, which was rather expensive.

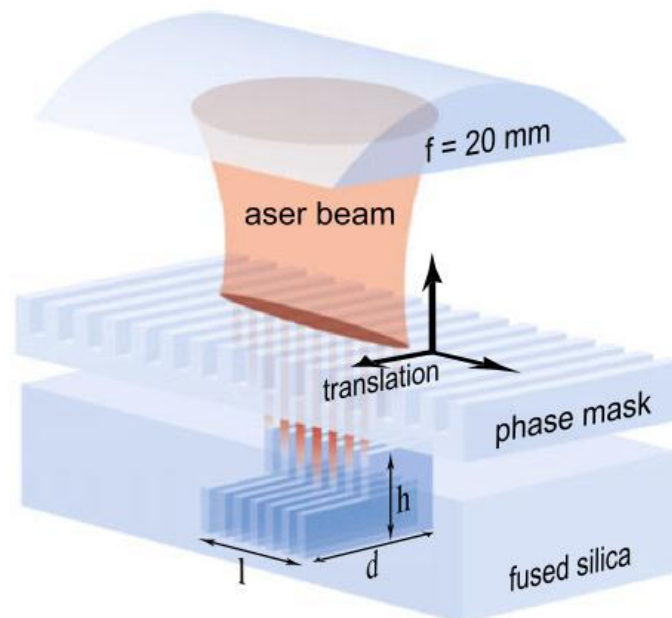


Fig. 2.4-3 Schematic setup for inscription of VBGs using a cylindrical lens and a phase mask^{from[79]}

2.4.3 Femtosecond laser writing Bragg grating in PMMA

Thanks to their ease of manufacture and low cost, polymers are attractive substrates for the fabrication of photonic components such as transient optical memory, [13] 2D and 3D waveguides, [14, 15], 3D micro-channels, [16] splitters, [28] and VBGs [18]. In the latter case [18], holographic exposure of azodye doped PMMA with NIR, 150fs pulses yielded 0.3mm diameter VBGs with a first order Bragg diffraction efficiency (DE), ~90% and 200lines/mm. However, the inscription simultaneously created surface relief gratings, which are material surface structures, contributing an estimated ~90% to this high efficiency.

Pure PMMA is of interest because it has high optical transparency, is inexpensive and so ideal for creating disposable photonic devices for clinical, biological and chemical applications. For example, NIR, low NA femtosecond laser inscription of 200 μ m thick VBGs in undoped PMMA was first demonstrated using 40fs, 1kHz pulses at 800nm with $\eta_1 \sim 37\%$ and inferred $\Delta n \sim 5 \times 10^{-4}$ [19]. Mochizuki et al [20] produced 10 μ m pitch, 300 μ m thick VBGs in PMMA and other polymers, using 0.5 μ J, 120fs pulses at 800nm and 1kHz repetition rate, focussed with a low NA = 0.13 objective, with highest $\eta_1 \sim 45\%$ in poly(methyl)pentene. More efficient inscription in PMMA at 800nm occurs with temporal pulselengths $\tau_p \leq 100fs$ allowing overscanning of exposed regions thus increasing Δn without optical breakdown [21]. At low NA ~ 0.1 , filamentation occurs in dielectrics, leading to a dynamic balance between Kerr lens focussing and plasma defocusing, extending modification depths well beyond the Rayleigh length, ideal for creating thick

VBGs [22]. By frequency doubling longer, 160fs NIR pulses at 775nm to the NUV, excellent inscription in PMMA was achieved at 387nm and the photochemistry mechanisms investigated after exposure [80].

Single beam inscription, especially at low kHz repetition rates can be accelerated by the use of parallel processing using a Spatial Light Modulator, (SLM), capable of generating arbitrary spot patterns when addressed with appropriate Computer Generated Holograms (CGH's)[80].

2.5 Laser parallel processing technique

The processing techniques can be roughly divided into 3 categories: single beam processing, two beam interference processing which has been introduced above and multi-beams processing by using SLM.

2.5.1 Introduction to spatial light modulator (SLM)

A SLM provides an approach to diffract a single laser beam into a 3D pattern with controlled characteristics, enabling a wide range of applications in photonics. The device mainly consists of an array of pixels, each of which can individually control the phase or amplitude of incoming light. They can be used not only to split an energetic laser beam into many arbitrary diffracted spots in 2D and 3D but also to correct wavefront aberrations. It's a remarkable optical device which demonstrates sophisticated control of incoming wavefronts.

Since their introduction in the 1980s [82], SLMs have been applied in many research areas, such as temporal pulse shaping [82], holographic optical tweezers [83-86], spatial beam shaping [87-90], wavefront correction [91, 92] and laser parallel processing [93-96].

SLM are mainly divided into two kinds. The first kind is called micromechanical SLMs which use an array of tiltable mirrors to physically change the paths of each pixel on the cross-section of the incoming light. This kind of SLM is only available in reflective mode. The second one is electro-optical SLMs that are based on various types of liquid crystal (LC) displays, and can work in either transmissive or reflective mode. In the following research, only reflective LC SLMs are employed, because they are more cost effective and flexible than the micromechanical SLMs, and offer high light utilisation efficiency.

Nematic LC is the most commonly used material for the LC SLMs. Fig. 2.5-3 shows a typical structure of a LC SLM. LC molecules in the LC layer are controlled by the voltage applied to the ITO and the electrodes layers. When the SLM is addressed with a Computer Generated Hologram (CGH), various voltages, which depend on the greylevel of the CGH, are applied on each liquid crystal pixel. Under the E field, the LC molecules make a voltage-dependent rotation, resulting in a refractive index change. Consequently, the phase of the incoming light is modulated after reflection (see Fig.2.5-1).

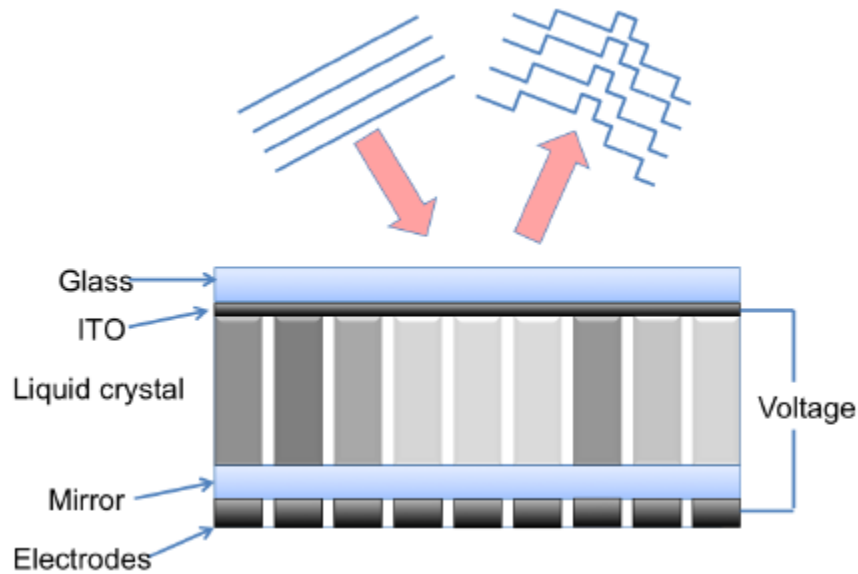


Fig. 2.5-1 Typical structure of a LCOSLM.

The LCOSLMs can be further divided into two categories, twisted nematic liquid crystal devices and parallel aligned nematic liquid crystal devices. In a reflective twisted nematic LCOSLM, the LC cells are filled with LC molecules that form a twisted structure, and they have two director plates aligned at a relative angle of 45° between the top and bottom of the LC layers. Polarised light passing through these cells follows the helical molecule axes, leading to a phase and polarisation change. However, in a parallel aligned nematic LCOSLM, the LC cells comprise two parallel director plates. Therefore, it can modulate the phase of the incoming light without affecting the polarisation.

2.5.2 Algorithms for calculating computer generated hologram (CGHs)

The CGHs for producing multi-beam patterns can be calculated by several algorithms, including Gerchberg-Saxton (GS) [97], Gratings and Lenses (GL) [52],

Weighted GS (GSW) [98], Generalised Adaptive Additive (GAA) [99], optimal rotation angle (ORA) [100], Multiplexed Phase Fresnel Lenses (MPFL) [101] and Mixed-Region Amplitude Freedom (MRAF) [70]. The GS algorithm, first introduced by Gerchberg and Saxton in 1972 [97], is used in this research as it is an iterative Fourier transform algorithm with a good accuracy and reasonable calculation speed. The grating and lens is a non-iterative algorithm with perhaps the fastest calculating speed but comparatively lower accuracy [93].

The GS algorithm is an iterative algorithm for retrieving the phase of two light distributions related via the fourier transform. The diagram in fig.2.5-2 illustrates the flow chart of the generation of a phase hologram with the GS algorithm.

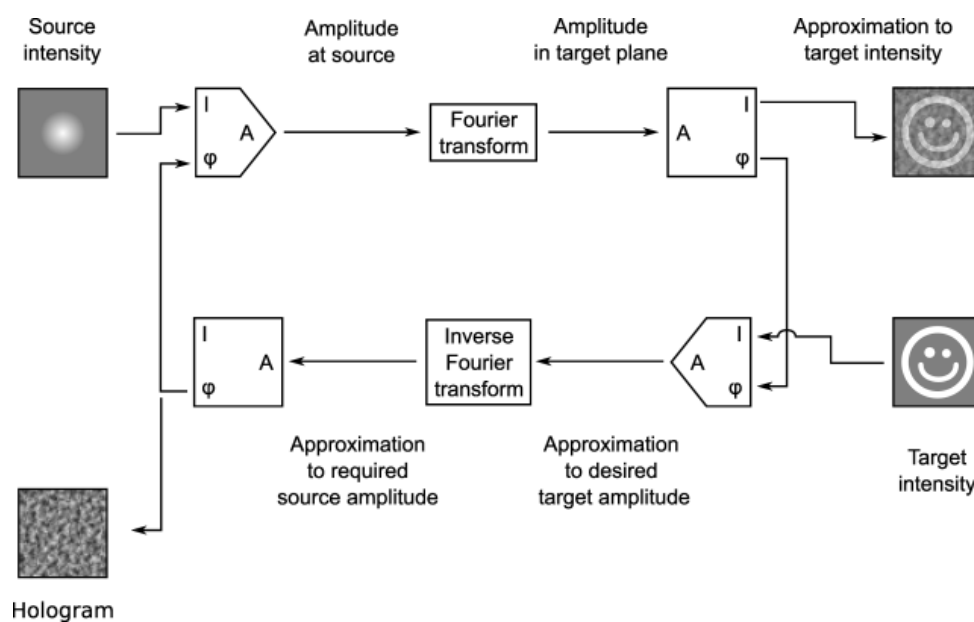


Fig. 2.5-2 Diagram graphically shows how to generate a phase hologram with the GS Algorithm

When the target intensity, which is the laser intensity distribution in the focal

plane of the objective, is designed in the image space as $I_t = I(x_t, y_t)$, the desired phase $\varphi_h = \varphi(x_h, y_h)$ at the hologram plane can be calculated to satisfy $FT[\exp(i\varphi_h)] = I_t$. Starting with an random $\varphi_{h,1}$ and the intensity distribution of the original laser beam supposed to be a Gaussian amplitude, the light field in the hologram plane is:

$$\psi_{h,1} = \exp(i\varphi_{h,1}) \quad \text{Eq. 2-5}$$

At the image plane, the light field can be expressed by using fourier transform as:

$$\psi_{i,1} = FT[\exp(i\varphi_{h,1})] \quad \text{Eq. 2-6}$$

Then, the intensity component is replaced by target amplitude I_t while the phase components keeps the same:

$$\psi'_{i,1} = \sqrt{I_t} \exp(i\varphi_{i,1}) \quad \text{Eq. 2-7}$$

Using inverse Fourier transform, the $\psi'_{i,1}$ is reversed to the hologram plane:

$$\psi'_{h,1} = FT^{-1}[\sqrt{I_t} \exp(i\varphi_{i,1})] \quad \text{Eq. 2-8}$$

Then, for the 2-nd iteration, the phase component at the hologram is replaced by:

$$\varphi_{h,2} = \arg(\psi'_{h,1}) \quad \text{Eq. 2-9}$$

And after repeating the above calculation by k iterations, at the hologram plane the phase component of the light field can be expressed as

$$\varphi_{h,k} = \arg(\psi'_{h,k}) \quad \text{Eq. 2-10}$$

while for the k-the iteration:

$$\psi_{h,k} = \exp(i\varphi_k) \quad \text{Eq. 2-11}$$

The GS algorithm can be used not only to generate multiple focussed spots of light but also arbitrary two-dimensional intensity distributions. Extended by Haist et al. [101], the GS algorithm has been demonstrated to modulate the

intensity distributions in several planes simultaneously. Later, Sinclair et al. [83] have successfully applied this algorithm in holographic optical tweezers, simultaneously trapping several objects in individually controllable arbitrary three-dimensional positions. This algorithm takes advantage of the phase freedom and iteratively optimizes the focal-plane intensity distribution by varying both these phase values and φ_h .

2.5.3 Parallel Femtosecond laser internal structuring with SLM

The first demonstration of applying holographic fs laser processing using SLM carried out by Hayasaki^[103] et al in 2005 (see Fig. 2.5-3). A fs laser (150fs, 800nm, 1kHz) was diffracted by the liquid crystal spatial light modulator into an arbitrary set of beams, the zero order and ghost of which was blocked by a shutter placed in a 4f optical system. Then, the first order diffracted beams were focused to the sample for processing.

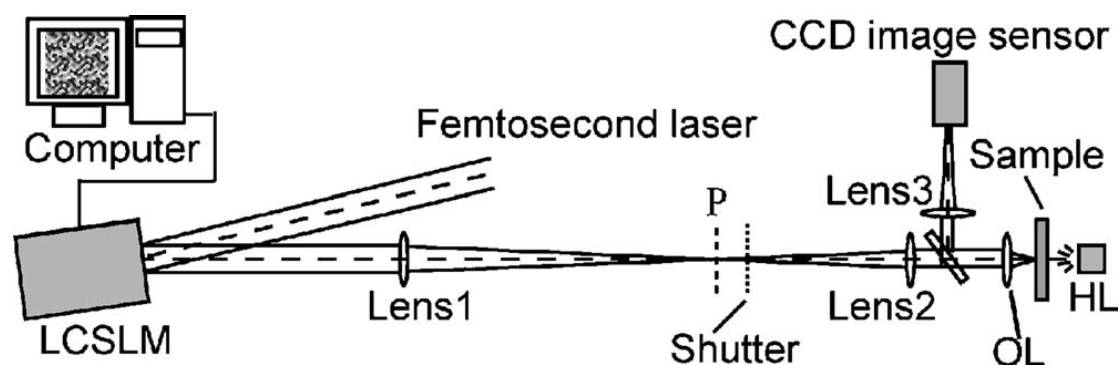


Fig. 2.5-3 experimental setup for femtosecond laser parallel processing by using

SLM from [103]

Hayasaki's group further developed a number of applications, including the first

application of this technique to material internal processing in 2006^[104]. They applied a multiplexed phase Fresnel lens (MPFL) (see Fig.2.5-4), to generate parallel fs laser beams for 3D internal structuring in glass. In addition, they also optimize the uniformity of the diffracted beams by changing the center phase and size of each phase Fresnel lens while taking account of the intensity distribution of the irradiated laser pulse and the spatial frequency response of the SLM.

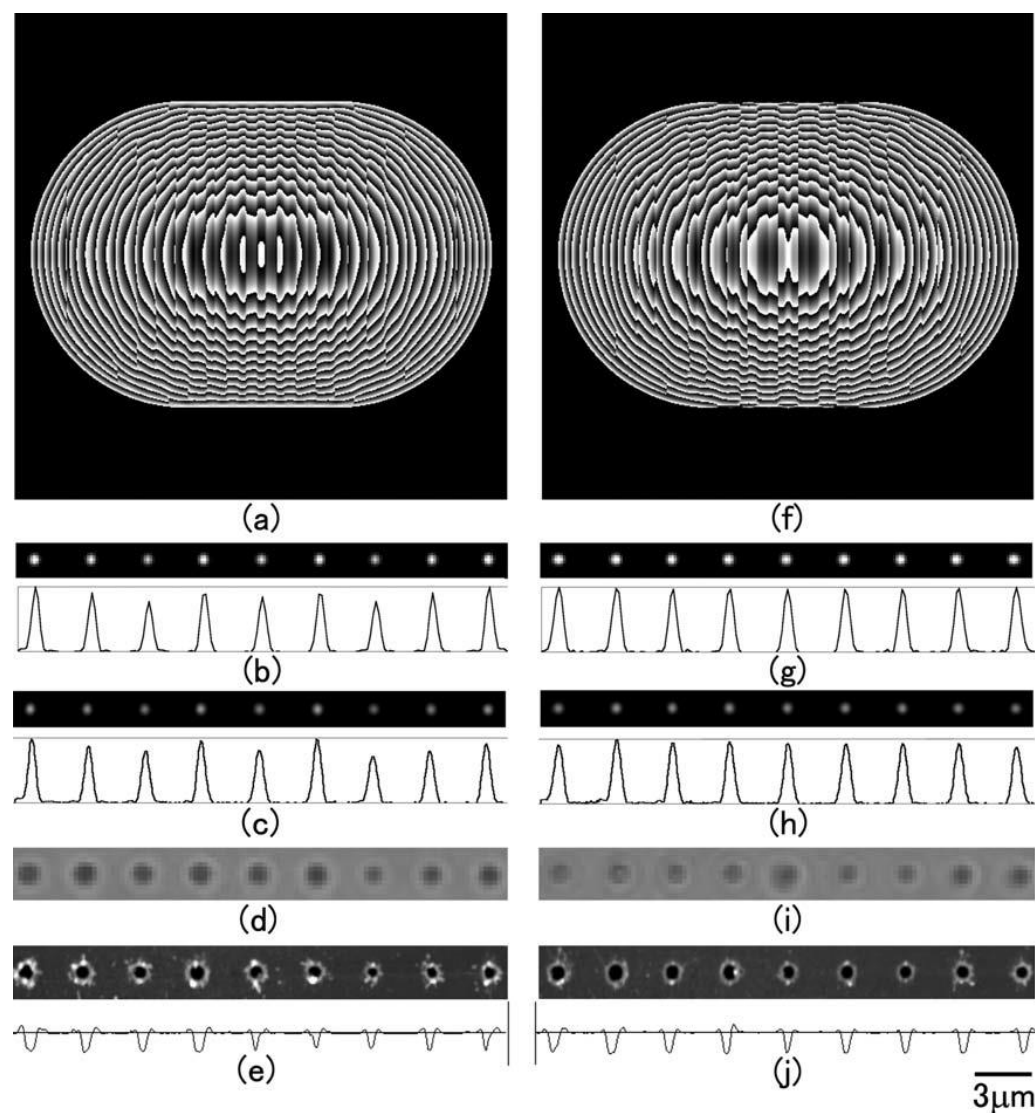


Fig. 2.5-4 (a) Original and (f) optimized MPFL. (b), (g) Respective computer reconstructions. (c), (h) Respective optical reconstructions. (d), (i) Transmission microscope and (e), (j) AFM images of the fabricated area. from [104]

D.Liu et al ^[62] applied this technique in producing VBGs by using a 775nm, 160fs laser. VBGs up to 4mm thick were created by 16 focused parallel beams with the aid of a phase only SLM. The measured first order diffractive efficiency fit well with Kogelnik's theory (see Fig. 2.5-5), reaching 75% at 4mm thickness. However, these gratings also demonstrated unsatisfactory stability with first order diffraction efficiency decreasing after a period of months. Later NUV(387nm) fs laser was employed by D. Liu et al ^[45] to produce VBGs in PMMA with 16 parallel beams. A 2mm thick VBG was generated with first order diffractive efficiency up to 70% and refractive index modification of 8.5×10^{-5} . The deviations of the experimental data from the theoretical curve, mainly due to the fabrication errors. The VBGs stabilised after a developing period of about 30days.

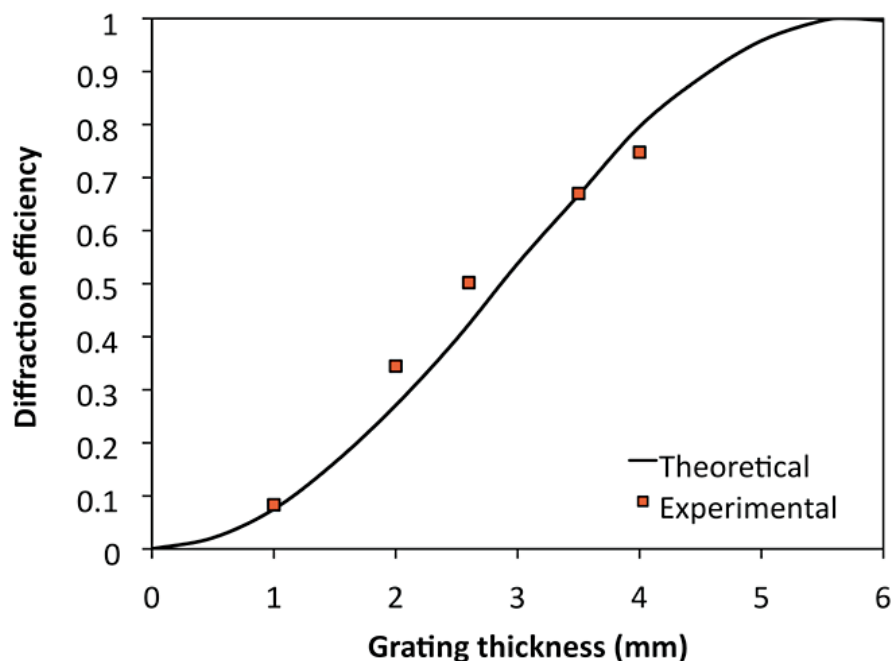


Fig.2.5-5 10 Diffraction efficiency of a series of VBGs of varying thickness^[62]

inscribed at 775nm and comparison with Kogelnik's theory from ^[74]

2.5.4 Optimization of CGHs

By using an SLM, an ultrashort pulse laser can be diffracted into a desired beam array or any other random patterns with reasonable uniformity. However, the uniformity easily degrades due to the limitation of the CGH calculation and effect of the SLM such as the finite pixel size, the crosstalk between pixels and the phase modulation characteristics.

2.5.4.1 Improvement of algorithms

The uniformity of multi-pulse energy which is dependent on the CGH can be optimized by considering the spatial distribution of the laser pulse intensity (Gaussian distribution in most cases) and the spatial frequency properties of the SLM^[100,104,105, 106]. For a complex experimental setup, however, it's almost impossible to modulate all these factors in the system to modify the hologram calculation progress. To obtain multiple beams with high energy uniformity, research in this has been carried out to improve the existing algorithms or developing new algorithms.

Roberto et al^[107] summarized the theoretical calculation results of the different CGH algorithms. Tables 2.5-1 and 2.5-2 shows the theoretical and experimental performance of weighted Gerchberg-Saxton (GSW)^[107] with respect to the currently available algorithms, random mask (RM) ^[108], superposition of prisms and lenses (S)^[109,110], Random Superposition (SR)^[111], Gerchberg-Saxton (GS)^[112,83], Generalized Adaptive Additive algorithm (GAA)^[114], Direct Search

algorithm (DS)^[115,116]. In Table 2.5-1 and 2.5-2, the target trap structure is a 10 × 10 square grid. Column 2 (Table 2.5-1) contains a 100 × 100 detail of the total 768×768 hologram. Performance parameters after K (column 6) iterations are reported in columns 3,4,5. Computational calculation complexity is reported in column 6 where: M=number of traps, N=number of pixels in hologram, K=number of iterations, P=number of gray levels (256 here), $e = \frac{\sum_{m \neq 0}^m I_m}{\sum_m I_m}$ (diffracted pulse energy / total pulse energy) is the diffraction efficiency, $u = 1 - \frac{\max(I_m) - \min(I_m)}{\max(I_m) + \min(I_m)}$ indicates the pulse energy range and $\sigma = \frac{\sum_m \sqrt{(I_m - \bar{I})^2}}{\bar{I}} \times 100\%$ is the standard deviation over mean. As a result, theoretically, the GSW has the best performance with 93% diffraction efficiency and good uniformity. However, the experimental result has $u=0.9$ compared to $u=0.99$ theoretically. This lower experimental performance for uniformity indicates $\pm 10\%$ error for I_m from average energy \bar{I} . This level of uniformity can degrade structures generated by these parallel beams.

Table 2.5-1 Summary of theoretical performances of investigated algorithms.^{from[107]}

algorithm	detail	e	u	$\sigma(\%)$	K	scaling
RM		0.01	0.58	16	-	N
S		0.29	0.01	257	-	$N \times M$
SR		0.69	0.01	89	-	$N \times M$
GS		0.94	0.60	17	30	$K \times M \times N$
GAA		0.93	0.79	9	30	$K \times N \times M$
DS		0.68	1.00	0	$7.5 \cdot 10^5$	$K \times P \times M$
GSW		0.93	0.99	1	30	$K \times N \times M$

Table 2.5-2 Summary of experimental performances
of investigated algorithms ^{from[107]}

algorithm	e	u	$\sigma(\%)$
RM	0.02	0.60	18
S	0.28	0.03	190
SR	0.68	0.05	74
GS	0.92	0.63	17
GAA	0.97	0.74	10
DS	0.73	0.88	4
GSW	0.93	0.90	4

2.5.4.2 Asymmetric beam designs

J. Curtis et al reported that the multi-beam patterns with a high degree of symmetry (Fig. 2.5-5(a)) lead to non-uniform intensity in diffracted beams from overlapping ghosts^[117]. The pulse energy uniformity was improved by D.Liu et al^[62] by breaking symmetry, for example, by introducing slight random

displacements of the required spot pattern (Fig. 2.5-6(b)). The spots were offset randomly in the Y axis (scan direction) while maintaining fixed pitch Λ . The cross-sections of the filament (see Fig. 2.5-6(b)) produced by asymmetric beam geometry are much more uniform, but certainly not perfect.

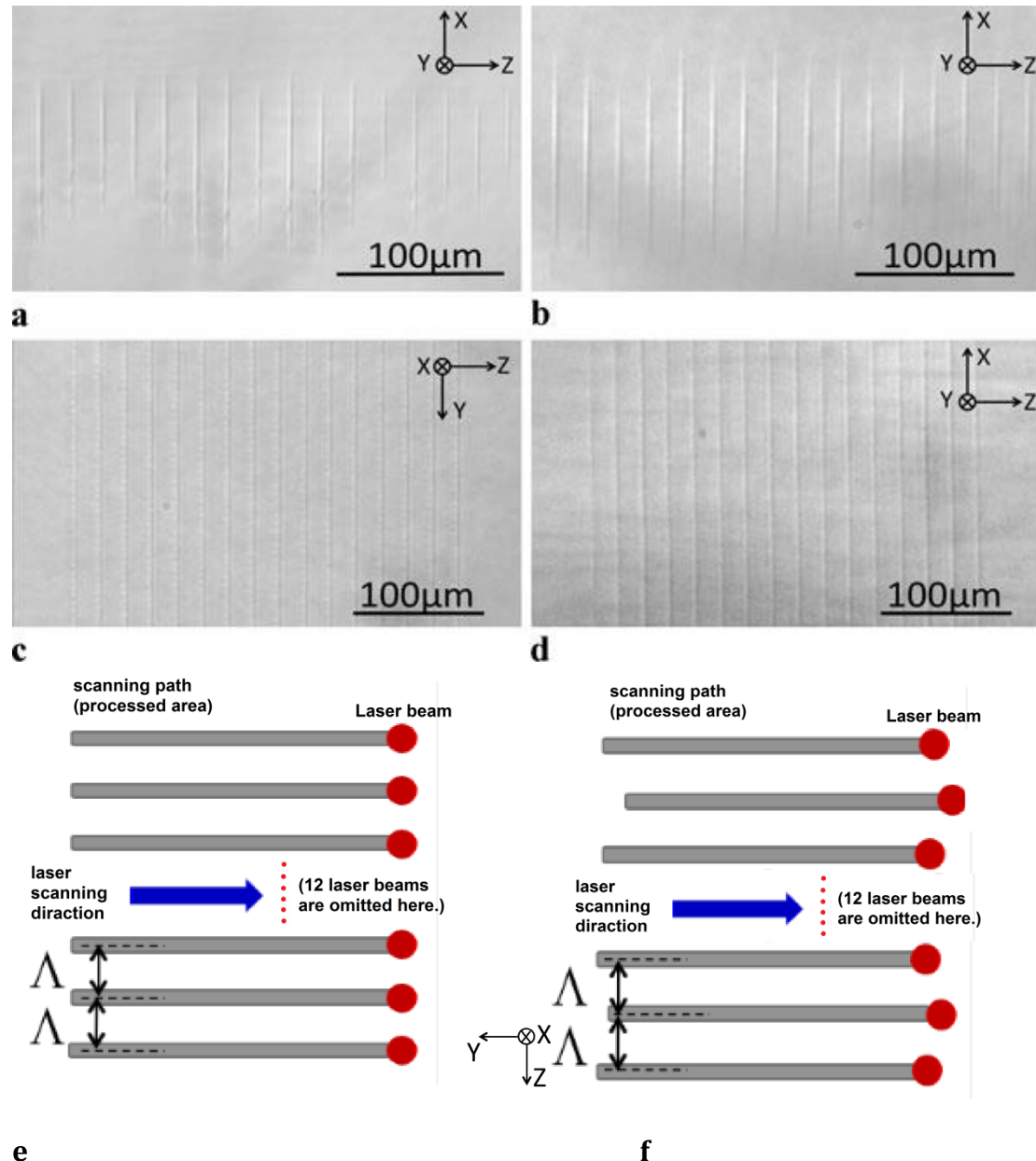


Fig. 2.5-6: Cross sections of the gratings written by 16 beams with (a) symmetric pattern and (b) asymmetric pattern showing improved uniformity. (c) front view and (d) cross section of a volume grating written by asymmetric spot pattern. The

volume grating consists of multi-layer with offsets $x = 100 \mu\text{m}$ to create continuous modification. The laser beams propagate along +X direction, and the sample translation direction is in +Y direction. Schematics of (e) a symmetric multi-beam pattern and (f) an asymmetric multi-beam pattern for parallel processing. The arrows denote the translation direction (+Y) of the sample.^[62]

Calculation speed of this algorithm is as fast as the general GS algorithm. The uniformity is also good enough to be utilised in real-time manipulation of the multiple trapping for optical tweezers, but still not suitable for high precision laser microprocessing. The down sides of this method are:

- 1) A symmetric 1D or 2D parallel beam array cannot be optimized by this method.
- 2) The uniformity after optimization is still not adequate and requires further improvement.

2.5.4.3 Camera based optimisation

The application of camera based optimisation system in the improvement of uniformity of SLM-generated multiple beams was first demonstrated in 1990^[118]. Y. Hasegawa and Hayasaki et al developed this technique for improving femtosecond laser beams uniformity^[119,105,103], using second harmonic generated by beta- BaB_2O_4 to optimize holographic femtosecond with the diffracted pulses collected by the CCD sensor (shown in Fig.2.5.7). The uniformity of the pulse energy was significantly improved, averaging at pulse energy uniformity $u=0.95$

($u = 1 - \frac{\max(I_m) - \min(I_m)}{\max(I_m) + \min(I_m)}$, I_m is the laser intensity of the m -th laser beam) after about 10 iterations as shown in Fig. 2.5.8.

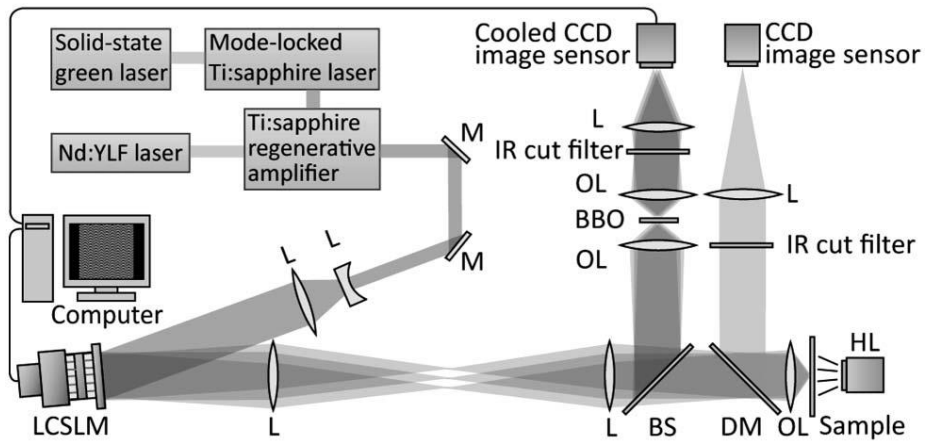


Fig.2.5.7. Holographic femtosecond laser processing system^[119]

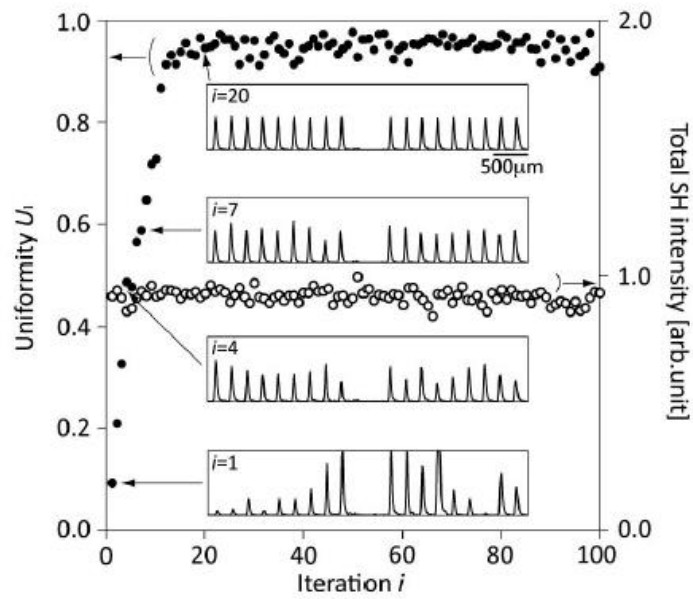


Fig. 2.5.8. Changes of the uniformity (filled circles) and the total SH intensity (open circles), from [119]

2.6 Polarisation dependent filamentation

Laser induced filamentation, which is accompanied with super-continuum, is an example of a highly nonlinear optical effect. Femtosecond pulses with ultrahigh peak powers easily generate such effects when focussed into dielectrics. As SF, related to third order non-linear susceptibility $\chi^{(3)}$ is polarisation dependent, the laser polarisation is also an important parameter during internal processing.

2.6.1 Critical Power for self-focusing (SF) and supercontinuum (SC)

As introduced in Section 2.2.3.2, laser beam forms a compressed focus with high intensity^[120] due to SF. Peak power above critical power threshold is the trigger for the generation of SC and this focus is the start of a filament.

The SC was first observed by Alfano and Shapiro^[121] in 1970. A wide spectrum, extending from the visible to NIR, was induced by focusing a giant picosecond laser beam into glass. The first femtosecond laser induced SC was generated by Fork et al in 1983^[122]. By focusing a 80fs laser beam into an ethylene glycol film, a spectrum covering the NUV to NIR was also observed^[123]. SC generation in gas by femtosecond laser was also reported by Corkum et al^[124]. M. Bradler et al ^[125] demonstrated the SC generated in several common laser host materials. Spanning spectra (400 nm to ~1200 nm) were produced in fused silica and sapphire (see Fig. 2.6-1) by 250 fs laser with mJ-level pulses^[126]. The basic mechanism responsible for the white-light continuum is the free electron enhanced self-phase modulation process^[127].

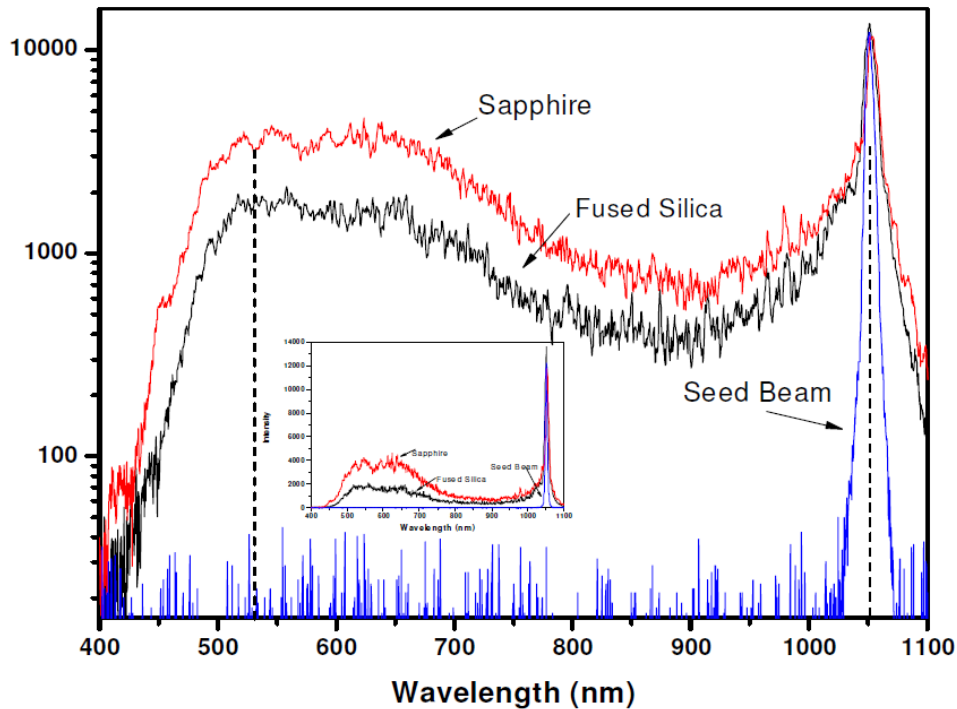


Fig. 2.6-1 Seed beam , white-light continuum spectra of sapphire and fused silica. [126]

A. Brodeur et al^[128] reported the dependence of critical power for SC on band-gap (see Table 2.6-1). SC was generated in different materials with 140fs laser (796nm). Clearly, the threshold for SC increases with the band-gap of the material, implying critical power for SF is inversely proportional to the Kerr index^[129]. They also found a band-gap threshold for the generation of SC due to the sharp reduction of diameter at focus d_{\min} from about $15\mu\text{m}$ to $10\mu\text{m}$ with the E_{gap} exceeding 4.7eV. In media with $E_{\text{gap}} < 4.7\text{eV}$, SF is stopped at lower intensity by plasma generation, also severely limiting the bandwidth of the continuum generated.

Table 2.6-1 Anti-stokes broadening $\Delta\omega_+$ and key data measured at $P=1.1P_{th}$:
 minimum beam diameter at focus d_{min} , maximum fluence F_{max} and energy loss E_{loss} .

P_{th} is accurate within $\pm 20\%$ from [128]

Medium	E_{gap} (eV)	$\Delta\omega_+$ (cm^{-1})	d_{min} (μm)	F_{max} (J/cm^2)	E_{loss} (%)	P_{th} (MW)
LiF	11.8	19 800	10.8	1.3	13	8.8
CaF ₂	10.2	18 300	10.4	1.0	11	7.4
Water	7.5	14 600	9.8	0.62	4	4.4
D ₂ O	7.5	14 600	10.6	0.46	4	3.6
Fused silica	7.5	13 500	10.4	0.57	3	4.3
Propanol	6.2	14 200	9.1	0.57	3	3.3
Methanol	6.2	14 500	10.2	0.54	4	3.9
NaCl	6.2	9000	9.9	0.29	3	2.0
1,4-Dioxane	6.0	10 200	9.3	0.44	3	2.7
Chloroform	5.2	11 200	10.0	0.29	1	2.2
CCl ₄	4.8	10 400	8.7	0.44	2	2.5
C ₂ HCl ₃	4.7	950	14.6	0.08	<1	1.2
Benzene	4.5	600	14.0	0.07	<1	0.90
CS ₂	3.3	400	15.6	0.01	<1	0.23
SF-11 Glass	3.3	340	15.6	0.03	3	0.52

The equivalence of the critical power for SF and SC was first investigated in 1967^[130]. After that, a series of experiments have shown that the threshold for white light continuum is consistent with the critical power for SF^[131]. WL Smith^[132] focused picosecond laser with 1.06 and 0.53 μm wavelength into water and heavy water also showed the same critical power for SF and SC.

2.6.2 Polarisation dependent critical power

The effect of laser polarisation on critical power of SF has been observed by Gawelda et al ^[133] in fused silica. In Fig. 2.6-2, stable filaments were generated even with longest pulse duration (Fig. 2.6-2 (c)), while the filaments were suppressed with circular polarisation under the same conditions.

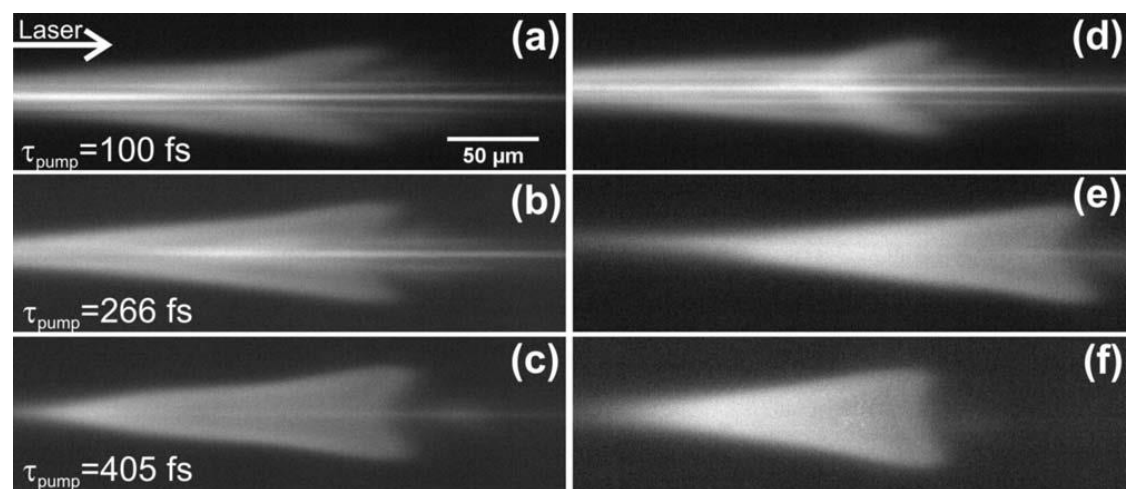


Fig. 2.6-2 Plasma emission images recorded for various pump pulse durations and various polarisation states (a–c) plasma emission images for linear polarization are shown, whereas (d–f) present plasma emission images for circularly polarized

laser from [133]

2.6.3 Numerical Solution of SF

The numerical solution of laser SF has been studied with different methods. The very first model was put forward by Kelly^[134] with the numerical solution put forward by J. H. Marburger ^[135,136]. For a Gaussian beam, the solution presents the relationship between incident laser power and length of SF was expressed as

$$\left(\frac{P}{P_2}\right)^{\frac{1}{2}} = 0.858 + 0.369 \frac{ka^2}{Z_f} \quad \text{Eq.2-12}$$

Where P is the incident laser power P_2 is the critical power for SF, wave number $k = \frac{2\pi}{\lambda}$, Z_f is the SF length and a is the radius of the beam. This basic form of the solution has been experimentally proved by C. C. Wang in organic liquids^[136].

Filamentation induced by fs laser has been demonstrated in different materials including gases, liquids and solids. For air, the critical power for SF is much higher, approximately 3GW. The experiments in fused silica ^[137,138] showed the dependence of filament length on laser pulse energy. From Fig. 2.6.3, the critical power can be estimated according to eq.2.6.3. with $n_2=3.54 \times 10^{-16}\text{cm}^2/\text{W}$, giving $P_{cr}=1.98\text{MW}$. This value has been confirmed ^[138] yielding $P_{cr}=1.72\text{MW}$ and $n_2=3.75 \times 10^{-16}\text{cm}^2/\text{W}$. In PMMA, D.Liu^[45] demonstrated the dependence of filament length on incident pulse energy at 775nm and 387nm where results were in agreement with an equation given by G. M. Zverev^[62]:

$$l_{fil} \propto \beta \sqrt{\left(\frac{n_2}{n_0}\right) (P - P_{th})}.$$

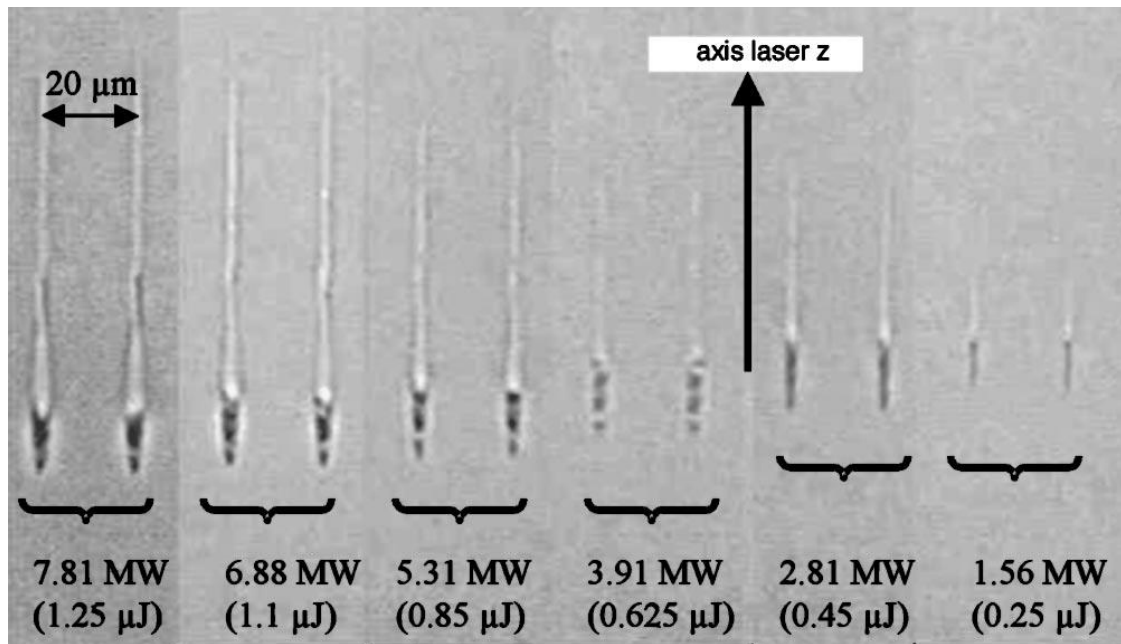


Fig. 2.6.3 the cross-section of the femtosecond laser induced filaments with various pulse energies from [137]

Chapter 3

NUV multiple laser beam parallel writing of VBGs in PMMA

3.1 Introduction

This chapter demonstrates the inscription of thick VBGs in clinical grade PMMA with parallel femtosecond laser beams at 387 nm, 170 fs pulse duration and 1kHz repetition rate. Phase hologram CGH's were generated in a Labview environment with the interactive Gerchberg-Saxton algorithm, generating 10 asymmetric near uniform, paraxial diffracted spots (Fig. 3.1-1). This asymmetry helps multiple beam uniformity as described in Section 2.5.4.2.

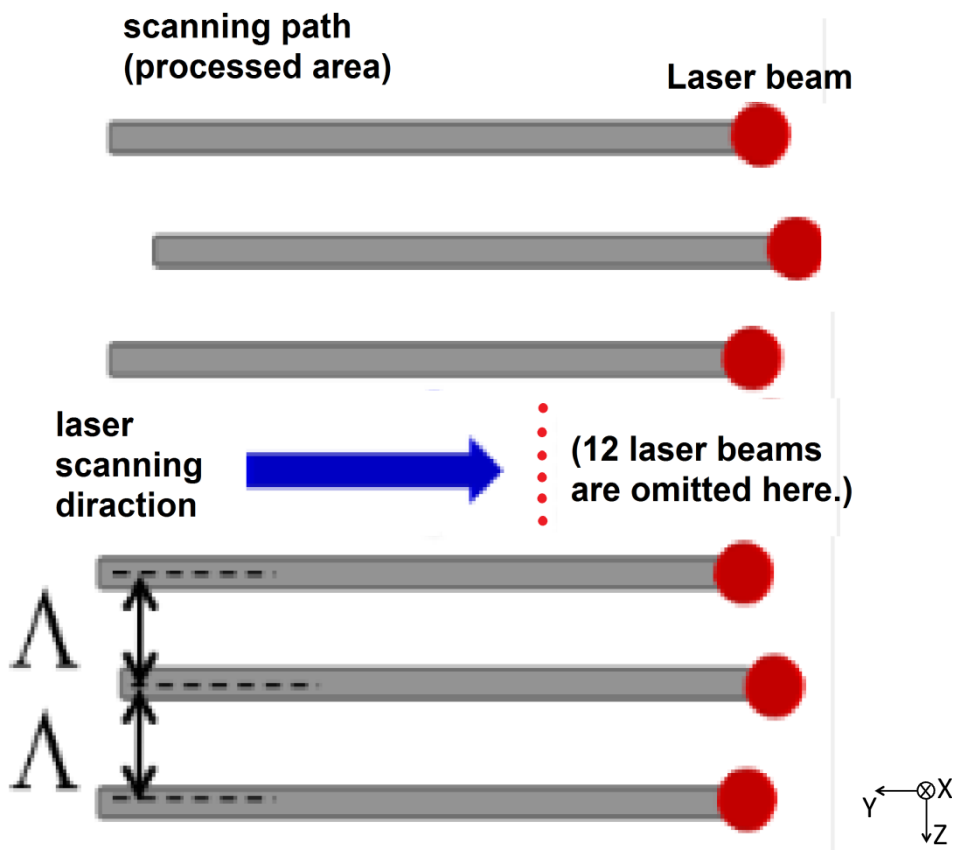


Fig. 3.1-1 Asymmetric multi-beam pattern for parallel processing. The blue arrow denote the translation direction (+Y) of the sample.

The fundamental laser output at 775nm was frequency doubled in beta- BaB_2O_4 to $\lambda_{2\omega} = 387\text{nm}$, creating vertical linear polarized NUV parallel beams. The thin BBO crystal was placed just after the SLM converting NIR parallel beams to NUV parallel beams. A series of VBGs with thickness from 1-7mm with pitch $\Lambda=22.3\mu\text{m}$ were inscribed horizontally at constant scan speed of 1mm/s.

3.2 Equipment

The femtosecond laser employed was a commercial system, a Clark-MXR CPA 2010 laser, generating NIR femtosecond laser pulses with a fundamental wavelength of 775 nm, a pulse energy of 1mJ, a pulse length of 170fs, a repetition rate of 1kHz, a beam quality factor M^2 of 1.3 and an output beam diameter of 6mm. The oscillator (mode locked Er:fibre at 1550nm) is frequency doubled to 775nm in periodically poled Lithium Niobate and seeds a Ti-Sapphire Regenerative amplifier. In addition, with a thin 0.6mm thick Beta Barium borate (BBO) crystal, the 775 fundamental wavelength can be frequency-doubled to the NUV beam with the wavelength of 387nm. The observed near Gaussian beam profile is shown in Fig. 3.2-1 measured with a Spyricon camera. The beam cross section in the amplified beam is slightly elliptical due to a small residual astigmatism.

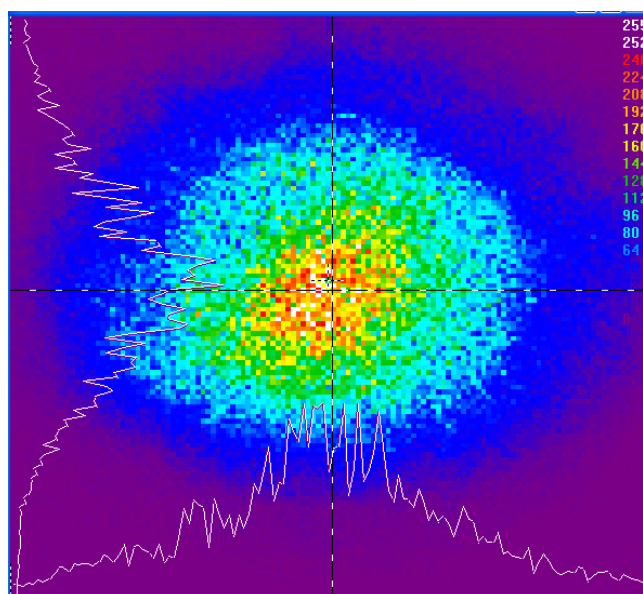


Fig. 3.2-1 Output Beam intensity profile of the femtosecond laser system, Clark-MXR CPA 2010.

The Hamamatsu X10468-02 phase only spatial light modulator (SLM), with a parallel aligned nematic liquid crystal (LC) on Silicon device has 800 x 600 pixels with 20 μ m pitch. Once a voltage is applied to the SLM, the LC molecules align horizontally along the optical axis, altering refractive index, so leading to a phase change of the incident light polarised along the molecular axis (director), while the light polarised perpendicular to the molecular axis is completely unaffected. An applied CGH consists of an 8 bit grey level map, each grey level applying a corresponding voltage (phase change) on each pixel. An incident plane wave thus undergoes diffraction by the applied CGH phase map. As described in Table 3.2-1, the X10468-02 is designed for a narrow range of wavelength 800 \pm 50nm, which provides 94% light utilisation efficiency and frame rate limited at 60 Hz. The reflective coating is a high damage threshold dielectric, able to handle peak intensity $I > 10\text{GWcm}^{-2}$ while the device can handle average power $P > 10\text{W}$.

Table 3.2-1 Specifications of the SLM

Model	Hamamatsu X10468-02
LC Type	Parallel aligned nematic
Number of input level	256 (8 bits)
Resolution (pixels)	SVGA (800×600)
Pixel pitch (μm)	20
Effective area (mm ²)	16×12
Mirror coating	Dielectric
Readout wavelength (nm)	800±50
Light utilisation efficiency*	94%
Fill Factor	95%
Response time** (rise/fall ms)	25/65
Frame rate (Hz)	60

*The actual light utilization efficiency is determined by the amount of diffraction loss caused by the pixelated structures and the reflectivity, which is affected by readout light wavelength.

**The response time is defined as the time required for the SLM to change from 10 % to 90 % for 2π modulation.

A software package was developed in LabVIEW environment based on the original package provided by Glasgow University developed for optical tweezers [139,140] (see Fig. 3.2-2). In the software interface, (Fig 3.2-2(a)), the green circles represent each diffracted beam which can be manually added and dragged to any desired positions. The red circle in the middle represents the zero order beam. All the circles only indicate the relative position of the diffracted beam but not the actual size. Calculated with Gerchberg-Saxton algorithm, the 8-bit greyscale CGH (Fig 3.2-2(b)) corresponding to the desired pattern was generated while

iteration rate depends on the complexity of the design. Then, the CGH was saved and subsequently displayed on the SLM to produce the multiple spots pattern at the focal plane of the lens.

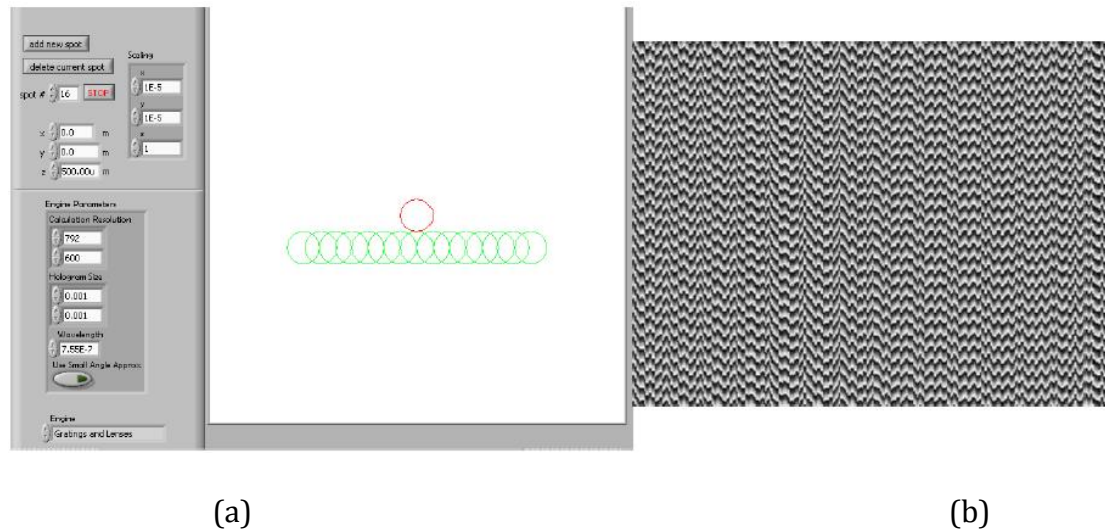


Fig. 3.2-2: (a) The original Labview interface with multiple spots pattern. The red spot in the middle represents the zero order beam. (b) The CGH generated using the GS algorithm in the Labview which will re-create the pattern.

3.3 Material

PMMA, the synthetic polymer of methyl methacrylate, is a transparent, versatile thermoplastic widely used as a photonic material due to its low cost, ease of processing and excellent optical performance. Due to its high transmission in the UV, visible and near IR spectral region, PMMA has been used as the core material for polymer optical fibre and the substrate for integrated optical devices.

The clinical grade bulk PMMA samples from Vista Optics used in this research

contain no additives and trace impurities. The PMMA has a density of 1.16g/cm^3 , a refractive index n_0 of 1.48 at 775 nm ($n_0 = 1.50$ at 387nm) and a glass transition temperature of 105°C to 120°C .

3.4 Experimental setup

The experimental setup is shown in Fig.3.4-1. A high energy variable diffractive attenuator was used to adjust the laser pulse energy continuously. After passing through the shutter and the beam expander with the magnification of 1.5, the horizontally polarised laser beam was reflected by the SLM at low angle of incidence addressed by an appropriate CGH. The reflected beams included the redundant zero order diffracted beam, first order diffracted beams, and remaining higher order diffracted beams with very low pulse energy, among which the first order diffracted beams could be used for processing. A thin BBO crystal ($8 \times 8 \times 0.7$ mm) was placed after and in close proximity to the SLM, converting the NIR beams to nearly collinear NUV beams. Then, a 4f optical system (with distance $AB=BQ=QC=CD = f = 200\text{mm}$, $AD=4f=800\text{mm}$ at 775nm) was introduced to eliminate the redundant zero order and the second or higher order diffractions at plane P, near the Fourier plane Q, by an absorbing target.

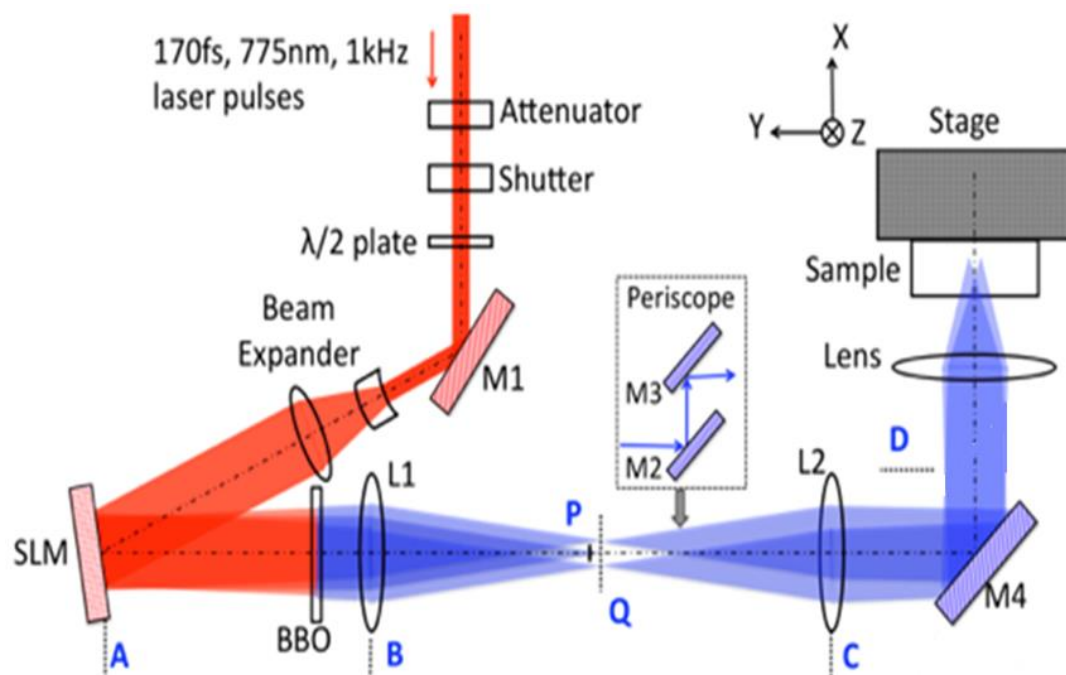


Fig. 3.4-1 Schematic of the experimental setup for NUV parallel processing

The first order diffractive beams were transmitted through the 4f system, reimaging the hologram addressed on the SLM to the back focal plane of a plano-convex lens with focal length $f = 50\text{mm}$ and $\text{NA} = 0.1$. The complex optical field at plane D was therefore identical with that at Plane A where the hologram was addressed to SLM. The PMMA substrates were mounted on a precision 3-axis motion control system (Aerotech) running under the controlling software NView MMI. Then, the 387 nm parallel beams were carefully focused $> 0.1\text{ mm}$ below the surface in order to keep the laser fluence at the interface of material and air below the damage threshold.

3.5 Diffraction efficiency measurement for VBGs

As illustrated in Fig. 3.5-1, a solid-state 532nm wavelength picosecond laser was utilized for probing the volume gratings. The laser beam passed through a volume grating sample which was mounted on a precision rotation stage. A silicon detector with power meter was placed at 1.5 meter away from the grating to measure the transmitted power into each order. The diffraction curves were measured by placing the detector in turn at the location of each diffracted order and rotating the grating from normal incidence.

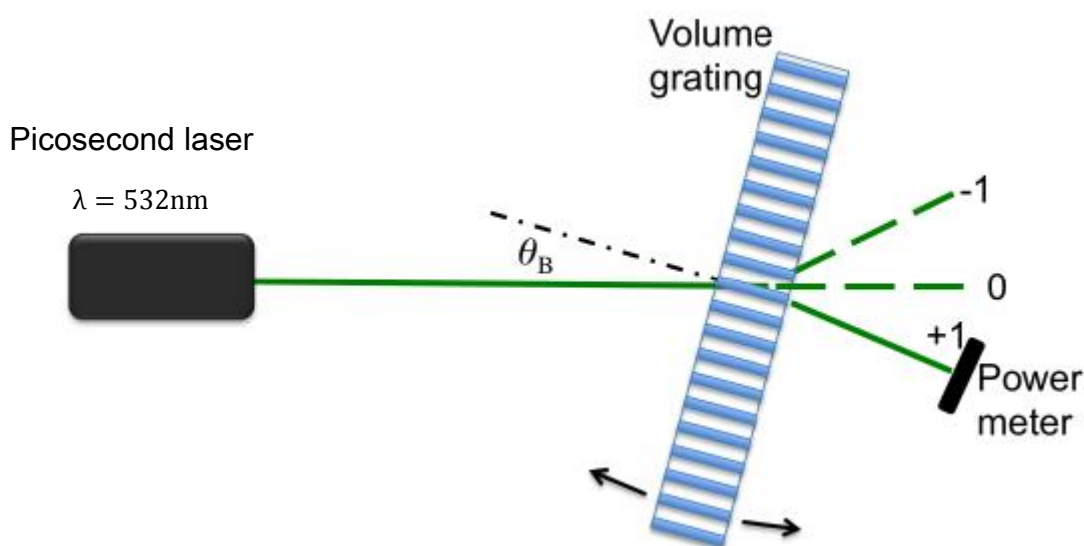


Fig. 3.5-1 Schematic of measuring the diffraction efficiency of volume gratings.

3.6 Multiple Laser Beam Direct Writing of VBGs

10 nearly uniform NUV beams were scanned transversely inside PMMA to produce refractive index modification with pulse energy $E_p = 0.35\mu\text{J}/\text{beam}$, and scan speed = 1mm/s, as shown in Fig. 3.6-1. As the pitch of the VBG was $\Lambda_1 =$

23.0 μm , the vertical distance between each horizontal scan was set to $\Lambda_2 = 230\mu\text{m}$, ten times of the grating pitch to produce a continuous, periodic vertical modification (z-direction). To inscribe thick 3D VBGs in the x-direction, along the optic axis, the 10 parallel beams were also scanned layer by layer, while overlapping the filamentary modifications, the deepest layer first. As the filaments had length $l = 370\mu\text{m}$, an offset of $\Delta X = 333\mu\text{m}$ along X axis was applied and a series of thick VBGs with dimension $5 \times 5 \times (1 - 7)\text{mm}^3$ were created. The ΔX offset was chosen to give a 10% overlap between layers to create a continuous and near uniform filament along the X-axis. A synchronized fast mechanical shutter was controlled within the Aerotech motion control software to avoid unwanted laser exposure of the material.

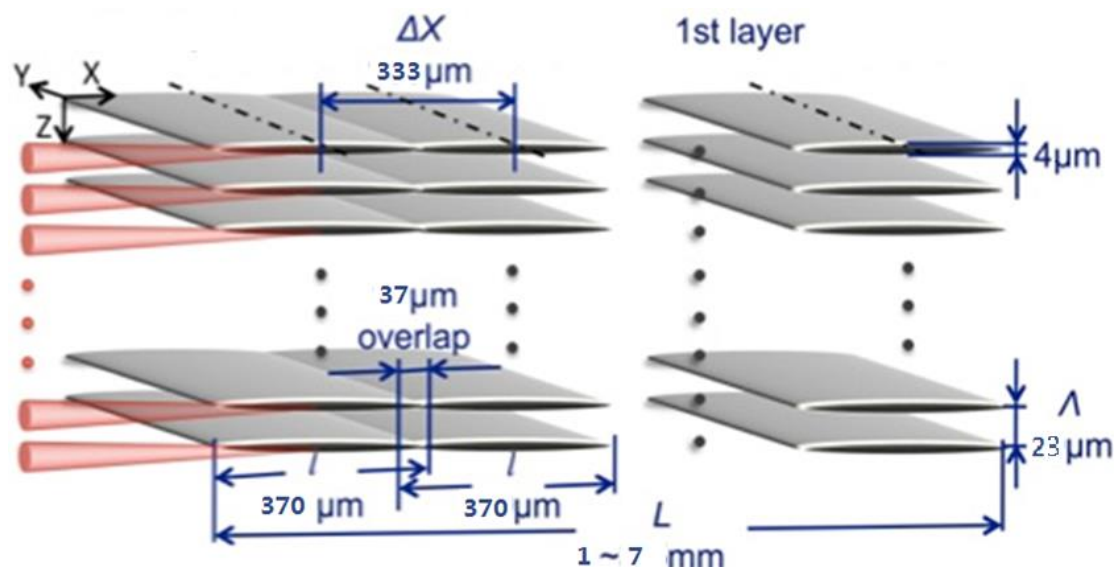
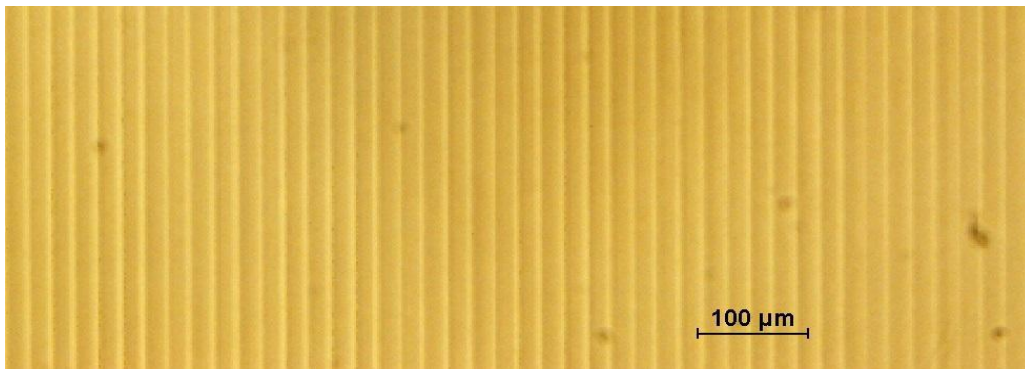


Fig. 3.6-1 Schematic of multi-beam modification to create continuous volume phase grating by stitching filamentary modifications with offsets $\Delta X = 333 \mu\text{m}$ and hence

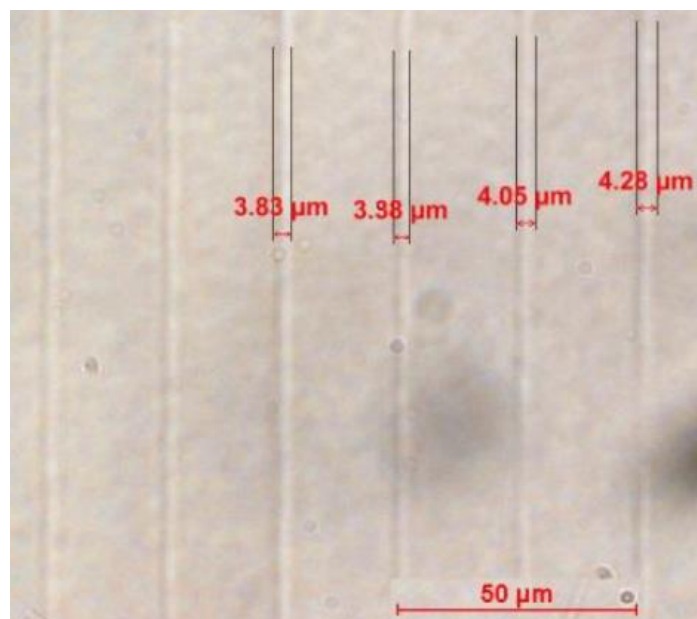
37 μm overlaps.

The size and quality of the filaments are measured under an optical microscope

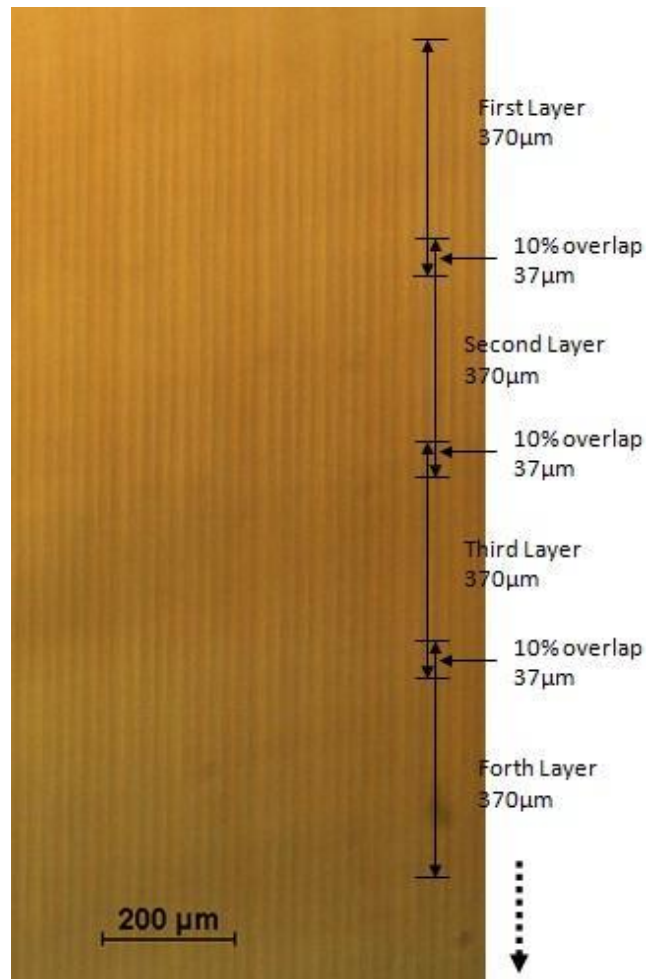
as shown in Fig.3.6-2(a). The filaments have good contrast and clear edges with the unmodified region which indicates a clear refractive index change in exposed regions and no crosstalk between adjacent filaments. The filaments are about 4 μ m in width, Fig. 3.6-2 (b). All the filaments are uniform with less than 10% difference in width. Fig.3.6-2 (c) demonstrates the good overlap between layers without separation and any obvious non-uniformity along the mm long filaments. Moreover, no optical breakdown is observed in the whole 3D structure.



(a)



(b)



(c)

Fig.3.6-2 (a) (b) Front view and (c) cross-sectional view of a thick VBG written with 10 parallel NUV beams. The volume grating consists of 9 layers with offsets $\Delta X = 333 \mu\text{m}$ ($37 \mu\text{m}$ overlaps) to create continuous modification and no discontinuities can be detected.

3.7 Measured Diffraction efficiency

Fig.3.7-1(a-c) shows the diffraction of transmitted beam at $\lambda = 532\text{nm}$ with 2mm and 5mm thick VBGs, after 30 days development. At normal incidence, the laser beam transmitted through the grating without diffraction, illuminating at the

position of zero on the wall as shown in Fig.3.7-1(a). Zero order appeared just above the black dot. Then, when the sample was slowly rotated around the vertical axis to the Bragg angle, the laser power diffracted to the first order with efficiency $\eta \sim 40\%$ (Fig. 3.7-1(b)). The 2mm thick VBG also showed a faint coupling to -1st order at the Bragg angle. With the same method, the 5mm grating showed high first order coupling with $\eta_1 > 90\%$ as shown in Fig. 3.7-1(c). However, there was clearly a remaining low background scatter, near the zero order. The scattered laser power was less than 0.5% of the total power, which was calculated as

$$P_S = P_t - P_{+1} - P_0 \quad \text{Eq. 3-1}$$

Where P_S is power in background scatter, P_t is the total incident power and P_{+1} and P_0 are the powers in +1 and 0 orders respectively.

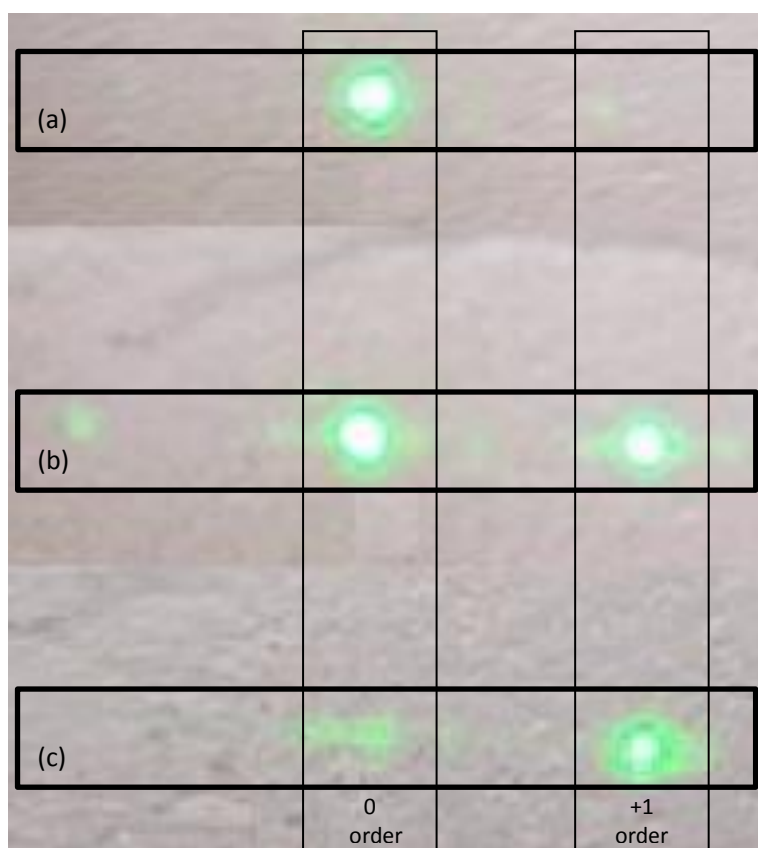


Fig. 3.7-1 Image of Bragg diffraction at $\lambda = 532$ nm (a) 2mm thick grating at normal incidence, (b) and (c) 0 and +1 order diffraction at the Bragg angle from the 2mm and 5 mm thick gratings respectively.

3.8 Thickness dependence of volume gratings

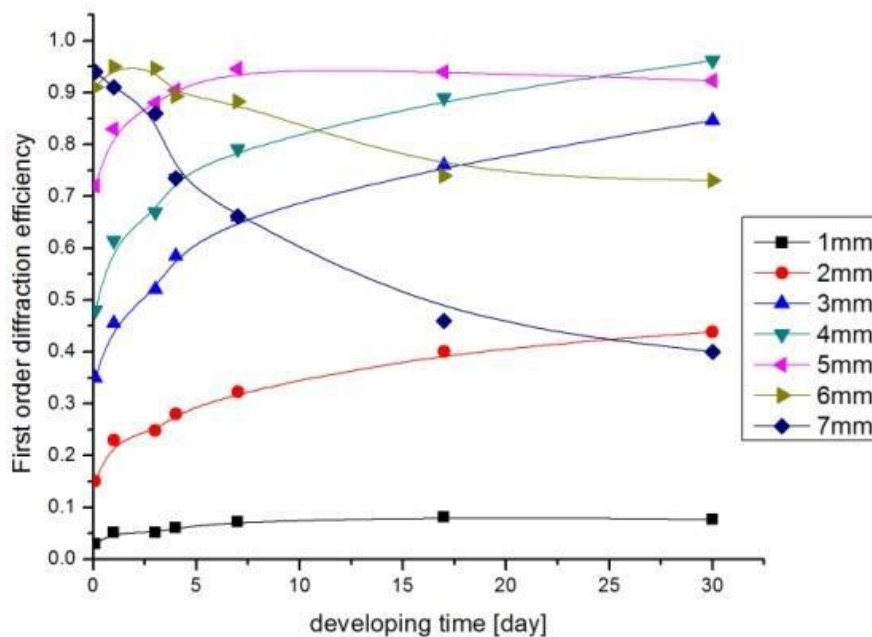
The first order diffraction efficiency can be simulated from the Kogelnik's theory equation,

$$\eta_{\pm 1} = \sin^2 \left(\frac{\pi \Delta n L}{\lambda \cos \theta_B} \right) \quad \text{Eq. 3-2}$$

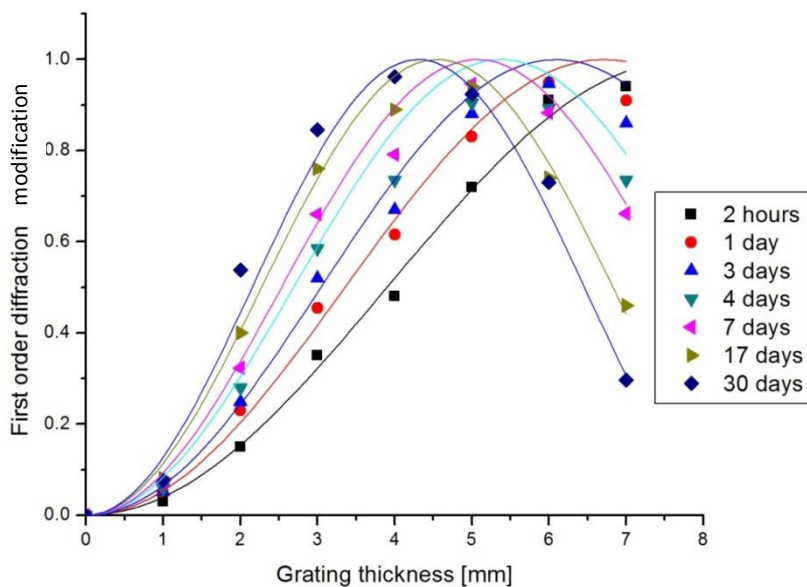
where Δn is the refractive index modulation, L is the grating thickness, $\lambda=532\text{nm}$ is the read out wavelength and θ_B is the Bragg angle. Fig.3.8-1(a) shows the measured Bragg diffraction efficiency of a series of gratings written under identical conditions with increasing thickness from 1mm to 7 mm measured from a few hours to 30 days after inscription.

As the refractive index change develops after inscription, gratings with thickness $L = 1\text{-}4\text{mm}$ increase monotonically with time as Δn rises. However, the gratings with $L= 5\text{-}7\text{mm}$ reach a maximum from hours to days then decay afterwards. The grating with $L = 7\text{mm}$ reaches its highest diffraction efficiency almost immediately after inscription (within hours) and decreases thereafter as RI modulation increases. The first order diffractive efficiency of the 4 mm thick grating reaches the peak at about 94% after 30 days. The source of the temporal variation will be discussed in Section 3.10

The theoretical fits based on Eq.3-2 (with fit parameter Δn) were drawn to calculate the refractive index modification of the gratings with time and thickness L (Fig.3.8-1b). Each curve represented the first order diffraction efficiency of the gratings with different thickness L (1-7mm) and same Δn , which was due to the same developing time. The results fit Kogelnik quite well, supporting a near uniform modification throughout the structures and highlighting the highest first order diffraction efficiency of $\eta_{max} = 94\%$ with the grating 4mm thick. The inferred RI modulation Δn reached 5.8×10^{-5} after 30 days. Also, the inferred optimum grating thickness is near $L \sim 4.5$ mm with the same processing parameter, where the diffraction efficiency near 100% could be expected. What worth mention is that the optimum thickness theoretically decreases with the increasing of pulse energy due to the higher induced Δn . However, the applicable upper constraint of the pulse energy is limited by the material breakdown threshold.



(a)



(b)

Fig.3.8-1(a) diffraction efficiency of gratings written with increasing thickness from 1mm to 7 mm measured at the Bragg angle from a few hours to 30 days after inscription (b) theoretical fit based on Kogelnik Theory with fit parameter Δn .

3.9 Bragg angular envelope of volume grating

Fig. 3.9-1 presents the measured first order Bragg angular envelope of a 5mm thick grating, measured at 532nm, 17 days after inscription and compared with the theoretical curve, [141].

$$\eta(\Delta\theta) = \frac{\sin^2(\pi L \left[\left(\frac{\Delta n}{\lambda} \right)^2 + \left(\frac{\Delta\theta}{\Lambda} \right)^2 \right]^{0.5}}{\left[1 + \left(\frac{\lambda \Delta\theta}{\Lambda \Delta n} \right)^2 \right]} \quad \text{Eq.3-3}$$

where L is the grating thickness, $\Delta n = \Delta n^{\text{lin}}$ is the refractive index modulation, $\Delta\theta$ is the angular deviation from the Bragg angle θ_B and Λ is the grating pitch. The agreement between experiment and theory is very satisfactory. The expected half width $\Delta\theta_{fwhm}^{\text{theory}} \approx \Lambda/L \approx 0.31^\circ$ while the measured FWHM $\Delta\theta_{fwhm}^{\text{exp}} = 0.29^\circ$.

The measured half width $\Delta\theta_{fwhm}^{\text{exp}}$ is very close to $\Delta\theta_{fwhm}^{\text{theory}}$ so that the envelope is almost the same as expected. The small difference may due to the slight angular divergence of the filaments which have a low but finite deviation error [35].

The measured peak diffraction efficiency is about 8% lower than theory, which was due to the slight scatters of the laser beam to the background as shown in Fig. 3.7-1. The efficiency peaks near $\theta_B = \sin^{-1} \left(\frac{\lambda}{2\Lambda} \right) = 0.68^\circ$ as expected. The

angular response also confirms that the grating is indeed a thick volume grating with thickness parameter [74] $Q = \frac{2\pi\lambda L}{n\Lambda^2} = 22.5$ with L= 5mm where $Q > 10$ is required for thick gratings. The VBGs were also found to be remarkably insensitive to polarisation direction, one of the attributes of VBGs.

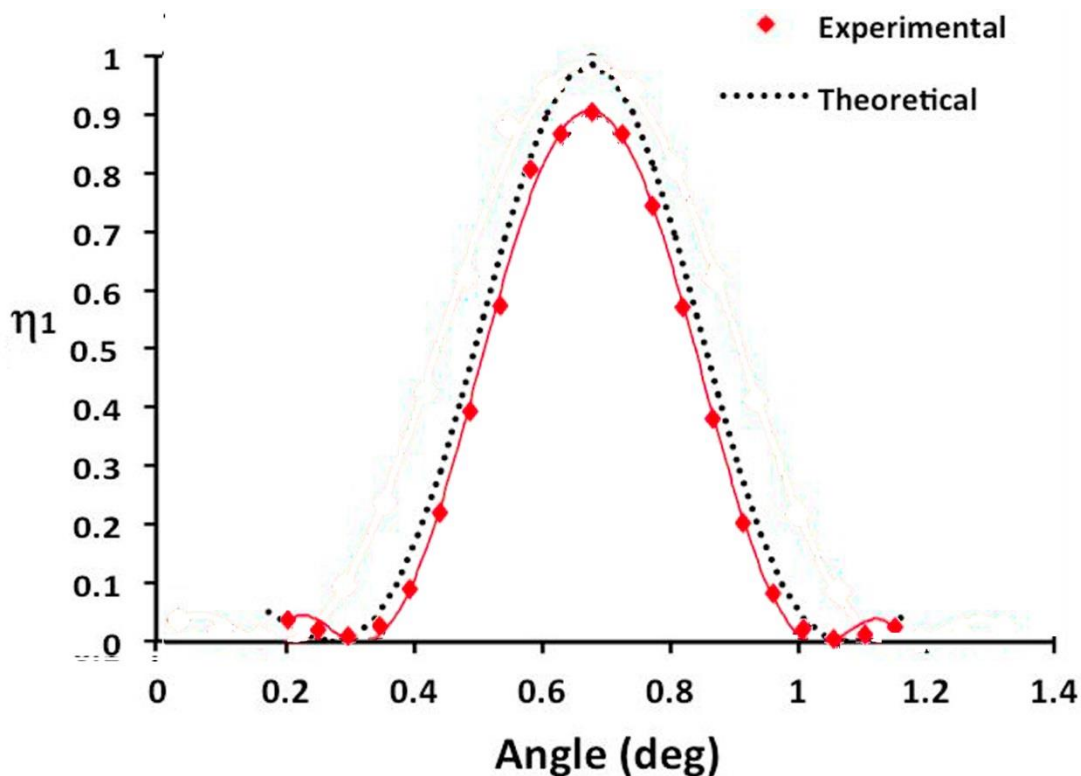


Fig. 3.9-1 the Bragg angular envelope of the 5mm thick VBG measured at 532nm, 17 days after inscription and comparison with theory. ^[141].

3.10 Time dependence of volume gratings

The refractive index change after inscription is time-dependent. The RI change was calculated from the theoretical fit, Eq. 3-2, where the dependence of the diffraction efficiency $\eta_{\pm 1}$ has only one unknown parameter, Δn . By adjusting Δn to give the best fit, the temporal development of the RI modulation could be determined and plotted in Fig.3.10-1. A large increase is observed in the first few days after inscription while stabilisation of the RI change occurs after 17 days.

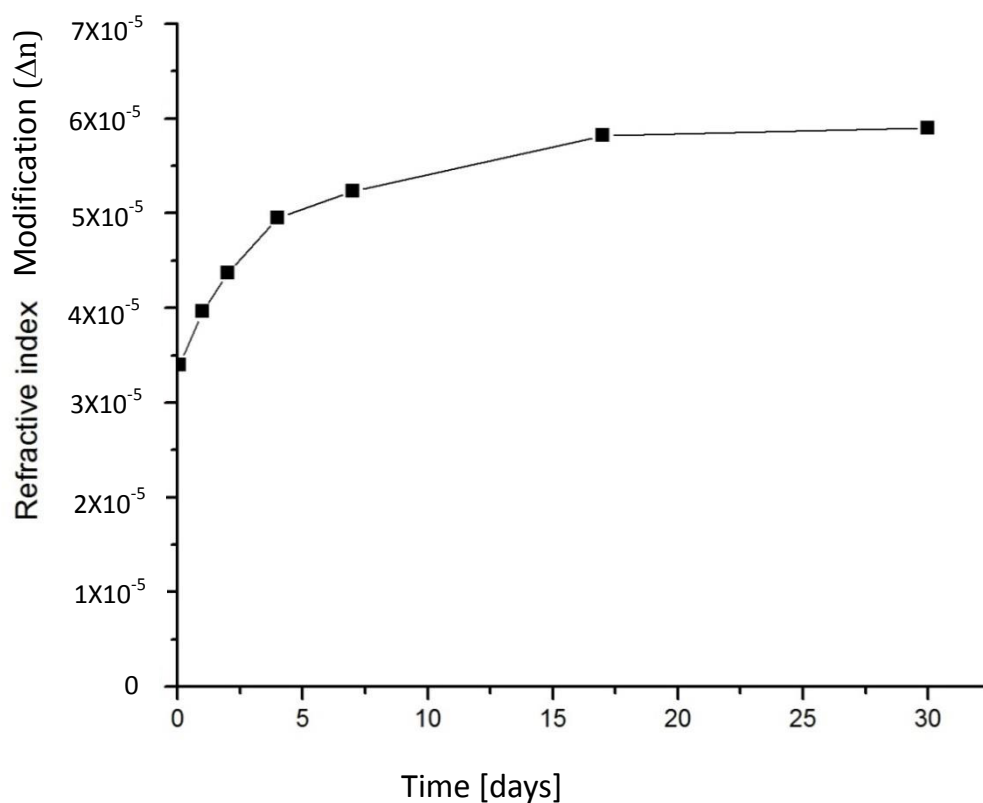


Fig. 3.10-1 the time dependence of the refractive index modification, showing stabilisation of refractive index n , 30days after exposure.

This temporal effect on the changing Δn in PMMA has been well documented by D.Liu^[45] and is due to:

- 1) Bond breaking in the PMMA chain via 2-photon absorption, generating MMA monomer, which can diffuse out into the surrounding regions between the filaments. This process takes many days to complete and gradually changes the density and optical properties of both the processed and unprocessed region after inscription.

- 2) More likely the C-C bonds. Partial crosslinking may occur between the ruptured chains, changing the structure in this volume.^[60] and increasing density (hence causing $+\Delta n$).
- 3) The stresses both from material expansion and stretching in the exposed region due to heat effect and the chemical change yield small density changes and hence a $+\Delta n$ inside the material. The relaxation of these stresses may also change the refractive index over time.

All these mechanisms contribute to the resulting time-dependent refractive index change Δn .

3.11 Production of VBGs with high density

A high density grating with pitch $\Lambda=5\mu\text{m}$ was produced with 30nJ pulse energy and $\text{NA}=0.4$. Due to the high filaments density and small filament dimension (length= $25\mu\text{m}$, width= $1\mu\text{m}$), a 5mm X 5mm X 1mm thick VBG took 17 hours for 10 parallel beams with $5\mu\text{m}$ pitch. To reduce the processing time, a new beam design was used.

As the SLM can generate parallel beams focussed at different planes by adding phase Fresnel lenses to the CGHs. Fig. 3.11-1 demonstrates the geometry of two layers (on x-axis) of beams with 10 beams (on z-axis) in each layer. Apart from a separation on x-axis, $\sim 20\mu\text{m}$, each layer has a small separation on y-axis to avoid the overlapping of laser beams.

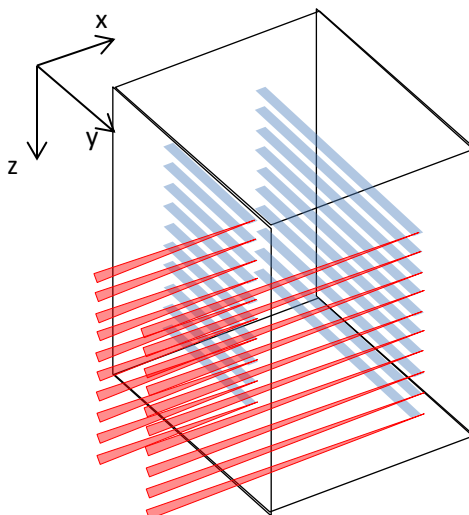


Fig. 3.11-1 Parallel writing inside PMMA. Transverse geometry for writing gratings in double layers.

5 layers of 10 parallel beams focused at different depth inside the material were generated to produce a 5mm X 5mm X 1mm thick VBGs layer by laser within 3.5 hours. The first order diffraction efficiency of this VBGs is about 10%. This efficiency was comparable to that measured with the 23 μ m pitch grating, however, inscription time is clearly a major issue combined with the fact that spherical aberration with thicker VBGs would severely limit uniformity

3.12 Summary

The SLM-generated parallel diffractive NUV beams were used to write high grade VBGs in PMMA with, 387nm, 1 kHz, 170 fs laser pulses. By carefully overlapping axial filaments layer by layer, along the optic axis, continuous uniform parallel filaments were inscribed throughout large volumes of the PMMA, resulting in a

series of VBGs with thickness from 1-7mm. Fabrication time for a 5 x 5 x 5mm thick VBG was ~45 minutes with 10 parallel spots, accelerating micro-fabrication greatly. This technique greatly increases the speed of production of 3D optical photonic components. The uniformity of the parallel beams was optimised by using an asymmetric spot pattern.

The VBGs of varying thickness show a good fit of diffraction efficiency when compared to Kogelnik's theory. The grating with 4 mm thickness demonstrates the highest first order diffractive efficiency η_{+1} up to = 94% and inferred $\Delta n \sim 5.8 \times 10^{-5}$ after ~30-days. The measured Bragg angular envelope is similar but wider by a factor of 1.3 when compared to first order theory, due to the small divergence of the filaments relative to the optic axis. Although the temporal changes in refractive index are observed after material inscription with fastest rise within the first few days, the RI modulation tends to stabilise after 17 days.

Chapter 4

Polarisation dependent filamentation

4.1 Introduction

The effect of inscription polarisation affected the processing efficiency and was investigated. VBGs were produced with 4 polarisation states: linear horizontal $|H\rangle$ (with the same direction of scanning), linear vertical $|V\rangle$ (vertical to scanning direction) and circular $|R\rangle$ and $|L\rangle$. Differences in the first order diffractive efficiency would infer that polarisation is an important parameter during inscription.

4.2 Effect of polarisations on writing VBGs at 387nm

A series of 5mm thick VBGs were inscribed with 10 parallel spots under four polarisation states: $|V\rangle$, $|H\rangle$, $|R\rangle$, $|L\rangle$. Table 4.2-1 summarises the measured first order Bragg efficiencies of the 5mm thick VBGs generated, 9 days after inscription. First order diffractive efficiency was highest with linear vertical polarisation $|V\rangle$, then linear horizontal $|H\rangle$. The circular polarisation $|R\rangle$ and $|L\rangle$ show a lowest efficiency with $\eta_{1|L\rangle} = \eta_{1|R\rangle}$ within experimental error, as expected from symmetry.

Linear polarisation states clearly couple more strongly to the material. While $\eta_1(|V\rangle) - \eta_1(|H\rangle) \sim 5\%$ the highest difference $\eta_1(|V\rangle) - \eta_1(|R\rangle) \sim 8\%$ corresponding to $\delta(\Delta n) = 6\%$ and 9% respectively. The total pulse energy was monitored carefully throughout the inscription of the set of 4 VBGs and

maximum variation in pulse energy $\frac{\Delta E_p}{E_p} = \frac{0.02\mu\text{J}}{3.12\mu\text{J}} = 0.64\%$ where E_p is the total pulse energy for 10 spots.

Table 4.2-1 1st order diffractive efficiencies 9 days after inscription with various polarisations

Polarisation	η_1 (L=5mm)	Inferred Δn
$ V\rangle$	0.92 ± 0.02	$(4.35 \pm 0.13) \times 10^{-5}$
$ H\rangle$	0.87 ± 0.02	$(4.07 \pm 0.10) \times 10^{-5}$
$ R\rangle$	0.84 ± 0.02	$(3.92 \pm 0.10) \times 10^{-5}$
$ L\rangle$	0.85 ± 0.02	$(3.97 \pm 0.10) \times 10^{-5}$

The time dependence of refractive index modification has been introduced in Chapter 3. The measured ratio $\eta_1(|V\rangle)/\eta_1(|R\rangle)$ was time dependent and results shown in Fig.4.2-1. Thus, $[\eta_1(|V\rangle)/\eta_1(|R\rangle)]_{max} = 1.21 \pm 0.03$, shortly after inscription, which decays to 1.09 ± 0.02 after 9 days as the VBGs develop.

Although the refractive index modification tends to be stable with time, this value changed from 5.4×10^{-5} to 5.8×10^{-5} (9% growth) with time increasing from 9 days to 30 days for linear polarisation (Fig.3.7-1). This growth for circular polarisation may differ from linear polarisation, further reducing the rate $\eta_1(|V\rangle)/\eta_1(|R\rangle)$. Therefore, more experiments are required to investigate $\eta_1(|V\rangle)/\eta_1(|R\rangle)$ for the extended period of time after 9 days. However, the dependence of refractive index modification on polarisation is still convincing as

shown in Fig. 3.7-1..

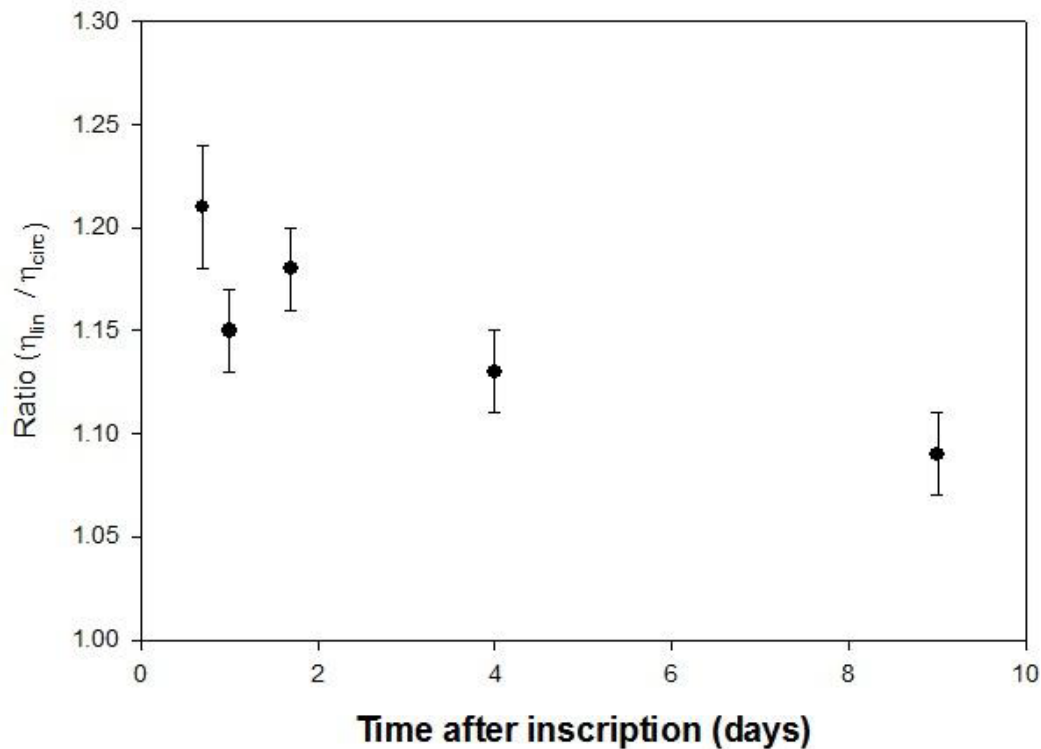
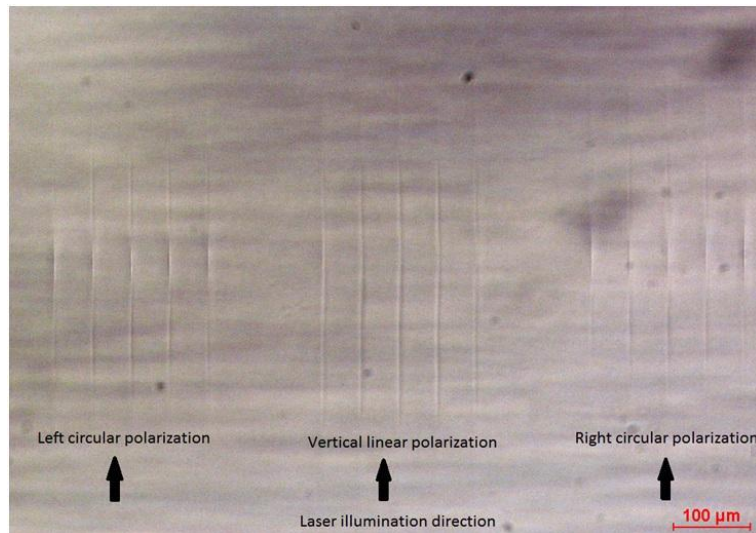


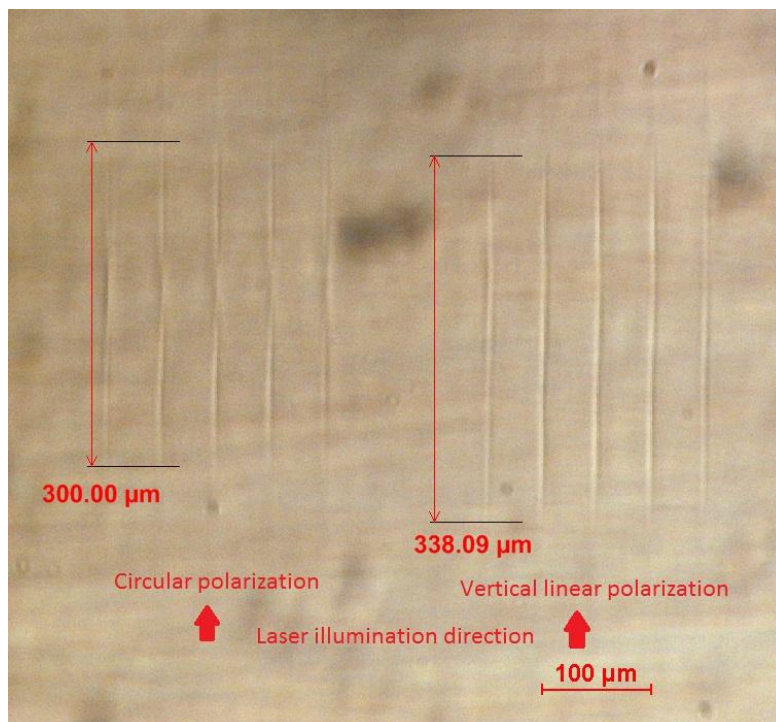
Fig. 4.2-1 time dependence of ratio $\eta_1(|V\rangle)/\eta_1(|R\rangle)$

The polarisation dependence in inscribing VBGs in PMMA with NUV fs laser infers a polarisation dependent filamentation. A series of filaments were inscribed under pulse energy $E_p = 0.301 \pm 0.001 \mu\text{J}$. The detector response (J3-05, Molectron) was checked carefully and determined to be independent of polarisation within experimental error. The polarisation was altered using either a zero order half wave for linear or quarter wave plate for circular, placed just ahead of the objective. Fig. 4.2-2,(a) shows the observed filament cross-sections with linear and circular polarisations inscribed at a depth of 2mm inside PMMA. There is clearly a significant difference in filamentary modifications. With linear polarisation, inscribed filaments appear more uniform,

to have higher refractive index contrast than circular polarisation ($\Delta n^{lin} > \Delta n^{circ}$), while also originating nearer the laser source by around $\Delta L \sim 40 \mu\text{m}$. (Fig. 4.2-2(b)). As expected from symmetry, right and left polarisations generate similar modifications. Circular polarisation also shows a short, higher contrast region ($\Delta n^{circ} > \Delta n^{lin}$ near $z \sim z_0$) where self-focussing appears to overcome plasma de-focussing, leading to filamentation collapse, then the plasma density rises again, filamentation recovers and a dynamic balance is re-established. From the observed filament contrast, however, in general, $\Delta n^{lin} > \Delta n^{circ}$. Filamentation differences were less obvious as inscription depth was increased beyond 4mm but still apparent even at 6mm depth. Therefore, the filamentation has experimentally shown to be polarisation dependent where the strength of SF by linear polarisation is higher than with circular polarisation.



(a)



(b)

Fig. 4.2-2 image of (a) the cross-section of polarisation dependent filamentation in PMMA inscribed by femtosecond laser at 387nm with linear $|V\rangle$ and circular $|R\rangle$ and $|L\rangle$ polarisations states. Inscription depth is 2mm below the PMMA surface. (b) measurement of filament length induced by laser with linear $|V\rangle$ and circular $|R\rangle$ polarisation states at higher magnification.

As filamentation is the result of the dynamic balance of Δn between self-focusing (SF) and plasma defocusing, the relationship between the third order susceptibility and nonlinear refractive index is given by, [144]

$$n_2 = \frac{0.0395\chi^{(3)}}{n_0^2} \quad \text{Eq. 4-1}$$

where n_2 has units cm^2W^{-1} and $\chi^{(3)}$ is measured in esu. In optical solids, the value of $\chi^{(3)}$ is typically in the range $10^{-13} - 10^{-14}$ esu [133]. For example, the value of $\chi^{(3)}$ in PMMA at $\lambda = 1500\text{nm}$ was estimated to be [102] $\chi^{(3)} \sim 3 \times 10^{-14}$ esu and as $\chi^{(3)}$ scales linearly with wavelength, then $\frac{\chi_{387}^{(3)}}{\chi_{1500}^{(3)}} = 0.258$ yielding $\chi_{387}^{(3)} \sim 7.7 \times 10^{-15}$ esu hence $n_2^{387} \sim 1.37 \times 10^{-16} \text{cm}^2\text{W}^{-1}$.

According to Eq.2.2, the critical power for self-focussing in PMMA is therefore $P_c \sim 1.1\text{MW}$ while the peak power in each beam $P = 1.7\text{MW} \sim 1.5P_c$ and confirms that self-focussing will occur ahead of the geometrical focus inside the material. According to Boyd[143] $n_2^{\text{lin}}/n_2^{\text{circ}}=1.5$ in a pure dielectric, the critical power for SF with linear and circular polarisation is therefore $P_c^{\text{circ}}/P_c^{\text{lin}} = 1.5$ according to Eq. 2-2

4.3 Experimental setup

As polarisation was clearly critical to the non-linear filamentation process, this was studied at the fundamental wavelength (775nm) where the effect of cylindrical vector polarisations could also be studied. Since the critical power for SF (SF) is identical with that for supercontinuum (SC) generation, the thresholds

for SC and hence SF were determined.

4.3.1 Femtosecond laser polarisation modulation

The fundamental set up at 775nm was altered to create 6 states of polarisation with the aid of quarter and half wave plates (vertical linear $|V\rangle$, perpendicular to scanning direction, horizontal linear $|H\rangle$, parallel to scanning directions, right circular $|R\rangle$, left circular $|L\rangle$) and combining linear polarisations at 45° with vortex phase CGHs and a quarter waveplate to generate radial $|R_a\rangle$ and azimuthal $|A_z\rangle$ polarisations. (see Fig. 4.3-1)

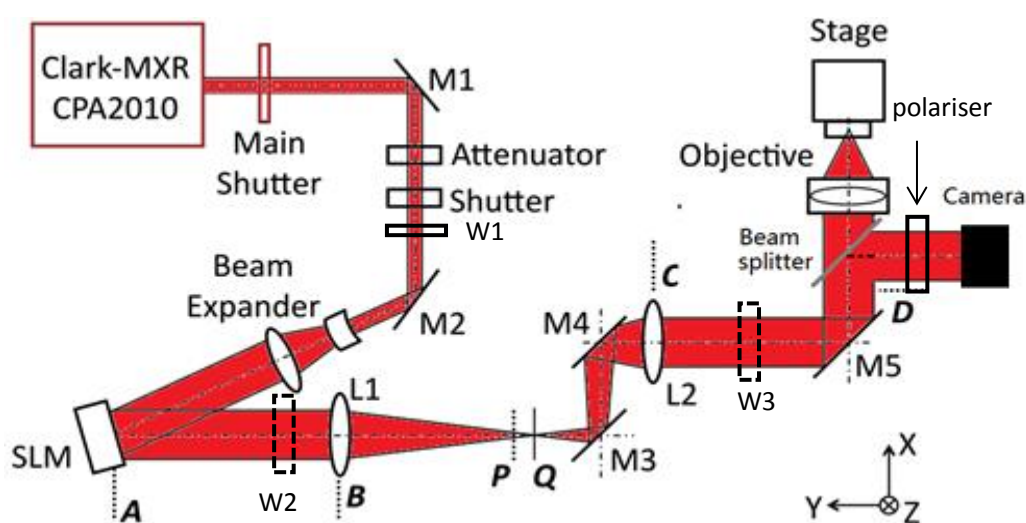


Fig. 4.3-1 Schematic of the experimental setup for NIR parallel processing at various polarisation states

Referring to Fig4.3-2, for horizontal linear, vertical linear and circular polarisations, a black hologram (fixed phase) was addressed onto the SLM working as a mirror. For linear polarisations, the half-wave plate placed at W3

was rotated from the horizontal to 45° with W2 removed. For circular polarisations, the quarter wave plate placed at W2 was rotated to $\pm 45^\circ$ with W3 removed.

The generation of vortex azimuthal and radial polarizations requires a vortex phase shift hologram ($0-4\pi$) combined with half wave plate W1 and quarter waveplate at W2 with W3 removed. The W1 fast axis was adjusted to 22.5° to the vertical direction, thus rotating the incident polarization 45° to the horizontal on the SLM. With the vortex phase diagram ($0-4\pi$) applied and the quarter wave plate fast axis at 45° to the horizontal, the polarization state can be switched between azimuthal and radial by rotating the orientation of the spiral phase hologram within LabVIEW.

The polarisations of the laser beam were monitored by the CCD camera, prior to which a polariser was used with transmission axis horizontal. The beam profiles at various polarisation statuses captured by the camera are shown at the bottom of Fig. 4.3-2.

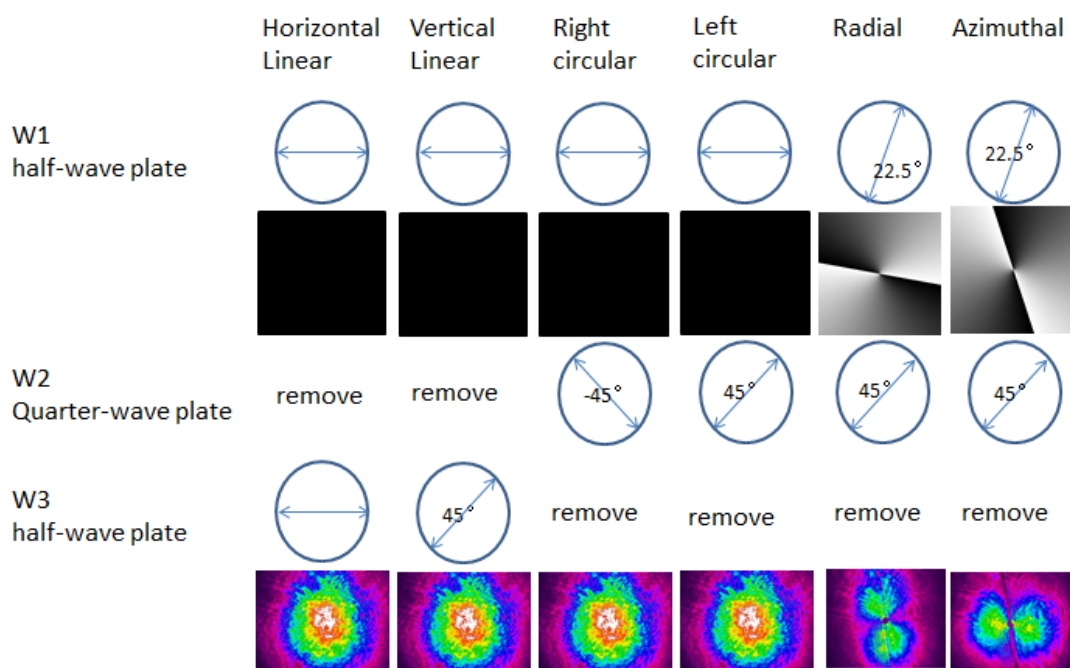


Fig. 4.3-2 selection of hologram and waveplate orientations for generating horizontal linear, vertical linear, right circular, left circular, vortex radial and vortex azimuthal polarisations. The camera images are those analysed after a polariser with transmission axis horizontal.

4.3.2 Measurement of white light continuum

Illuminated by the 775nm femtosecond laser, the white light continuum was generated in PMMA (Fig. 4.3.3) by focusing the fs beam 2-3mm inside. The sample was mounted on the side of the z axis-stage and scanned continuously in a raster pattern at 10mm/sec to ensure that a new spot was exposed with every pulse. The diverging light behind the sample, containing the continua and the original 775nm wavelength laser, was focused by a lens with 50mm focal length to the fibre connector for the spectrometer.

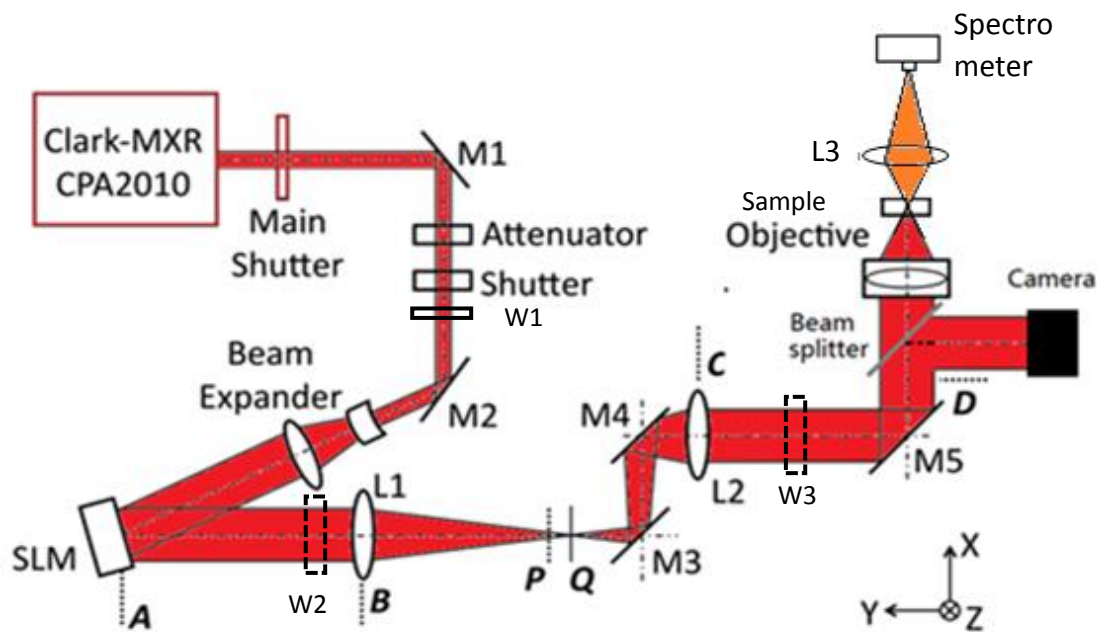


Fig. 4.3-3 Experimental setup for the analysis of the continuum generation by 775 nm pulses at various polarisations. PMMA Samples were scanned in the Z-axis

The SM240 is a compact CCD Spectrometer used to measure the spectrum of the white light continuum generated in PMMA when focusing femtosecond laser pulses. This spectrometer accepts light via optical fibre and fibre coupler. The standard sensor arrays used are the Sony ILX 511 which has been designed for highly sensitive yet stable operation, allowing up to 850nm wavelength measurement. In addition, the spectrometer applies new UV enhancing coating on the CCD to increase the UV sensitivity below 450nm.

4.4 Polarisation dependent critical pulse energy for SC

Fig. 4.4-1 shows the spectrum of the NIR femtosecond laser and the spectrum (red line) generated in PMMA detected after focusing a pulse energy of $2\mu\text{J}$ in the material at 0.08NA. The laser beam has a bandwidth $\Delta\lambda_{\text{FWHM}} = 8\text{nm}$ and 16nm

at base of the spectrum, while the super-continuum has a wavelength ranging from 761nm to 797nm measured at the base, hence 36nm wide. The spectrum was quite stable with less than 5% variation. In addition, a red shift of the peak intensity from 775nm to 783nm in the white light continuum was observed. This broadening of the laser spectrum to longer (Stokes shift) and shorter wavelengths (Anti-Stokes) is a characteristic SC which broadens massively as pulse energy is increased.

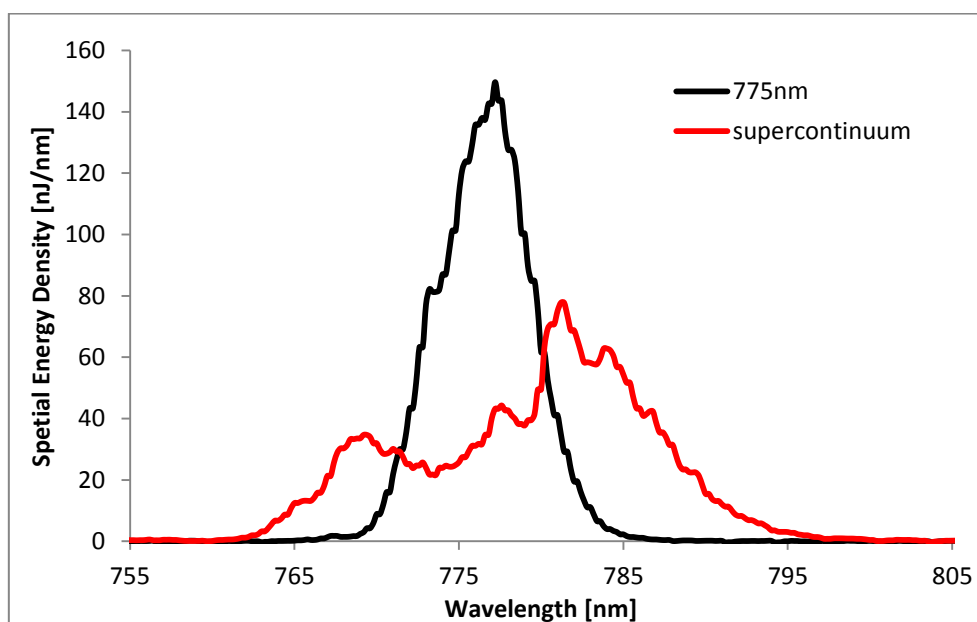


Fig. 4.4-1 spectrum of 775nm femtosecond laser $|V\rangle$ (black) and the induced SC spectrum in PMMA at 2000nJ pulse energy (red)

Fig. 4.4-2 shows the measured left wing (blue shift) of the SC spectrum generated with linear $|V\rangle$ and circular polarisation $|R\rangle$ states and with 200nJ (1.1MW) and 1000nJ (5.5MW) pulse energy. For 200nJ pulse energy, (very near the SC threshold), the spectrum of linear polarisation overlaps with that of circular polarisation with a separation of less than 1nm. However, when the pulse energy

was increased to 1000nJ, a clear separation with about 5nm was obtained at the base of the spectrum. A beam with linear polarisation $|V\rangle$ generates a wider spectrum than with circular $|R\rangle$ indicating a higher coupling efficiency for linear state. The polarisation dependence of the SC is therefore clearly demonstrated.

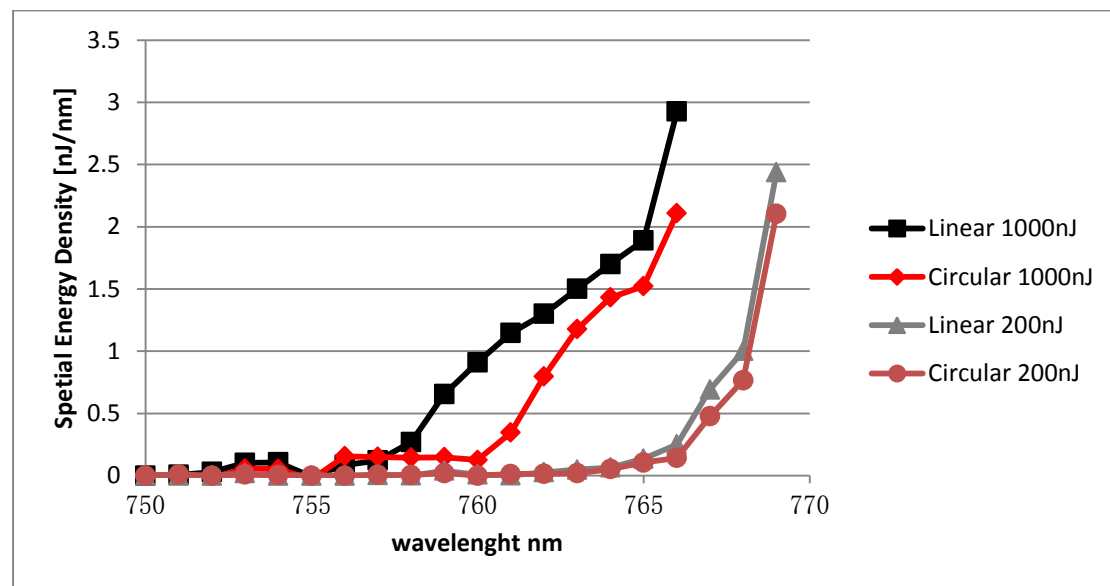


Fig. 4.4-2 left wing of the spectrum of the SC generated with linear $|V\rangle$ and circular polarisation $|R\rangle$ and with 200nJ (near threshold) and 1000nJ (above threshold) pulse energy respectively.

To compare the SC thresholds for different polarisations, the blue left wing of the SC spectra induced with 4 polarisation states, vertical linear $|V\rangle$, right circular $|R\rangle$, vortex azimuthal $|Az\rangle$ and vortex radial $|Ra\rangle$, were integrated over the wavelength range of 750nm-760nm which covers the , while pulse energy was varied from 200nJ to 1300nJ (Fig. 4.4-3). With low pulse energy < 300nJ (1.6MW), no SC was induced. As pulse energy increases, the curve for $|V\rangle$ starts to increase first followed by $|R\rangle$ and finally the $|Az\rangle$ and $|Ra\rangle$. The thresholds

for SC can be estimated from the rising edges of the curves. Therefore, the vertical linear polarisation $|V\rangle$ has the lowest critical pulse energy at about 400nJ (2.2MW), followed by $|R\rangle$ at about 500nJ (2.8MW) and finally $|Ra\rangle$ and $|Az\rangle$ states with equal energy at about 1000nJ (5.5MW). The ratio of critical powers for linear and circular polarisation is therefore $P_c^{\text{CIRC}}/P_c^{\text{LIN}} \sim 1.25$ from this data. The much higher thresholds observed for Radial and Azimuthal states (with a vortex wavefront) is very interesting, however, part of this may be due to a slightly lower beam quality created by the method of generating these states with the SLM.

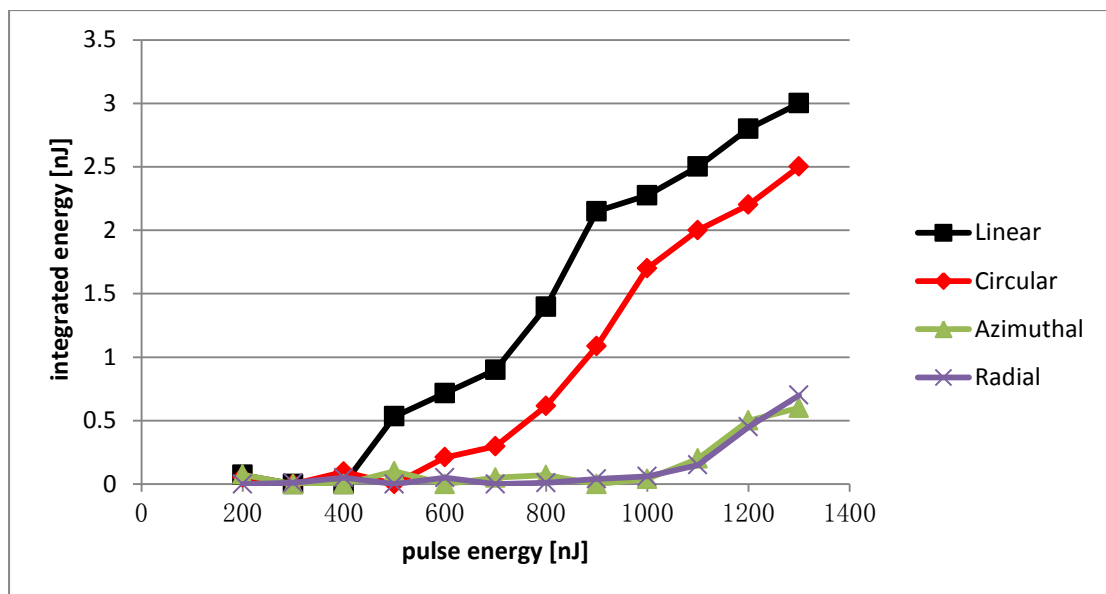
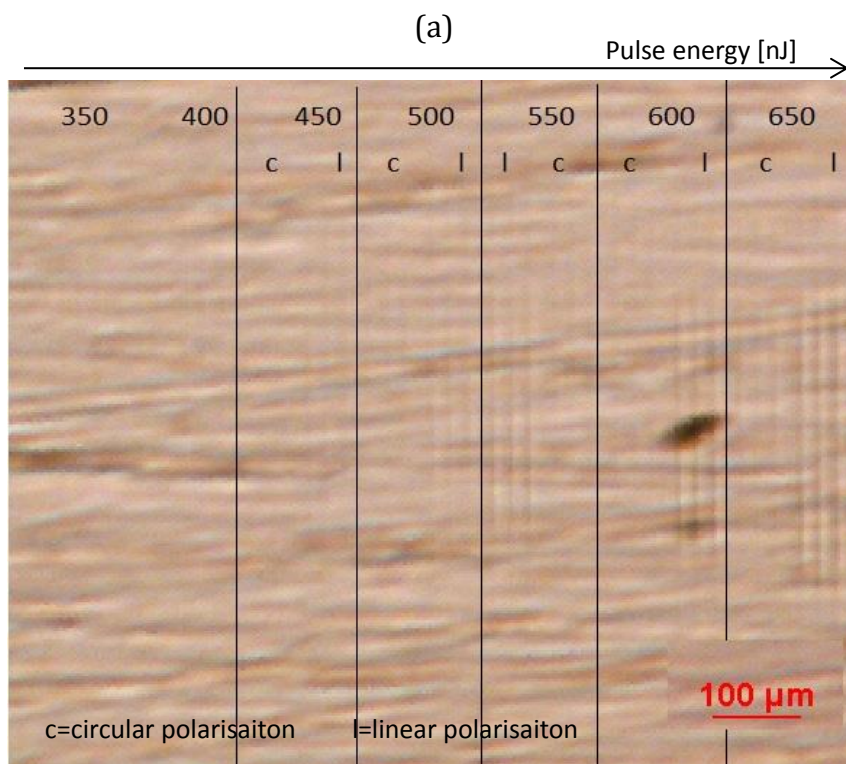
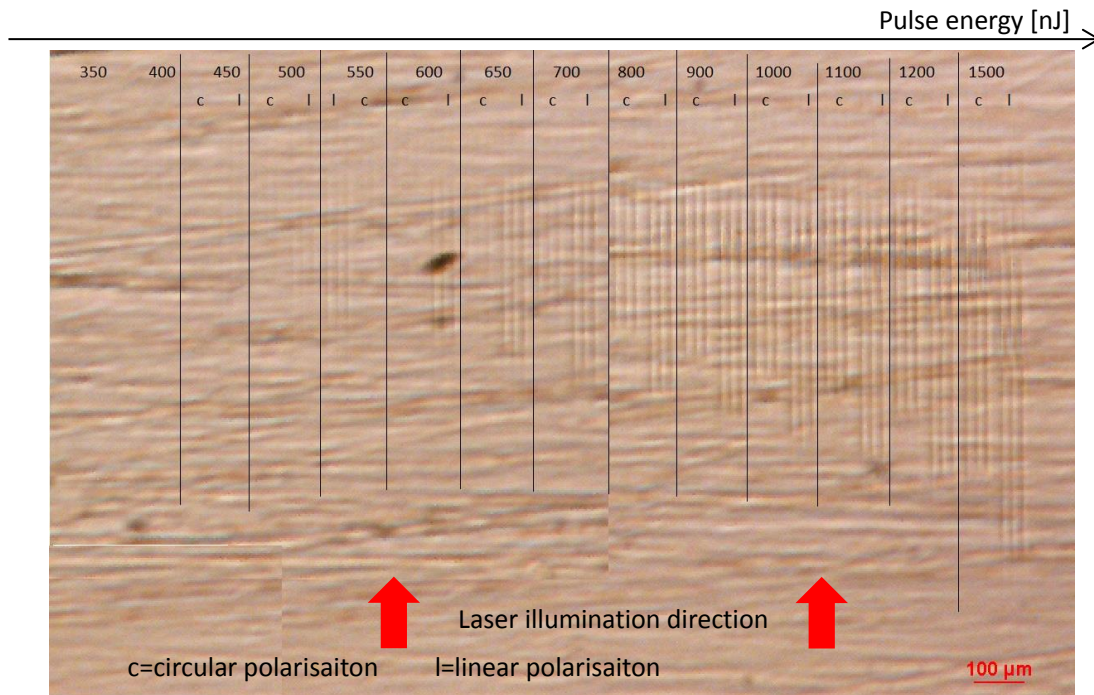


Fig. 4.4-3 integrated pulse energy, distributed from 750nm to 760nm in the spectrum of the SC generated with four polarisation states: $|V\rangle$, $|R\rangle$ $|Az\rangle$ $|Ra\rangle$, shows clear evidence of polarisation dependent critical power for SC and hence SF

4.5 Polarisation dependent critical power for filamentation in PMMA at 775nm

A series of filaments were produced in PMMA by 775nm femtosecond laser (NA=0.1). The scanning speed was 1mm/second and the pulse energy ranged from 350nJ (1.94MW)-1500nJ (8.33MW). The polarisation was switched between linear $|V\rangle$ and circular $|R\rangle$ or $|L\rangle$. The cross-section of the filaments are shown in Fig. 4.5-1(b) where the pulse energy thresholds for filamentation are $\sim 450\text{nJ}$ (2.5MW) (linear) and 650nJ (3.6MW) (circular) hence a ratio of critical powers $R \sim 1.4$. In Fig. 4.5-1(a) The starting point of the filaments produced by linear polarisation, which is the tip of the filament towards the laser source, is closer to the surface of the material than that produced by circular, supporting the argument that linear polarisation has lower critical SF threshold than circular polarisation.



(b)

Fig.4.5-1 cross-section of the filaments in PMMA induced by femtosecond laser with pulse energy (a) 350-1500nJ (b) 350-600nJ with linear and circular polarisation states.

4.6 Effects of polarisation on transmitted pulse energy through PMMA at 775nm

An additional method to estimate SF thresholds at 775nm was carried out in PMMA as follows. The scanning method is the same as that in the previous experiment, but the spectrometer after the sample was replaced with a pulse energy meter to measure the transmitted pulse energy with increasing incident pulse energy (as introduced in Section 4.3.3). The absorbed pulse energy is mainly composed of two parts: 1) linear absorption by the material when the pulse energy is lower than critical pulse energy for filamentation, 2) nonlinear absorption by the material when the pulse energy is higher than critical value. For PMMA, the linear absorption is negligible since the material is transparent at 775nm (and 387nm.) Therefore, all the non-linearly absorbed pulse energy contributes to the generation of a filament. The pulse energy transmission was measured every 50nJ from 200nJ-600nJ and every 100nJ from 600nJ-1200nJ. The results are plotted in Fig.4.6-1. A clear polarisation dependent effect is again observed using this approach.

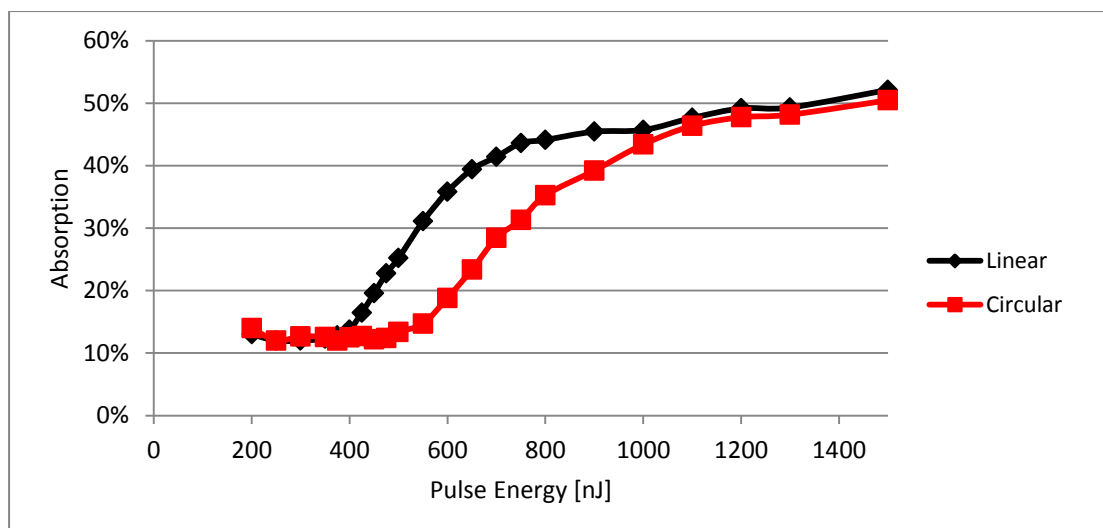


Fig. 4.6-1 absorption rate of focused NIR femtosecond laser by PMMA with pulse energy and with linear and circular polarisations $|V\rangle$ and $|R\rangle$

By locating the data point where the absorption start to increase, we estimate the threshold energies in PMMA at which absorption increases to be about 394nJ (2.2MW) and 544nJ (3.0MW) for linear and circular polarisations respectively. The ratio of critical powers is therefore approximately 1.38, close to the theoretically expected ratio of 1.5. A comparison of the measured polarisation dependent filament length and corresponding absorbed energy is shown in Fig. 4.6-2. These are clearly correlated. The pulse energy threshold for filamentation with linear polarisation is ~400nJ (2.2MW), while it is ~600nJ (3.3MW) for circular polarisation and thus inferring a ratio close to 1.5 which is in agreement with theory.

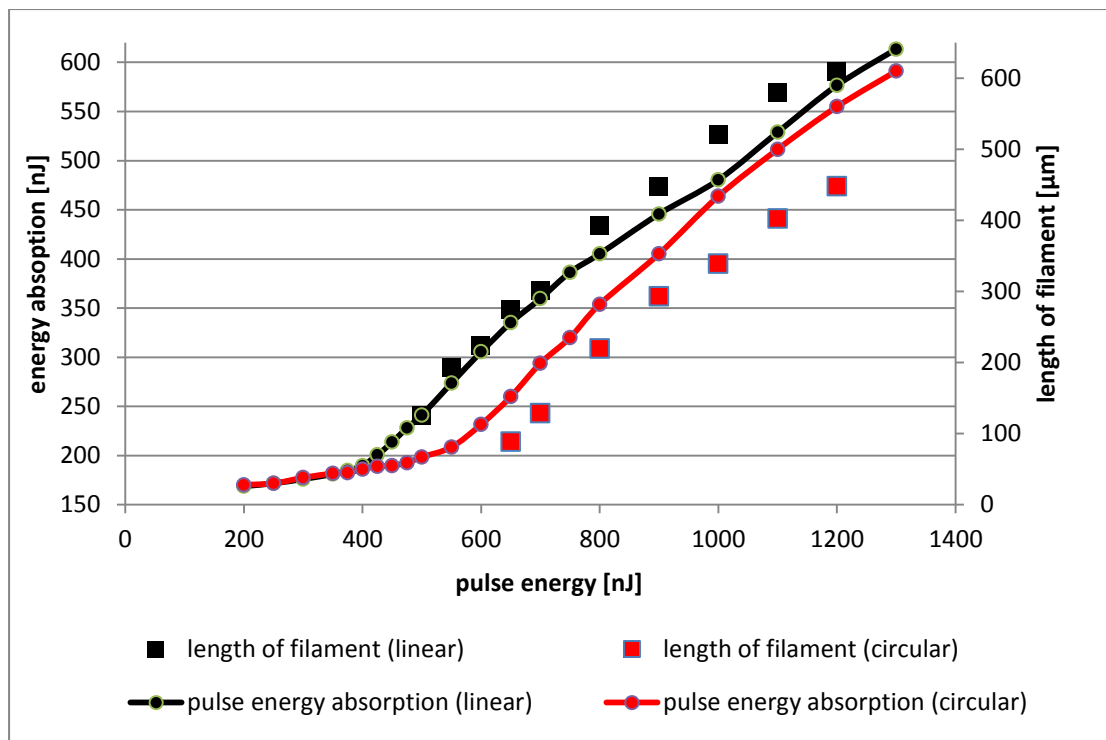


Fig.4.6-2 Comparison of filament length and pulse energy absorption at linear $|V\rangle$ and circular $|R\rangle$ polarisation in PMMA at 775nm

4.7 Polarisation dependent critical power for filamentation in fused silica at 387nm

With pulse energies from $0.5\mu\text{J}$ - $9\mu\text{J}$, at 387nm and $\text{NA}=0.4$, a series of filaments were produced in fused silica (see Fig. 4.7-1). The substrate scan speed was 1mm/sec. Ahead of the filaments, a funnel shaped structure was formed due to the SF, evident from these optical images. As expected, higher pulse energy tends to induce the SF closer to the laser source. With low pulse energy $E < 0.7\mu\text{J}$, no modification was observed. Due to the low optical contrast of the filaments near threshold, it is difficult to estimate the exact energy threshold.

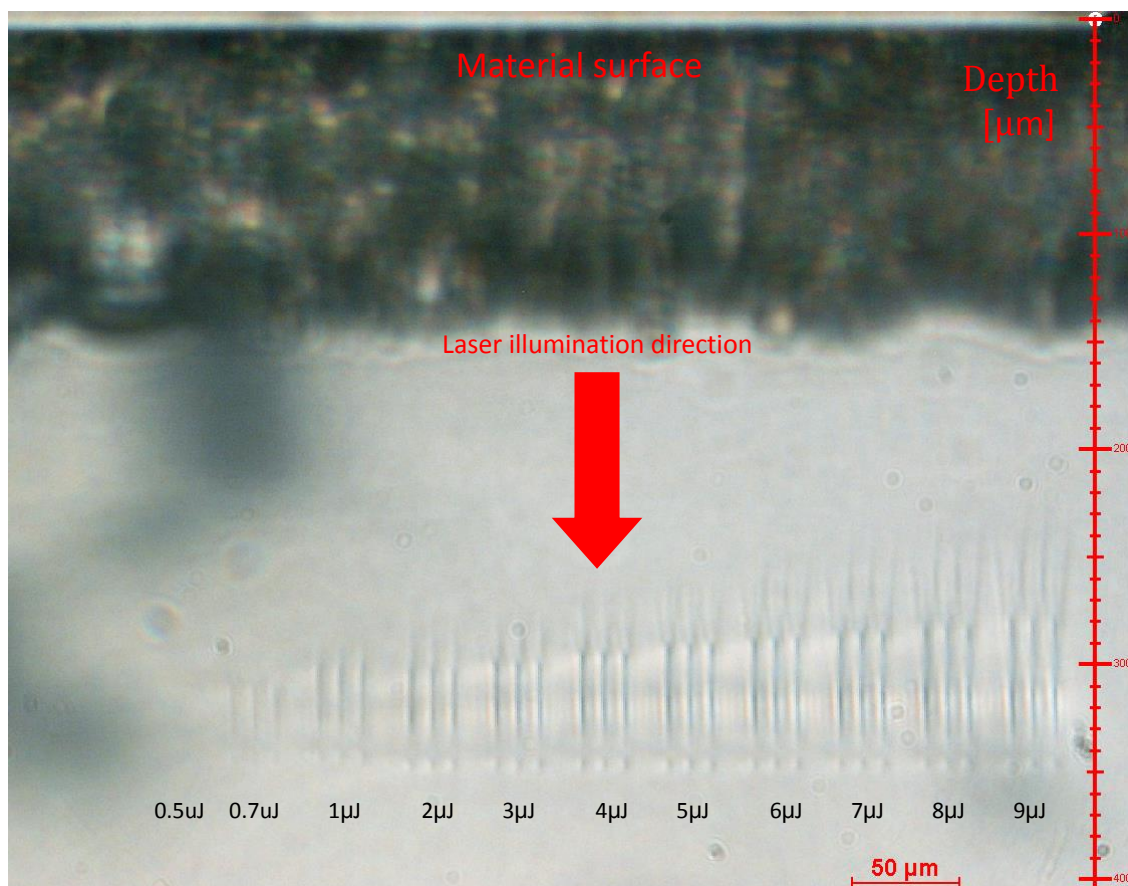


Fig.4.7-1 cross-section of filaments induced by femtosecond laser in fused silica with pulse energy from 0.5 μJ, 0.7 μJ and 1-9 μJ (from left to right) with linear polarisation

4.8 Effects of polarisation on transmitted pulse energy through fused silica at 387nm

As with PMMA, the observed energy loss with incident pulse energy was measured (Fig. 4.8-1) in fused silica with 387nm. The critical energy is ~450nJ for linear polarisation and ~680nJ for circular polarisation and hence a ratio of $P_{C}^{circ}/P_{C}^{Lin} \sim 1.4$, consistent with measurements in PMMA and close to 1.5, expected for all homogeneous dielectrics. Due to the high damage threshold inside fused silica, the laser beam did not result in breakdown of the material,

even at high pulse energy up to 1000nJ.

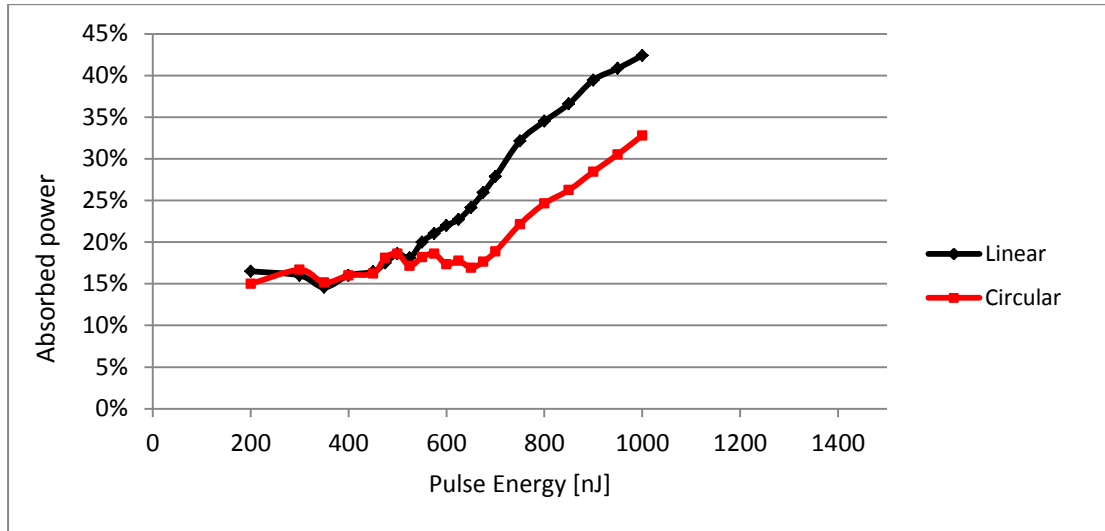


Fig. 4.8-1 absorbed power of focused NIR femtosecond laser (387nm) by fused silica with various pulse energy and with polarisations (|V> and |R>)

4.9 Discussion

We first consider theoretical aspects of filamentation in PMMA with 387nm, fs pulses. As filamentation is the result of the dynamic balance of SF, due to the non-linear refractive index component and plasma defocusing. The n_2^{387} can be estimated by a simple model. From the observed filament widths, self-guiding was limited to a diameter $\varphi = 4.0\mu\text{m}$ (approximate value limited by the resolution of the microscope, see fig.4.2-2(b)) during filamentation. This can be compared to a waveguide whose core has $RI' = n_0 + \delta n$ while outside, the $RI = n_0$. The critical angle for traversing rays in a waveguide is given by $\theta_c = \left(\frac{2\delta n}{n_0}\right)^{1/2}$ while the angle of diffraction of a Gaussian beam of diameter is given by $\theta_{\text{dif}} = 0.61\lambda/n_0\varphi$ so that guiding will occur if all rays experience total

internal reflection, that is when $\theta_c = \left(\frac{2\delta n}{n_0}\right)^{0.5} = 0.61\lambda/n_0\varphi$, hence

$$\delta n_{387} = n_2^{387} I = n_0 \frac{(0.61\lambda_0)^2}{2(n_0\varphi)^2} \quad \text{Eq. 4-2}$$

With $I = 1.22 \times 10^{13} \text{Wcm}^{-2}$, $\lambda_0 = 3.87 \times 10^{-5} \text{cm}$, $\varphi = 4.0 \times 10^{-4} \text{cm}$ and $n_0 = 1.49$, we obtain a value $n_2^{387} = 9.85 \times 10^{-17} \text{cm}^2 \text{W}^{-1}$, a value in reasonable agreement with D'Amore [102] ($1.37 \times 10^{-16} \text{cm}^2 \text{W}^{-1}$) and lower by a factor of 0.7. The proximity of these values supports the linear scaling of $\chi^{(3)}$ to shorter wavelengths. The RI modulation during self-guiding in PMMA, $\delta n = n_2^{387} I \sim 1.67 \times 10^{-3}$, a level consistent with a strongly guiding structure.

The plasma defocusing, causing a negative RI change, can be estimated from the real part $R_e(\Delta n)$ of the Drude equation for the RI change due to the plasma [142],

$$\Delta n = \left[\frac{e^2}{2n_0 \varepsilon_0 \omega^2 m_e} \right] \left[\frac{\rho_e \omega^2 \tau_c^2}{1 + \omega^2 \tau_c^2} \right] \quad \text{Eq. 4-3}$$

where e and m_e are the electron's charge and mass, ε_0 is the permittivity of free space, 1.49 is the linear refractive index, ρ_e is the electron density, $\omega(387\text{nm})$ is the laser frequency ($3.87 \times 10^{15} \text{rads}^{-1}$) and τ_c is the electron collision time. If τ_c is of the order of 1fs or greater, ($\tau_c = 0.4 \text{fs}$ in fused silica) the ratio $\frac{\omega^2 \tau_c^2}{1 + \omega^2 \tau_c^2} > 0.96$ and tends closer to unity as τ_c increases. By equating

the modulus of these two contributions, we get

$$\Delta n = n_2^{387} I = \left[\frac{e^2}{2n_0 \varepsilon_0 \omega^2 m_e} \right] \left[\frac{\rho_e \omega^2 \tau_c^2}{1 + \omega^2 \tau_c^2} \right] \quad \text{Eq. 4-4}$$

Hence we obtain, as $n_2 I = 1.67 \times 10^{-3}$, an estimate of the electron density in a filament, with the help of Eq. 4-4

$$\rho_e = \frac{2n_0 \varepsilon_0 \omega^2 m_e (n_2 I)}{e^2} = 2.22 \times 10^{22} \times (n_2 I) = 4.3 \times 10^{19} \text{cm}^{-3}$$

This value is of the correct order required to produce permanent modification [41]

and well below the critical plasma density $\rho_e^{crit} \sim 10^{21} \text{cm}^{-3}$ which would result in complete optical breakdown. As the scanning speed is 1mm/s (1 $\mu\text{m}/\text{ms}$) during inscription, the material is exposed to only ~ 4 overlapped pulses during inscription of 4 μm wide structures.

The grating efficiencies depend on the phase angle ϕ where $\phi(|P\rangle) = \pi\Delta n_p L / \lambda \cos\theta_B$ for a grating of thickness L and $|P\rangle$ the state of polarisation. As the inscribed filament cross-sections for linear and circular polarisations are different (Fig. 4.2-2), then allowing for slight variation in Δn_p with depth z , the difference in first order DE's is related to changes in optical path length $OPD = \delta(\Delta n_p L)$ given by,

$$\delta(OPD) = \int [\Delta n^{lin}(z) - \Delta n^{circ}(z)] dz = [\Delta n^{lin} - \Delta n^{circ}] L \quad \text{Eq. 4-5}$$

The observed DE after 1 day for linear (TE) polarisation was 62% while the ratio of diffraction efficiencies $R = \frac{\sin^2(\alpha\Delta n^{lin})}{\sin^2(\alpha\Delta n^{circ})} = 1.21 \pm 0.03$ after ~ 1 day which leads to $(\langle \Delta n^{lin} \rangle / \langle \Delta n^{circ} \rangle)_{max} \sim 1.13 \pm 0.03$ when averaged throughout a 4mm grating structure (Section 4.2), a modest though significant variation.

As 2-photon absorption (also related to third order susceptibility $\chi^{(3)}$) initiates the non-linear ionisation process in PMMA at 387nm, there may be a polarisation dependent effect on the 2-photon absorption cross section ratios in PMMA which initiates plasma formation.

Effects of polarisation in multi-photon ionisation, (MPI), were first observed in 1971 during the 3-photon ionisation of atomic Cesium with a Ruby laser where

experimentally, the ratio of cross sections was found to be $\left(\frac{\sigma_2^{circ}}{\sigma_2^{lin}}\right) = 2.15 \pm 0.4$ [113]. Following this, experiments on 2-photon ionisation of Cesium yielded the ratio $\left(\frac{\sigma_2^{circ}}{\sigma_2^{lin}}\right) = 1.28 \pm 0.2$ [145]. These experiments inspired theoretical work on MPI [146, 147] which predicted the dominance of circular polarisation in low order MPI, $N \leq 3$ with upper limits $\left(\frac{\sigma_2^{circ}}{\sigma_2^{lin}}\right) = \frac{3}{2}$ and $\left(\frac{\sigma_2^{circ}}{\sigma_2^{lin}}\right) = \frac{5}{2}$ so that theory and experiments were in reasonable agreement. The general arguments, related to angular momentum conservation during MPI were expected to apply also in solids, confirmed with 4-photon conductivity experiments in quartz yielding $\left(\frac{\sigma_2^{circ}}{\sigma_2^{lin}}\right) = 2.05 \pm 0.9$ [148]. Reiss [147] pointed out, however, that a significant reversal of this behaviour was expected for $N=4$ and confirmed in high $N > 4$, 6-photon Resonance Enhanced MPI (REMPI, 3+3), in the nitric oxide (NO) molecule yielding $\left(\frac{\sigma_2^{circ}}{\sigma_2^{lin}}\right) \sim 2.9$ [149]. In addition, single pulse, (50fs, 800nm) 6-photon ionisation in fused silica at peak intensities $I \sim 10 - 20 \text{ TW cm}^{-2}$ yielded the ratio of absorption cross sections $\left(\frac{\sigma_2^{circ}}{\sigma_2^{lin}}\right) \sim 3.7$ [150]. However, the RI contrast during waveguide inscription in fused silica (120fs, 1kHz, 800nm, 0.46NA) was both polarisation and intensity dependent. [151].

The plasma densities reached in filaments with linear and circular polarisation could be expected to vary by a factor of 3/2 leading to $(\langle \Delta n^{lin} \rangle / \langle \Delta n^{circ} \rangle)_{theory} \sim 1.5$. assuming that $\Delta n \propto \rho_e$. However, the ratio is clearly much lower, $(\langle \Delta n^{lin} \rangle / \langle \Delta n^{circ} \rangle) \sim 1.13$. However, if the ratio of two-photon ionisation cross sections in PMMA was similar that observed in atomic Cesium, that is,

favouring circular polarisation, with $(\frac{\sigma_2^{circ}}{\sigma_2^{lin}}) \sim 1.28$ [145] then circular polarisation could enhance 2-photon ionisation over linear polarisation, increasing the initial seed electron density available for impact ionisation. This effect could reduce the differential in final plasma densities, yielding $(\langle \Delta n^{lin} \rangle / \langle \Delta n^{circ} \rangle) \sim \frac{1.5}{1.28} \sim 1.17$, closer to the ratio $(\langle \Delta n^{lin} \rangle / \langle \Delta n^{circ} \rangle)_{max} \sim 1.13 \pm 0.03$ estimated from the measured first order diffraction efficiencies. This may be a fortuitous result and would require additional confirmation by high NA, polarisation dependent experiments (defeating filamentation) of 2-photon absorption coefficients, well beyond the scope of this thesis.

4.10 Summary

In this chapter, the effect of polarisation in femtosecond laser internal processing in PMMA is demonstrated. VBGs were produced using parallel NUV femtosecond laser beams at 387nm with 4 polarisation states: linear $|V\rangle$, linear $|H\rangle$, right circular $|R\rangle$ and left circular $|L\rangle$. The first order diffraction efficiencies of these gratings have significant polarisation dependent effect, due to polarisation dependent SF leading to the polarisation dependent filamentation. In PMMA, at 387nm with linear $|V\rangle$ and circular $|R\rangle$ or $|L\rangle$ polarisation, the critical pulse energy for filamentation has been convincingly measured to be higher for circular polarisation and the ratio $P_c^{LIN}/P_c^{circ} \sim 1.3-1.5$. This agrees with theoretical expectations in pure dielectrics [143]. In addition, at the fundamental wavelength of 775nm, vortex azimuthal $|Az\rangle$ and radial polarisation $|Ra\rangle$ showed highest critical power for SF requiring 1000nJ in PMMA almost twice

that required for circular polarisation. Radial and azimuthal states had nearly equal thresholds and this high threshold may well be due to slightly lower beam quality when generating these unusual polarisation states carrying orbital angular momentum.

Chapter 5

Optimisation of energy uniformity of multiple laser beams

5.1 Introduction

A real-time laser beam profile feedback and optimisation system was developed to optimise the laser pulse energy of multi-pulse beams generated by the SLM. This system collects the complete beam profile image with the camera and analyses the energy distribution. After comparing the measured pulse energy of multi-beam pattern with the desired pattern, a new CGH is calculated to improve the pulse energy uniformity of the multiple beams. The optimisation technique was applied to improve the uniformity of both NIR and NUV parallel beams for internal and surface processing. In addition, the real-time feedback system collected data and used to optimise dynamic beam patterns.

5.2 Equipment

The Clark-MXR CPA 2010 laser and SLM Hamamatsu X10468-02 phase only spatial light modulator were used in this experiment. When combined with a CCD camera, a real-time feedback system was therefore developed.

5.2.1 CCD Camera

A Spiricon SP620U USB silicon CCD camera was used to capture the beam profile for a real time feedback system, which was programmed to optimize the energy uniformity of multi-beam pulses. Table 5.2-1 shows the specification of this camera.

Table 5.2-1 Specifications of the CCD camera

Item	Specification
Model	SP620U
Application	1/1.8" format, high resolution, wide dynamic range, pulsed lasers, CW YAG, adjustable ROI
Spectral Response	190 - 1100nm ⁽²⁾
Active Area	7.1mm W x 5.4mm H
Pixel spacing	4.40µm x 4.40µm
Number of effective pixels	1600 x 1200
Minimum system dynamic range	62 dB
Linearity with Power	±1%
Accuracy of beam width	
Frame rates: In 12 bit mode	7.5 fps at full resolution 28 fps at 640x480 44 fps at 320x240
Saturation intensity ⁽¹⁾	2.2µW/cm ²
Lowest measurable signal ⁽¹⁾	2.5nW/cm ²
Damage threshold	led for <100ns pulse width ⁽³⁾
Dimensions and CCD recess	96mm x 76mm x 23mm CCD recess: 4.5mm below surface

“Beamgage” is the commercial software developed to control the camera and measure the beam properties. This software is much more advanced than previous versions and provides more functions. As shown in Fig. 5.2-1 the beam profile can be demonstrated both in 2D and in 3D images. Most importantly, the camera can be partitioned electronically into many different sections so that the integrated signals (energy) in these sections can be compared.

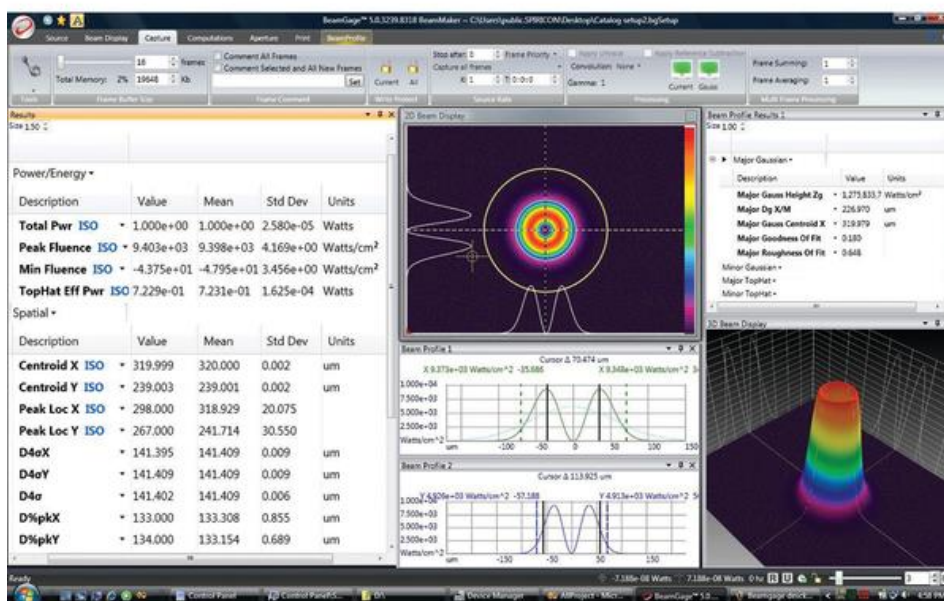


Fig. 5.2-1 Interface of the Beamgage software

5.2.2 Modification of LabVIEW software

The basic Glasgow software introduced in Section 3.2 was modified significantly to generate new CGHs for parallel processing with the feedback system collecting data from the camera to optimize the CGHs. Fig.5.2-2, shows the new the software interface, where an arbitrary pattern with random or regular array design comprising multiple spots can be created manually by typing the x-y position of each spot or generated automatically by setting the array size, spots separations, and the position of the top left corner in the x and y axes. The red spots are the equivalent of the green circles in the original program (Fig. 3.2-2). With the same GS algorithm, the improved 8-bit greyscale CGH was generated, and the CGH was addressed to the SLM to diffract the energetic single beam to a multiple beam pattern. The CGH was optimized according to the feedback beam

profile under each iteration.

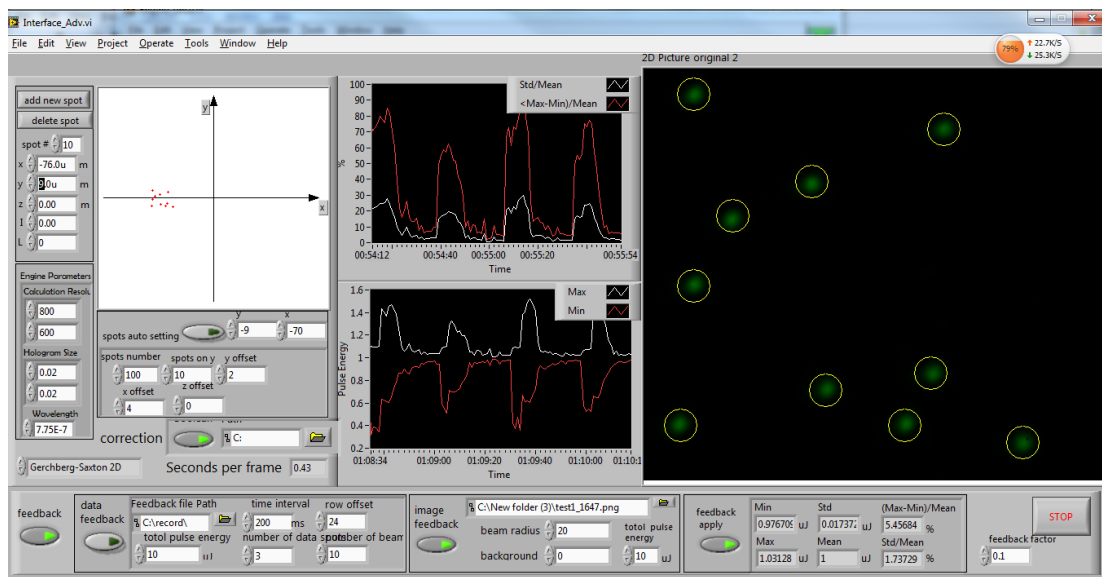


Fig. 5.2-2 the reprogrammed LabView interface with multiple spots pattern and feedback. The left white window is the designed beam pattern. The right black window shows the detailed beam pattern while the two middle charts illustrate the uniformity of the measured pulse energies (see Section 5.4.5).

5.3 Experimental setup

Based on the experimental setup introduced in Section 3.4, Fig. 5.3-1 demonstrates the new processing setup with real-time feedback, inserted between M4 and objective. Prior to the objective, a thin film pellicle beam splitter was used to pick off the laser beam holding the re-imaged hologram with 8% reflectivity. This feedback beam was focused by a long focal length lens L3 ($f=750\text{mm}$) to about 10mm in front of the CCD camera to avoid sensor damage.

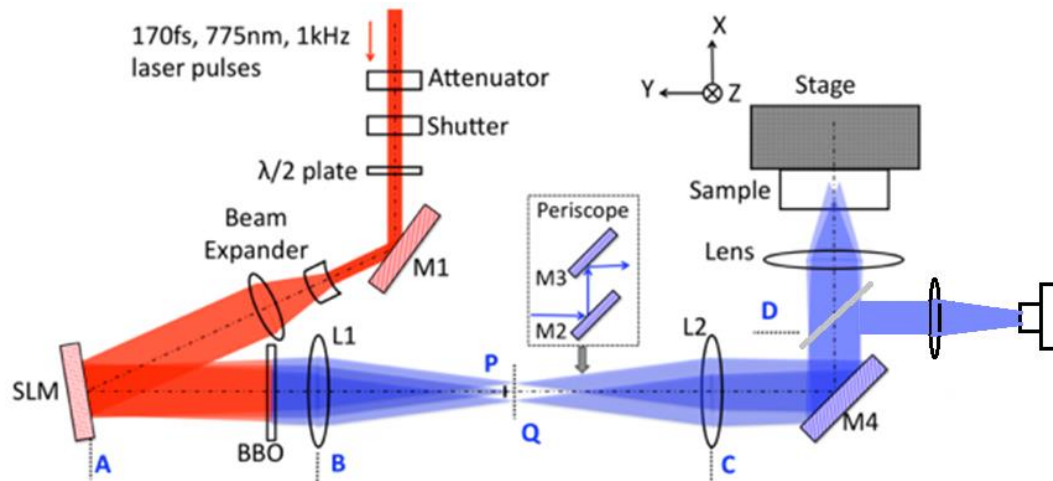


Fig. 5.3-1 Schematic of the experimental setup for NUV parallel processing with camera based feedback and optimization system

The setup for processing with NUV(387nm) can be switched to NIR(775nm) by removing the BBO crystal, replacing mirrors 3-5 with 775nm high reflectors and re-adjusting the positions of L1 and L2 in the 4f system.

5.4 Introduction to the software

The flowchart of the software is demonstrated in Fig.5.4-1. It is composed of three main modules: hologram setting module, hologram calculation module and feedback module.

The parameters of a desired beam pattern can be described by the set \mathbb{S} , expressed as follows:

$$\mathbb{S} = [S_1(x_1, y_1, \varepsilon_1), S_2(x_2, y_2, \varepsilon_2), S_3(x_3, y_3, \varepsilon_3) \cdots \cdots S_n(x_n, y_n, \varepsilon_n)] \quad \text{Eq. 5-1}$$

where x_n and y_n are the position of the n-th beam in the xy-coordinate system and ε_n is the pulse energy of the n-th beam. The setting of these parameters of \mathbb{S} is entered in the software interface. It is the manually input value.

The objective of the module is to generate beams with the desired parameters of \mathbb{S} . The captured beam generated can be expressed as:

$$\mathbb{Q} = [Q_1(X_1, Y_1, E_1), Q_2(X_2, Y_2, E_2), Q_3(X_3, Y_3, E_3) \cdots \cdots Q_n(X_n, Y_n, E_n)] \quad \text{Eq. 5-2}$$

where \mathbb{Q} is the group of beams on the image captured by the camera, Q_n is the n-th beam in this group. X_n and Y_n are the measured position of the n-th beam corresponding to the camera captured image and E_n is the measured pulse energy.

Due to the approximation of the algorithm, \mathbb{Q} is not identical to \mathbb{S} , and the difference between which deteriorates the quality of material processing. The difference between \mathbb{S} and \mathbb{Q} then generates adjusted settings via feedback, which can be expressed by the set \mathbb{P} ,

$$\mathbb{P} = [P_1(x_1, y_1, e_1), P_2(x_2, y_2, e_2), P_3(x_3, y_3, e_3) \cdots \cdots P_n(x_n, y_n, e_n)] \quad \text{Eq. 5-3}$$

where P_n is the n-th beam in this group. The optimisation of the pulse energy uniformity is all based on the calculation with group \mathbb{S} , \mathbb{P} and \mathbb{Q} .

5.4.2 Calculation of holograms

The hologram calculation module, which includes 5 algorithms, were all developed by Glasgow University [110,114] for applications in optical tweezers. These are termed Lens and Gratings, Random Phase, Gerchberg Saxton 2D, Gerchberg Saxton 3D and Roberto Gerchberg Saxton. The Gerchberg Saxton 2D algorithm (which is itself an iterative algorithm) was used to achieve a fast calculation speed while also generating reasonable initial uniformity. The feedback pulse energy uniformity is mainly returned to this module for optimisation.

5.4.3 Methods of feedback

The feedback module collects the properties of the focused diffracted beams including the position and the pulse energy on the camera. It provides two feedback mechanisms all connected to the Beamgage camera control software either by image feedback or data feedback.

For the data feedback algorithm, the module receives the processed beam properties expressed as group Q from Beamgage. The multi-beam image was collected by the camera and displayed in Beamgage as shown in Fig5.2-2. For Beamgage to calculate the energy, each beam in the image was identified and selected by manually defining partitions on the camera, each covering one beam. The pulse energy of each beam was calculated by the Beamgage software and recorded into a spreadsheet file. This mechanism has a high recording speed at

about 10 data points per second but with a partition limitation of 12 due to the software setting.

For the image feedback, the Labview program reads and analyses the image files, recorded by Beamgage at 4-5 frames per second. Since Beamgage measure the exposure (energy) on every pixel, the pulse energy in each beam can be calculated by integrating the exposure in each partition in LabVIEW software.

5.4.4 Algorithm of optimisation

For the first iteration, after the generation of the first hologram corresponding to the original hologram setting

$$\mathbb{S} = [S_1(x_1, y_1, \epsilon_1), S_2(x_2, y_2, \epsilon_2), S_3(x_3, y_3, \epsilon_3) \cdots \cdots S_n(x_n, y_n, \epsilon_n)] \quad \text{Eq. 5-4}$$

$$\mathbb{P}_1 = \mathbb{S}$$

and the return of the first feedback beam properties:

$$\mathbb{Q}_1 = [Q_{11}(X_1, Y_1, E_{11}), Q_{21}(X_2, Y_2, E_{21}), Q_{31}(X_3, Y_3, E_{31}) \cdots \cdots Q_{n1}(X_n, Y_n, E_{n1})] \quad \text{Eq. 5-5}$$

The energy difference group \mathbb{E}_1 is then calculated from the pulse energy in group \mathbb{Q} and pulse energy in the original beam setting \mathbb{S} , giving

$$\mathbb{E}_1 = (\Delta e_{11}, \Delta e_{21}, \Delta e_{31} \cdots \cdots \Delta e_{n1}) \quad \text{Eq. 5-6}$$

where $\Delta e_{n1} = E_{n1} - \epsilon_n$.

A positive Δe_{n1} indicates that the measured pulse energy is higher than setting value and vice versa.

Furthermore, the energy difference is divided by an adjustment factor m (discussed in section 5.4.6), so that the modified energy difference can be written

as:

$$\mathbb{E}_1' = \frac{\mathbb{E}_1}{m_1} = \left(\frac{\Delta e_{11}}{m_1}, \frac{\Delta e_{21}}{m_1}, \frac{\Delta e_{31}}{m_1} \dots \dots \frac{\Delta e_{n1}}{m_1} \right) \quad \text{Eq.5-7}$$

For the second iteration, the energy difference group \mathbb{E}_1' is then added to group \mathbb{P}_1 giving the adjusted pulse energy setting \mathbb{P}_2 after the first iteration :

$$\mathbb{P}_2 = [P_{12}(x_1, y_1, e_{12}), P_{22}(x_2, y_2, e_{22}), P_{32}(x_3, y_3, e_{32}) \dots \dots P_{n2}(x_n, y_n, e_{n2})] \quad \text{Eq. 5-8}$$

where $e_{n2} = e_{n1} + \frac{\Delta e_{n1}}{m}$. A new hologram is calculated with the adjusted beam setting \mathbb{P}_2 which is then sent to SLM to generate a new set of diffracted beams. Measured by the camera, the new beam group \mathbb{Q}_2 is returned to the system:

$$\mathbb{Q}_2 = [Q_{12}(X_1, Y_1, E_{12}), Q_{22}(X_2, Y_2, E_{22}), Q_{32}(X_3, Y_3, E_{32}) \dots \dots Q_{n2}(X_n, Y_n, E_{n2})] \quad \text{Eq. 5-9}$$

The \mathbb{E}_2 for the second iteration is calculated from \mathbb{P}_2 and \mathbb{Q}_2 :

$$\mathbb{E}_2 = (\Delta e_{12}, \Delta e_{22}, \Delta e_{32} \dots \dots \Delta e_{n2})$$

where $\Delta e_{n2} = E_{n2} - \mathcal{E}_n$

Thus,

$$\mathbb{E}_2' = \left(\frac{\Delta e_{12}}{m_2}, \frac{\Delta e_{22}}{m_2}, \frac{\Delta e_{32}}{m_2} \dots \dots \frac{\Delta e_{n2}}{m_2} \right) \quad \text{Eq. 5-10}$$

Then, the \mathbb{P}_3 for the third iteration is given by:

$$\mathbb{P}_3 = [P_{13}(x_1, y_1, e_{13}), P_{23}(x_2, y_2, e_{23}), P_{33}(x_3, y_3, e_{33}) \dots \dots P_{n3}(x_n, y_n, e_{n3})] \quad \text{Eq. 5-11}$$

where $e_{n3} = e_{n2} + \frac{\Delta e_{n2}}{m_2}$

Therefore, in the k-th iteration, we get:

1) The group of setting beams behind the interface:

$$\mathbb{P}_k = [P_{1k}(x_1, y_1, e_{1k}), P_{2k}(x_2, y_2, e_{2k}), P_{3k}(x_3, y_3, e_{3k}) \cdots \cdots P_{nk}(x_n, y_n, e_{nk})] \quad \text{Eq. 5-12}$$

2) The group of real beams:

$$\mathbb{Q}_k = [Q_{1k}(X_1, Y_1, E_{1k}), Q_{2k}(X_2, Y_2, E_{2k}), Q_{3k}(X_3, Y_3, E_{3k}) \cdots \cdots Q_{nk}(X_n, Y_n, E_{nk})] \quad \text{Eq. 5-13}$$

and each pulse energy is theoretically equal or very close to the original setting, achieving a much improved uniformity.

3) The energy difference group:

$$\mathbb{E}'_k = \left(\frac{\Delta e_{1k}}{m_k}, \frac{\Delta e_{2k}}{m_k}, \frac{\Delta e_{3k}}{m_k} \dots \dots \frac{\Delta e_{nk}}{m_k} \right) \quad \text{Eq. 5-14}$$

where $\Delta e_{nk} = E_{nk} - e_{nk}$

5.4.5 Critical value

The pulse energy uniformity of a group of captured beams

$$\mathbb{Q} = [Q_1(X_1, Y_1, E_1), Q_2(X_2, Y_2, E_2), Q_3(X_3, Y_3, E_3) \cdots \cdots Q_n(X_n, Y_n, E_n)] \quad \text{Eq. 5-15}$$

is measured by two indices of dispersion:

1) Standard deviation over mean (SDM):

The standard deviation (σ) shows how much variation or dispersion from the average exists. The Standard deviation over mean is therefore,

$$\eta_{sdm} = \frac{\sigma}{\bar{E}} = \sqrt{\frac{\sum_{i=1}^n (E_i - \bar{E})^2}{n}} / \bar{E} \times 100\% \quad \text{Eq. 5-16}$$

where \bar{E} is the average pulse energy of the n beams.

2) Range to Mean Ratio (rmr):

For a large number of beams, when most beams have relatively similar pulse energy but still one or two with extreme low or high energy, the η_{sdm} can still be reasonably low. However, for parallel processing, occurrence of a small number of beams with extreme pulse energy is enough to degrade the processing quality significantly, particularly for the fabrication of integrated optics with periodic structures such as VBGs. Therefore, another critical value is used for detecting these outliers and given by,

$$\eta_{rmr} = \frac{E_{max} - E_{min}}{\bar{E}} \quad \text{Eq. 5-17}$$

where E_{max} and E_{min} are the maximum and minimum pulse energy in this beam group, and \bar{E} is the average pulse energy. A low η_{rmr} indicates a high beam quality.

5.4.6 Factor m

In the calculation, the factor m in Eq. 5-7, Eq. 5-10 and Eq. 5-14 is a key value determining the percentage of the energy difference between settings and measurements to be added to \mathbb{P} . In the first few iterations, m is usually set equal to 2. In other words, about 50% of the difference can be compensated in \mathbb{Q} after each iteration. However, the energy weight change \mathbb{E}' to group \mathbb{P} will affect the calculation with the GS algorithm. As a result, when m =2, the real effect on \mathbb{Q} is not exactly $0.5\Delta e_{nk}$ but $0.5\Delta e_{nk} \pm E(m)$, where $E(m)$ is a function of m. Experimentally, $E(m)$ was found to generally increase with m related to the calculation algorithm for CGHs. As a results, after 3-4 iterations, the uniformity

could not be optimised further due to high $E(m)$. Therefore, in the software, when η_{sdm} was lower than 10%, the factor m was increased to 10 to lower the $E(m)$ and further improve the pulse energy uniformity.

5.5 Optimisation of 10 × 10 beam array

Fig 5.5-1 illustrates the generation and optimisation of an array of 10 X10 NIR laser beams in Labview environment with $E_T \sim 100\mu\text{J}$ incident total pulse energy. The 2D beam array was designed with separation of 30 μm and 25 μm on x and y axes and $\sim 1\mu\text{J}/\text{pulse}/\text{beam}$. NIR Multi-beam internal structuring fused silica before beam optimisation, the minimum pulse energy was about 0.4 μJ while the maximum pulse energy was about 1.6 μJ . The high η_{sdm} up to 30% indicated a poor uniformity. This large deviation in pulse energy degrades the processing quality significantly.

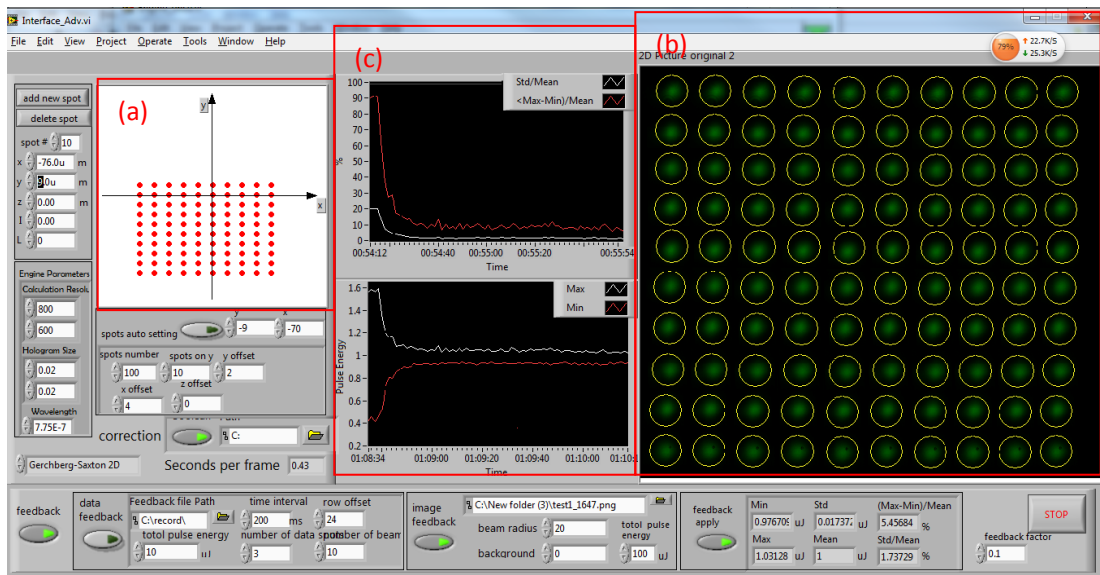


Fig. 5.5-1 The design and optimisation results of 100 NIR beams (a) 10 X10 NIR beam array designed in xy coordinates (b) image of focused beam captured by camera with auto tracked and circled beams. (c) charts showing the pulse energy uniformity with time.

After 18 seconds of optimisation as shown in the middle charts of Fig. 5.5-2, the standard deviation/Mean (η_{sdm}) was reduced from about 20% to about 1.7% and the η_{rnr} was also decreased from about 90% to about 5%. The optimisation result was stable with less than 2% fluctuation.

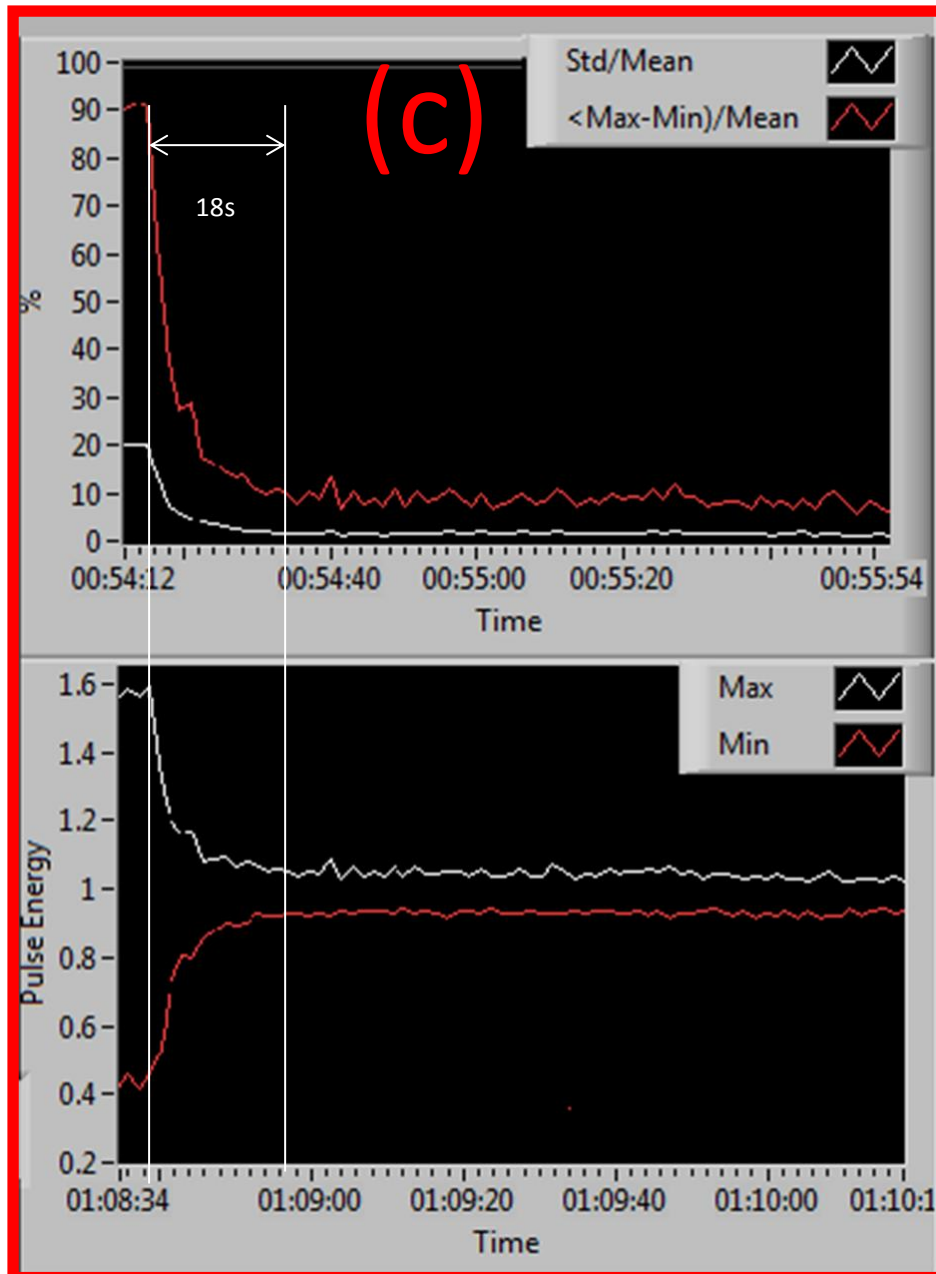


Fig. 5.5-2 Charts showing the pulse energy uniformity with time

(zoom-in of section (c) in Fig. 5.5-1).

Fig. 5.5-3 illustrates the theoretical pulse energy uniformity of 10 X 10 beam array recognised by the system (white curve) and the experimental uniformity measured by the camera (red). In Section 1 of Fig.5.5-3, the system started to calculate the CGH which reach the optimised condition after about 5 iterations.

Correspondingly, the standard deviation over mean (SDM) of the pulse energy measured through the feedback image reached 20% which is not fully optimised. In section 2 (Fig.5.5-3), the uniformity was stable. At the beginning of section 3, the feedback optimisation was switched on. The SDM of the measured pulse energy was reduced to 1% which kept stable in section 4, while the SDM in the system increased to 20% which means the algorithm in the system failed to produce uniform beams although the system considered the uniformity was optimised. With the feedback system, the uniformity was successfully corrected.

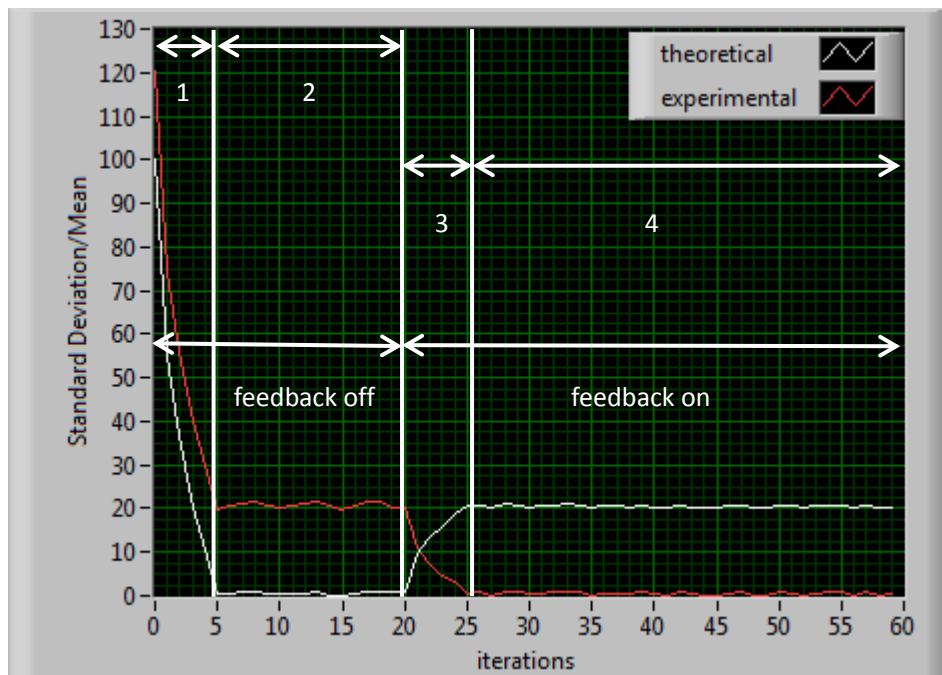


Fig. 5.5-3 the Standard Deviation/Mean of the theoretical uniformity (calculated by the CGHs Calculation module, white) and experimental uniformity (measured by Camera, red) before and after the utilisation of feedback system

5.6 Auto-tracking of multiple beams

This auto-tracking technique can rapidly locate and number each diffracted beam automatically. As shown in Fig.5.6-1(a) a group of 10 beams \mathbb{S} are dragged to random positions.

$$\mathbb{S} = [S_1(x_1, y_1, \varepsilon_1), S_2(x_2, y_2, \varepsilon_2) \cdots \cdots S_{10}(x_{10}, y_{10}, \varepsilon_{10})] \quad \text{Eq. 5-18}$$

$$\mathbb{P}_1 = \mathbb{S}$$

By analysing the feedback image from the camera, the system marks the positions of the beams in circles and numbers all the beams in the image into a detected beam group,

$$\mathbb{Q} = [Q_1(X_1, Y_1, E_1), Q_2(X_2, Y_2, E_2) \cdots \cdots Q_{10}(X_{10}, Y_{10}, E_{10})] \quad \text{Eq. 5-19}$$

For instance, after the k-th iteration, let us assume that one of the beams (n=2) needs to be moved to a new position. Let the new position of S_2 be given by,

$$S'_2(x_2 + \Delta x, y_2 + \Delta y, \varepsilon_2)$$

Thus,

$$\mathbb{S}' = [S_1(x_1, y_1, \varepsilon_1), S'_2(x_2 + \Delta x, y_2 + \Delta y, \varepsilon_2) \cdots \cdots S_{10}(x_{10}, y_{10}, \varepsilon_{10})] \quad \text{Eq. 5-20}$$

After the software loads the image recorded by Beamgage, it is quick for the system to mark and pick up the beam. However, it is not trivial for the system to identify which beam in the original image has moved and to which new position.

To arrange the detected beams with the correct order, an auto-tracking function was achieved with 3 steps as follows:

- 1) Pick up all the beams in the feedback image.
- 2) Analyse the position of each beam.

3) Number the beams by comparing the beam position with settings.

Therefore, the system automatically tracked the beam which has been moved and recorded the new beams in the new image as a new group:

$$\mathbb{Q}_k = [Q_{1k}(X_1, Y_1, E_{1k}), Q_{2k}(X_2 + \Delta X, Y_2 + \Delta Y, E_{2k}), Q_{3k}(X_3, Y_3, E_{3k}) \\ \dots \dots Q_{nk}(X_n, Y_n, E_{nk})] \quad \text{Eq. 5.21}$$

As a result, by using image feedback, the system always returns the \mathbb{Q}_k with the consistent beam orders.

In the k-th iteration, the design of the beam is shown in Fig. 5.6-1(a). At the beginning, the beams were all detected and circled by the software shown in Fig. 5.6-1(b). In the k+1-th iteration, beam 2 was moved from left to the right side (see Fig. 5.6-1(c)). The new hologram was then calculated and addressed to the SLM, the diffracted beams from which were captured by the camera shown in Fig. 5.6-1(b) and (d). The system automatically circled the beam 2 at the new position and feedback \mathbb{Q} with the same order as in the original setting. This real-time auto-tracking function can be applied to track dynamic beam designs.

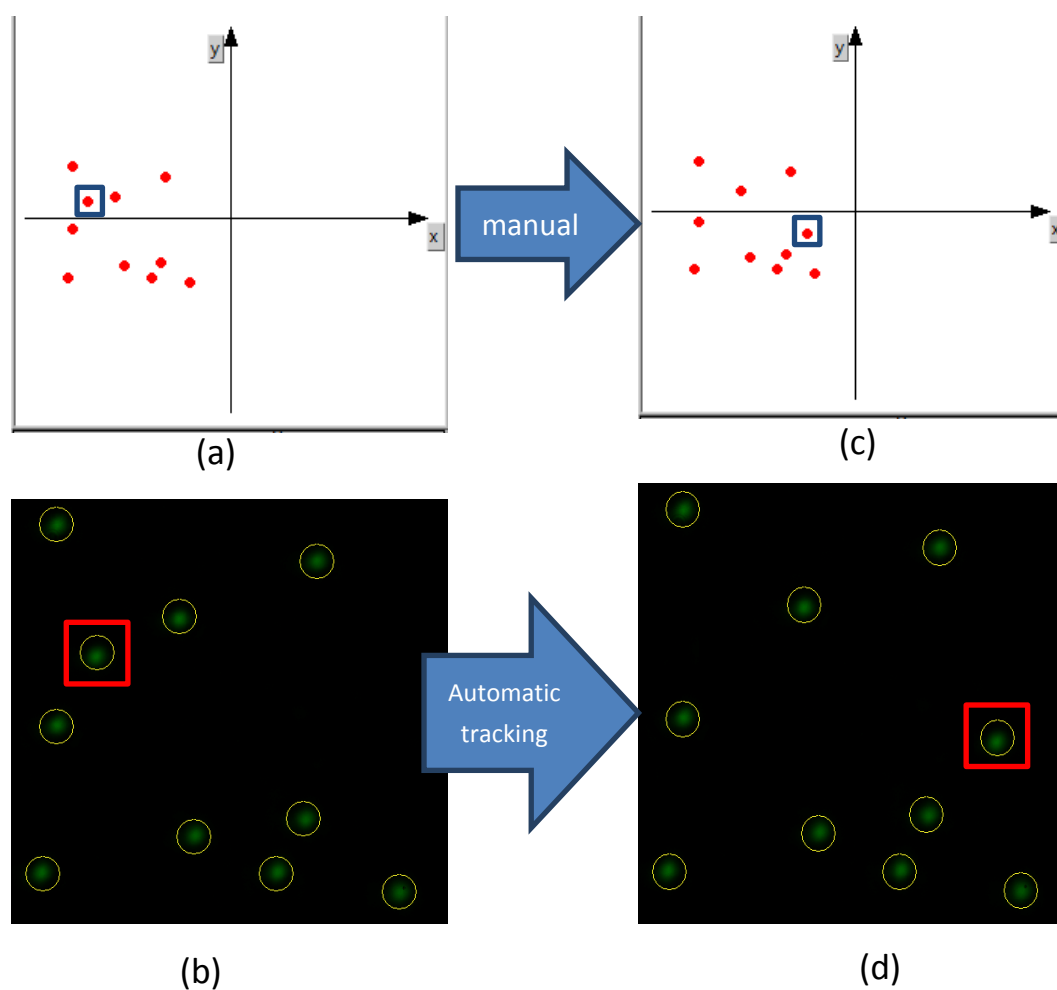


Fig. 5.6-1 Dynamic beam auto-tracking system. The moved beam is inside the square in the images. (a) the original beam pattern designed in interface. (b) image of the beam pattern captured from the camera. (c) beam 2 in the original beam pattern moved to a new position. (d) the beam 2 in the new position was tracked and circled in the new image.

The real-time tracking and optimisation technique was utilised for improving the pulse energy uniformity of 10 infrared beams. The positions of the beams were randomly moved every 5 seconds. Fig. 5.6-2 demonstrates the performance of the real-time optimisation of dynamic beams. The optimisation started to work at $t=6s$, improving the pulse energy uniformity within $6(t=12s)$ seconds with the

η_{sdm} from about 30% to lower than 8% and η_{rmr} from about 85% to lower than 18%. Then, at $t=22s$ η_{sdm} and η_{rmr} were further reduced to 4% and 10% respectively. At $t=26s$ the position of the beams were reset and the hologram was recalculated. As a result, the uniformity of the pulse energy deteriorated at once with the η_{sdm} and η_{rmr} increasing back to about 20% and 60% respectively. Receiving the declined uniformity, the optimisation system started to adjust the energy weight in group \mathbb{P} to narrow the difference between measurement group \mathbb{Q} and the desired setting. Within 2 seconds, the pulse energy uniformity improved again with low η_{sdm} and η_{rmr} . The optimisation improved the uniformity with each change of the beam geometry.

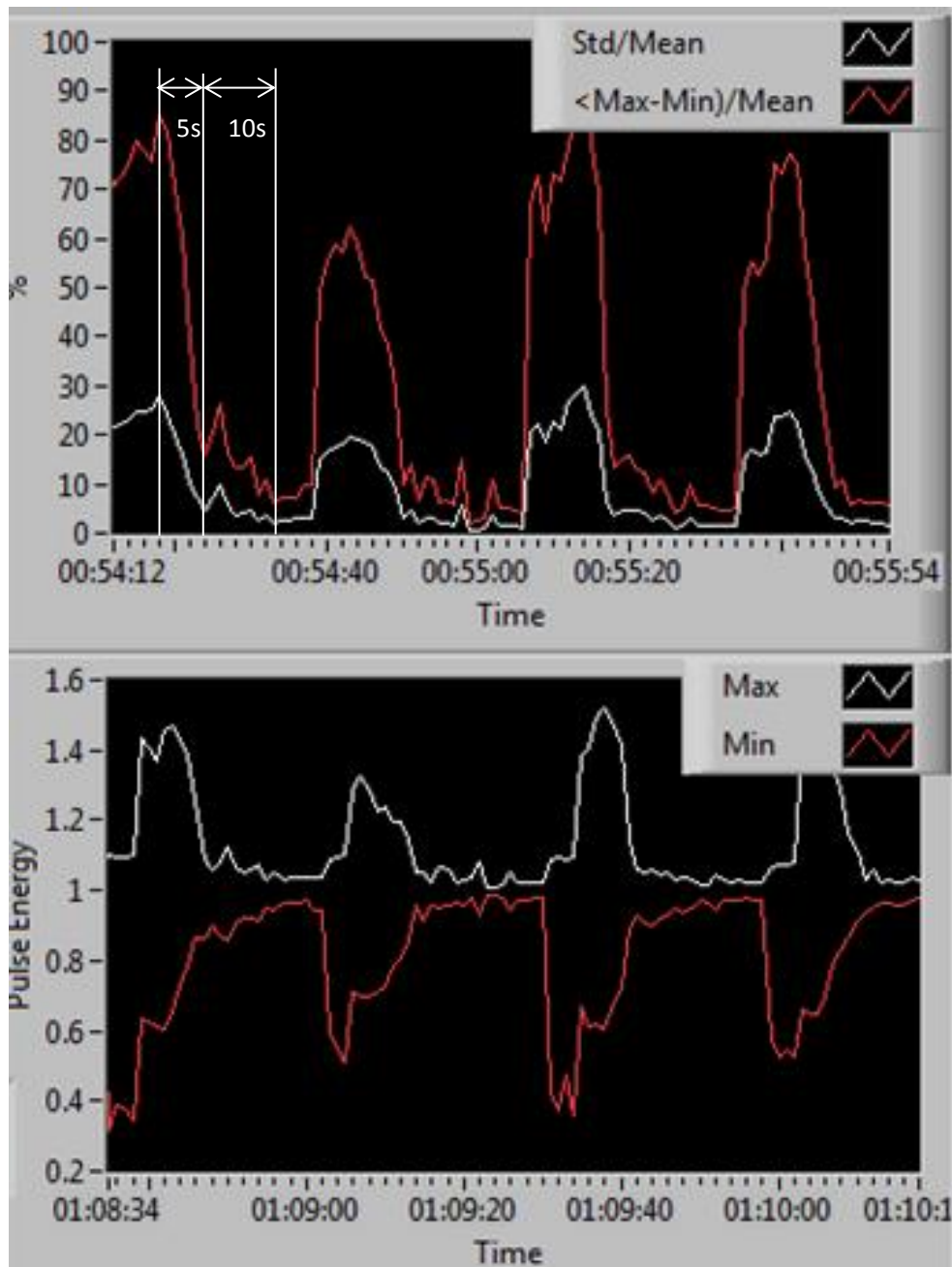


Fig. 5.6-2 optimisation of dynamic beam designs showing response time of 20-30 seconds

5.7 pulse energy optimisation at NUV wavelength for filamentation in PMMA

The optimisation of multiple NUV laser beams is critical for uniform filaments and refractive index modification in laser internal processing. Filaments were created inside PMMA by 10 parallel NUV femtosecond laser beams. The geometric and orientation of the filaments is explained in Fig.5.7-1(a). A comparison of cross-sections of the filaments produced by original array compared to the optimised 10 NUV femtosecond laser beam array is shown in Fig 5.7-1(b). The 10 filaments on the left were processed with 10 parallel NUV beams without CGH feedback optimisation. Before optimisation, (η_{rmr} of 20% and η_{sdm} exceeding 10%) the variation in filament lengths due to pulse energy non-uniformity are very clear, with the longest filament almost twice that of the shortest. As non-linear SF is highly energy sensitive, then higher pulse energy increases the SF effect which creates filaments which originate nearer the laser source. These variations could limit VBG performance through non-uniform inscription.

The 10 filaments on the right of Fig.5.7-1 (b) were generated by optimised 10 parallel NUV beams using feedback. Clearly, the uniformity was dramatically improved as the filaments all start almost at the same depth. The two indices of dispersion η_{rmr} and η_{SDM} in filament lengths were consequently reduced to 0.8% and 0.4% respectively.

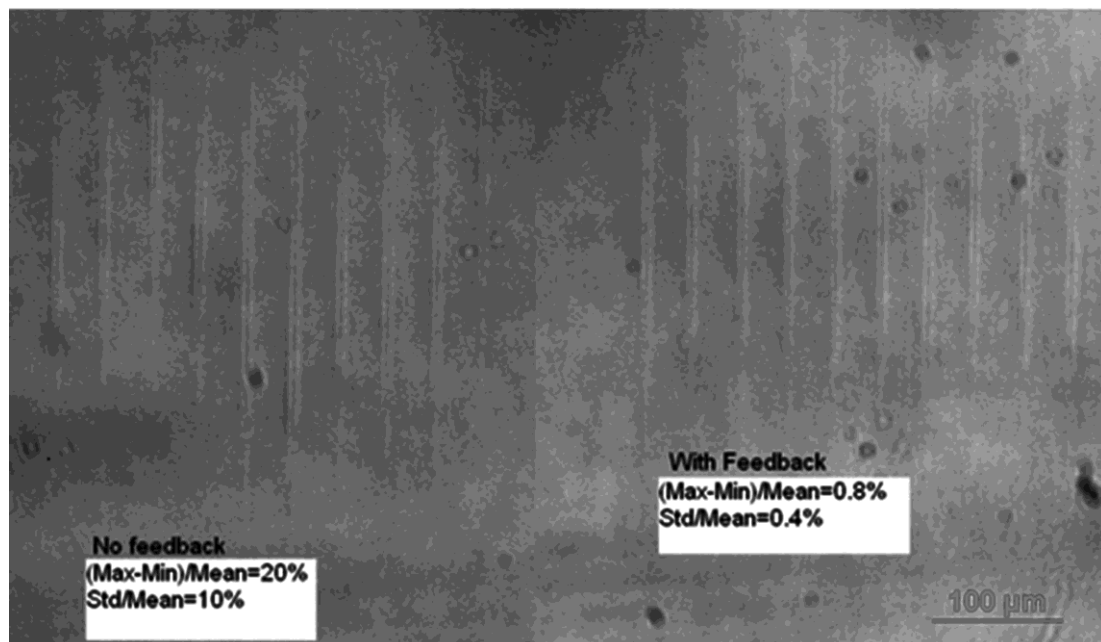
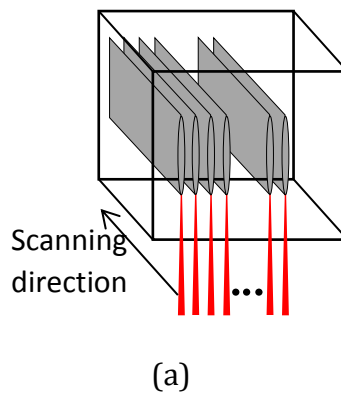


Fig. 5.7-1 (a) geometric and orientation of the filaments (b) the internal micro-machining inside PMMA clearly demonstrates the improvement in uniformity with the 10 parallel spots

However, VBGs with 4mm thickness did not show a major improvement in quality even when the feedback system was employed. One possible reason is due to the 10% overlapping of filaments between layers as shown in Fig. 3.6-1, which reduced the difference in filament lengths. Nevertheless, when thicker VBGs are required, the sensitivity to non-uniformities will be magnified and so

comparison of efficiencies and scatter in devices with $L > 4$ would be instructive.

5.8 Pulse energy optimisation at NIR wavelength for surface ablation

Although the feedback system didn't improve the quality of VBGs, this technique can also be applied in laser surface processing, which will demonstrate obvious difference in processing quality.

By using the real-time feedback and optimisation system, the beam array, as shown in Fig 5.8-3 (b) and (d), achieved outstanding pulse energy uniformity at the η_{sdm} of 1.7% and η_{rmr} of 5.4%, indicating a major uniformity improvement. Fig 5.8-3 (e) and (f) demonstrate the results of surface machining on stainless steel process by the 100 spot beam array with and without optimisation, confirming clearly the advantages of the feedback system.

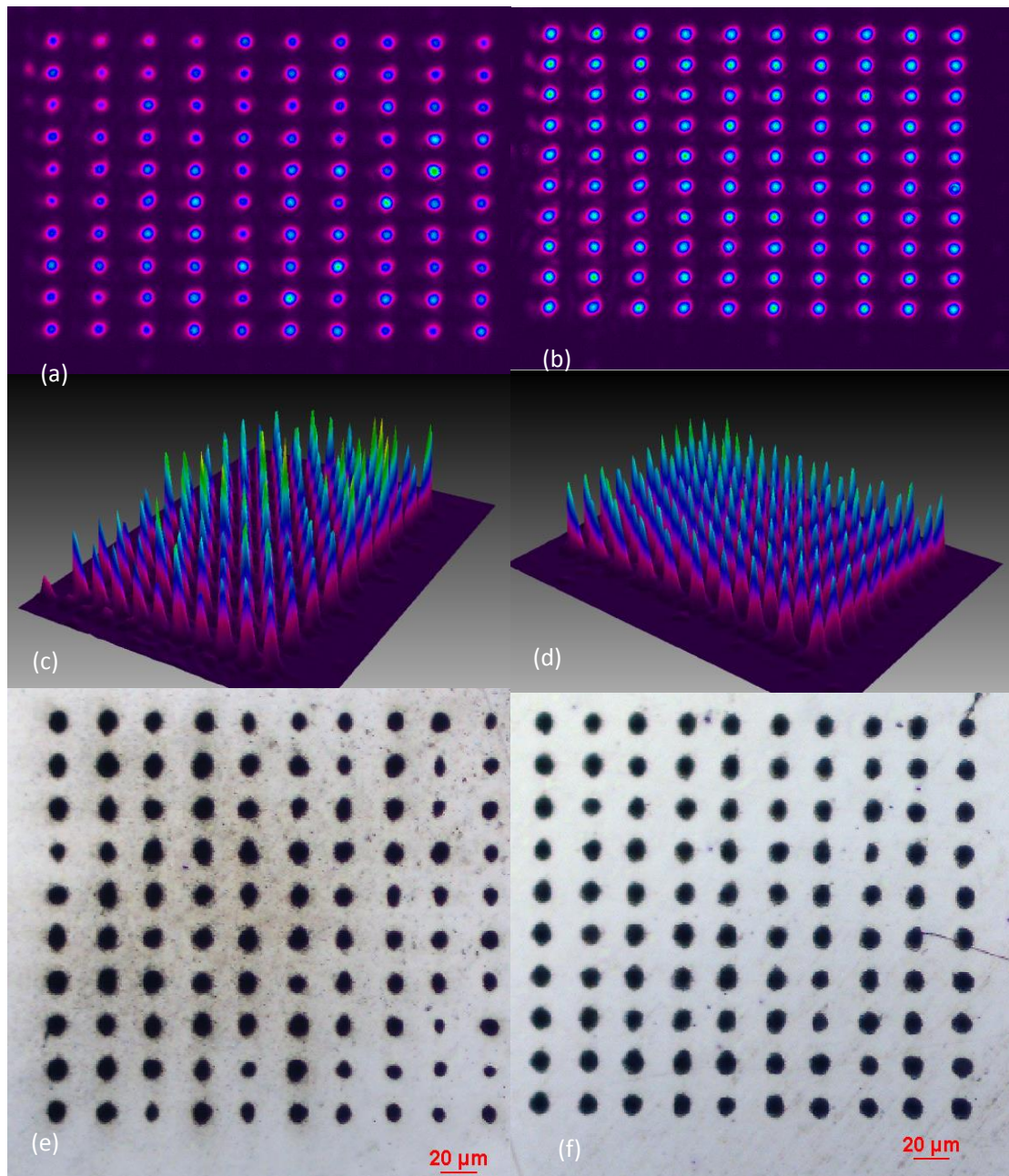


Fig.5.8.3 (a)(b) and (c)(d) illustrate the pulse energy of the 100 diffracted NIR beam array before and after optimisation both in 2D and 3D format. (e) and (f) show the surface micro-machining of a stainless steel substrate confirming the much improved micro-machining.

5.9 Discussion

In principle, a CGH optimisation system with feedback is usually slower than other methods which only consider the calculation algorithm itself and which don't need to read data from external equipment. However, the efficiency of the optimisation of static beam patterns is still fast enough to solve this problem. It optimises the uniformity of 100 beams in less than 20 seconds (about 10 iterations). Compared with other hologram optimisation mechanisms such as improving the calculating algorithm, or adding a correction for optical aberration, the feedback system in my research is more flexible and provides a more comprehensive improvement which can correct the deviation from both hologram calculation and the optical system.

For fixed beam designs, the optimised hologram can be saved for future use as long as the optical arrangement keeps as the same. The real time feedback system can also be easily applied for different laser systems. For example, this system has been successfully applied to another laser set up at 532nm in our laboratory with some basic adjustment of the setting in few minutes. The application could potentially be extended to other processing systems with SLM and monitor camera which can collect and return image information.

The optimisation of dynamic beam designs is new technique with many potential applications which need low speed real-time beam adjust and can't be achieved by pre-saved optimised holograms. However, it's inapplicable for laser processing with high speed pattern changes due to the slow calculation time, limited by

computer calculating speed and camera recording speed.

5.10 Summary

The real-time hologram optimisation system based on the camera feedback was applied to the Gerchberg Saxton Algorithm, optimising the desired holograms greatly. It was demonstrate that the feedback system improved the poor pulse energy uniformity which was also proved mainly to be related with computer calculation. the feedback system Addressed with these optimised holograms, the SLM generates multiple beams up to 100 spots with uniform pulse energy in one and 2 dimensions. For internal processing by multiple NUV femtosecond beams, the optimised parallel beams produced parallel filaments at the same depth inside PMMA with less than 2% SDM. Although the application of optimised parallel beams in producing VBGs in PMMA didn't demonstrate obvious improvement, It was proved to be valuable for surface ablation which is sensitive to pulse energy. The ablations on stainless steel by 10 X 10 optimised NIR beam array has the SDM in diameter down to 2%. In addition, with the extension of auto-tracking function, this optimisation system can also improve the energy uniformity of random dynamic multi-beam designs.

Chapter 6

Conclusions and future work

6.1 Conclusion

This thesis demonstrated the high speed inscription of 5 x5 x (1-7mm) thick, VBGs in PMMA with parallel NUV (387nm), 180fs laser beams, with linear and circular polarisations. Linear (TE) polarisation produced the highest refractive index modulation while circular produced the lowest. The observed first order diffraction efficiency and Bragg angular envelope agree well with theoretical expectations. The source of the variation in RI contrast was investigated and found to be due to polarisation dependent non-linear SF, the first such observation in a pure polymer. First order diffractive efficiency at 532nm up to 94% was achieved with linear polarisation with resulting modulation $\Delta n \sim 5.8 \times 10^{-5}$, the highest diffraction efficiency yet demonstrated in pure PMMA. Critical powers for SF were measured by observing the thresholds for white light SC generation with polarisation state. We find the ratio $P_C^{\text{lin}}/P_C^{\text{circ}} \sim 1.4 \pm 0.1$ in PMMA. This ratio is expected theoretically due to the polarisation dependent third order susceptibility χ_3 (a tensor) which has two components for linear but only one for circular polarisation [143]. This same value was essentially observed in fused silica as well. Additionally, by using spiral phase CGH's applied to an SLM combined with appropriate waveplates, vortex Azimuthal $|Az\rangle$ and radial polarisation $|Ra\rangle$ states were produced and their critical powers measured for the first time in PMMA. No significant difference between Radial and Azimuthal states was detected but had significantly higher critical powers. The ratio $P_C^{\text{Rad}}/P_C^{\text{lin}} \sim 2.0 \pm 0.2$. This higher critical power P_C^{rad} may well be partly due to the slightly increased focal spot size of the vortex states which focus to a near

Gaussian beam.

The poor pulse energy uniformity of multiple beams diffracted by the SLM in the used setup was proved to be due to the imperfect computer calculation. A camera based real-time feedback system was developed to optimise the pulse energy uniformity in parallel processing. For internal processing with 10 parallel NUV fs beams, the StdD of the filaments length was reduced from 20% to 2%. However, the optimised beams didn't improve the quality of VBGs, perhaps due to the overlapping of filaments between layers which reduce the difference of filament lengths. The SDM of pulse energy of a 10X10 NIR beam array was reduced from 90% to 2% using this system in approximately 18 seconds, creating high uniformity ablations on stainless steel. This result, by using camera based feedback, demonstrated a significant improvement in multi-beam processing with SLM. In addition, with the extension of auto-tracking function, the optimisation of dynamic random beams designs was first presented.

6.2 Recommendations for future work

In section 4.2, the time dependence of ratio $\eta_1(|V|)/\eta_1(|R|)$ (Fig.4.2-1) was incompletely investigated without the extension of the time after 9 days. The final ratio might be even lower than 1.09 after developing. Because the research was carried out for the purpose of developing a potential technique to produce device level VBGs, the study of the full range of long term time dependent effect is recommended to ensure the stability of the optical device.

Polarisation dependent filamentation and critical pulse energy for SF has been investigated in Chapter 4 with four different polarisations. The vortex azimuthal $|Az\rangle$ and radial $|Ra\rangle$ polarisations have much higher critical power than linear and circular polarisations have. The reason may be due to the lower beam quality. However, the vortex states may affect the critical power as well, which can be investigated through comparing of the critical power of $|Az\rangle$ and $|Ra\rangle$ vortex in phase states with a planar wavefront. The in-phase $|Az\rangle$ and $|Ra\rangle$ polarisations can be generated with the combination of two SLMs or a spiral wave-plate, now commercially available. It would also be interesting to investigate pure spiral phase beams with linear/circular polarisation and with Angular Optical Momentum (OAM) with $l > 1$.

The current optimization is only applicable for 1d or 2d beam arrays. It is technically possible to modify this system for a more complex 3D beam array. One approach is to use a movable lens, the function of which is to focus the beams at different depth onto the camera, controlled by a stage.

In addition, the feedback system can also be used to improve the beam quality each with precise pulse energies as desired, which are all different, extending this technique to a new application area, such as 3D data storage, step shape gratings and step shape surface ablations.

While the real-time feedback system as proved very effective, further improvement could be achieved. For example, the speed for loading image by LabView can be improved if the image from the camera can be directly loaded to

LabVIEW without the aids of Beamgate software. It saves time by avoiding saving the image in Windows by Beamgate and reading the image from windows by LabView.

References

1. Maiman, T. H. "Stimulated Optical Radiation in Ruby" *Nature*, Volume 187, Issue 4736, pp. 493-494 (1960)
2. Robert J. Wayne, Peter P. Chenausky, Carl J. Buczek "Method for cavity dumping a Q-switched laser", United States Patent number 4,176,327
3. Ewart P., "Frequency tunable, nanosecond duration pulses from flashlamp pumped dye lasers by pulsed Q-modulation" *In Optics Communications* 28(3):379-382 (1979)
4. W. Dietel, E. Döpel, D. Kühlke, B. Wilhelmi, "Pulses in the femtosecond range from a cw dye ring laser in the colliding pulse mode-locking (CPM) regime with down-chirp" *Optics Communications* 43(6):433-436 (1982)
5. F. O'Neill, "Picosecond pulses from a passively mode-locked cw dye laser" *Optics Communications* 6(4):360-363(1972)
6. A. Borot , A. Malvache, XW. Chen, A. Jullien, JP. Geindre, P. Audebert, G. Mourou, F. Quere, R. Lopez-Martens, " Attosecond control of collective electron motion in plasmas" *NATURE PHYSICS*; MAY, , 85, p416-p421(2012)
7. P.P. Pronko, S.K. Dutta, J. Squier, J.V. Rudd, D. Du, G. Mourou, "Machining of sub-micron holes using a femtosecond laser at 800nm." *Optics Communications* 114 (1-2), pp. 106-110 (1995)
8. K. M. Davis, K. Miura, N. Sugimoto, and K. Hirao, "Writing waveguides in glass with a femtosecond laser", *Opt. Lett.* 21(21), 1729–1731 (1996)
9. Ed. R Ossellame, G.Cerulloa and R.Ramponi,"Passive Photonic Devices in Glass", *Topics in Applied Physics* Vol. 123, "Fs Laser Micro-machining", p155-195 (Springer, Heidelberg) (2011)
10. W. Watanabe and K. Itoh, "Fabrication of photonic devices with femtosecond laser pulses", *Proc SPIE*, vol. 5340 pp. 119-126 (2004)

11. D. Paipulas, V. Kudriasov, K. Kurselis, M. Malinauskas, S. Ost and V. Sirutkaitis ,
“Volume Bragg grating formation in fused silica with high repetition rate femtosecond Yb:KGW laser pulses”, Proc. LPM 2010 (11th International Symposium on Laser Precision Microfabrication), June 7-10, Stuttgart, Germany. (2010)
12. C. Voigtländer, D. Richter, J. Thomas, A. Tünnermann, and S. Nolte, "Inscription of high contrast volume Bragg gratings in fused silica with femtosecond laser pulses," Appl. Phys. A-Mater. Sci. Process. 102 (1), 35-38 (2011).
13. K. Yamasaki, S. Juodkazis, T. Lippert, M. Watanabe, S. Matsuo, and H. Misawa,
“Dielectric breakdown of rubber materials by femtosecond irradiation,” Appl. Phys., A Mater. Sci. Process. 76, 325–329 (2003)
14. A.Zoubir C.Lopez, M.Richardson and K.Richardson, “Femtosecond laser fabrication of tubular waveguides in poly(methyl methacrylate)”, Opt Lett, Vol. 29, No.16, 1840-1842 (2004)
15. W. Watanabe, S. Sowa, T. Tamaki, K. Itoh and J. Nishii, “Three-Dimensional Waveguides Fabricated in Poly(methyl methacrylate) by a Femtosecond Laser”. Jap. J. Appl. Phys, Vol 45, No 29, L765 –L767 (2006)
16. K. Yamasaki, S. Juodkazis, S. Matsuo and H. Misawa, “Three-dimensional micro-channels in polymers: one step fabrication”, Appl Phys A 77, 371-373 (2003)
17. N. Uppal, P. S. Shiakolas, and M. Rizwan, “Three dimensional waveguide fabrication in PMMA using femtosecond laser micromachining system,” SPIE Symposium on MOEMS-MEMS 2008 Micro and Nanofabrication, San Jose, California, Proc. SPIE, Vol. 6882, 68820I (2008); DOI:10.1117/12.763824 (2008)
18. J. Si, J. Qiu, J. Zhai, Y. Shen and K. Hirao, “Photoinduced permanent gratings inside bulk azodye-doped polymers by the coherent field of a femtosecond laser,” Appl. Phys. Lett. 80, 359-361 (2002).
19. P.J. Scully, D. Jones and D.A. Jaroszynski, “Femtosecond laser irradiation of

- polymethylmethacrylate for refractive index gratings". *J.Opt.A, Pure Appl. Opt.* 5, S92-S96 (2003)
20. H. Mochizuki, W. Watanabe, R. Ezoe, T. Tamaki, Y. Ozeki, K. Itoh, M. Kasuya, K. Matsuda, S. Hirono, "Density characterization of femtosecond laser modification in polymers", *Appl. Phys. Lett.* 92, no. 9, pp. 091120,(2008).
21. Alexandra Baum, Patricia J. Scully, Walter Perrie, David Jones, Riju Issac, and Dino A. Jaroszynski "Pulse duration dependency of femtosecond laser refractive index modification in poly(methyl methacrylate)", *Optics Letters*, Vol. 33, Issue 7, 651-653,(2008)
22. W. Watanabe, "Femtosecond filamentary modifications in bulk polymer materials", *Laser Phys.* 19, no. 2, pp. 342-345,(2009).
23. A. Zakery , S.R. Elliott, "Optical Nonlinearities in Chalcogenide Glasses and their Applications", IX, 202p, Hardcover. ISBN: 978-3-540-71066-0 (2007)
24. M. D. Feit and A. M. Rubenchik, "Influence of Subsurface Cracks on Laser Induced Surface Damage", *PIE Boulder Damage Symposium XXXV Annual Symposium on Optical Materials for High Power Lasers*, Boulder, CO (US), 09/22/2003--09/24/2003
25. H. D. Jones and H. R. Reiss, "Intense-field effects in solids," *Phys. Rev. B* 16, 2466 (1977)
26. L. V. Keldysh, "Ionization in the field of a strong electromagnetic wave," *Sov. Phys. JETP* 20, 1307 (1965)
27. B. Rethfeld, "Unified Model for the Free-Electron Avalanche in Laser-Irradiated Dielectrics," *Phys. Rev. Lett* 92, 187401 (2004)
28. Y. Peng, Y. Wei, and Z. LV, "Femtosecond laser-induced damage in dielectrics," *Opt. Appl.* XXXIV(2004).
29. A. P. Joglekar, H.h. Liu, E. Meyhofer, G. Mourou, and A. J. Hunt, "Optics at critical intensity: Applications to nanomorphing," *P Natl. Acad. Sci. USA* 101, 5856 (2004).

30. E.N. Glezer, M. Milosavljevic, L. Huang, R.J. Finlay, T.-H. Her, J.P. Callan, E. Mazur, "Three-dimensional optical storage inside transparent materials." *Opt. Lett.* 21, 2023 (1996)
31. G. Zhou, M.J. Ventura, M.R. Vanner, M. Gu, "Use of ultrafast-laser driven microexplosion for fabricating three-dimensional void based diamond-lattice photonic crystals in a solid polymer material." *Opt. Lett.* 29, 2240 (2004)
32. J. Song, X. Wang, X. Hu, J. Xu, Y. Liao, H. Sun, J. Qiu, Z. Xu, "Orientation-controllable self-organized microgratings induced in the bulk SrTiO₃ crystal by a single femtosecond laser beam." *Opt. Express* 15, 14524 (2007)
33. A. Martinez, M. Dubov, I. Khrushchev, I. Bennion, "Direct writing of fibre Bragg gratings by femtosecond laser," *Electron. Lett.* 40 1170–1172. (2004)
34. A.M. Streltsov, N.F. Borrelli, "Fabrication and analysis of a directional coupler written in glass by nanojoule femtosecond laser pulses," *Opt. Lett.* 26 (2001)
35. A. Baum, P. J. Scully, M. Basanta, C. L. Paul Thomas, P. R. Fielden, N. J. Goddard, W. Perrie, and P. R. Chalker, "Photochemistry of refractive index structures in poly(methyl methacrylate) by femtosecond laser irradiation," *Opt. Lett.* 32, 190 (2007).
36. J. W. Chan, T. Huser, S. Risbud, and D. M. Krol, "Structural changes in fused silica after exposure to focused femtosecond laser pulses," *Opt. Lett.* 26, 1726 (2001).
37. C. B. Schaffer, A. Brodeur, J. F. García, and E. Mazur, "Micromachining bulk glass by use of femtosecond laser pulses with nanojoule energy," *Opt. Lett.* 26, 93 (2001).
38. A. M. Streltsov and N. F. Borrelli, "Study of femtosecond-laser-written waveguides in glasses," *J. Opt. Soc. Am. B* 19, 2496 (2002).
39. B. D. Strycker, M. Springer, C. Trendafilova, X. Hua, M. Zhi, A. A. Kolomenskii, H. Schroeder, J. Strohaber, H. A. Schuessler, G. W. Kattawar, and A. V. Sokolov, "Energy transfer between laser filaments in liquid methanol" *OPTICS LETTERS*, 37 1, p16-p18, JAN 1, (2012)

40. Tie-Jun Wang, Jingjing Ju, Jean-Francois Daigle, Shuai Yuan, Ruxin Li and See Leang Chin, "Self-seeded forward lasing action from a femtosecond Ti:sapphire laser filament in air", *Laser Phys. Lett.* 10 125401 (2013)
41. A. Brodeur and S.L. Chin, "Band-Gap Dependence of the Ultrafast White-Light Continuum", *Phys. Rev. Lett.* Vol.80, No.20, (1998)
42. A. Couairon, E. Gaizauskas, D. Faccio, A. Dubietis and P. Di Trapani, "Nonlinear X-wave formation by femtosecond filamentation in Kerr media", *Physical Review E* 73, 016608 (2006)
43. A. Salimnia, N. Nguyen, S. Chin, and R. Vallée, "The influence of self-focusing and filamentation on refractive index modifications in fused silica using intense femtosecond pulses," *Opt. Commun.* 241, 529 (2004).
44. Dun LIU, Walter PERRIE, Zheng KUANG, P. J. SCULLY, A. BAUM, S. LIANG, A. TARANU, S. P. EDWARDSON, E. FEARON, G. DEARDEN, and K. G. ATKINS, "Multiple Beam Internal Structuring of PMMA" *Proceedings of LAMP* (2009)
45. D. Liu, Z. Kuang, W. Perrie, P. J. Scully, A. Baum, S. P. Edwardson, E. Fearon, G. Dearden, K. G. Watkins, "High-speed uniform parallel 3D refractive index micro-structuring of poly(methyl methacrylate) for volume phase gratings" *Applied Physics B* 101(4):817-823. (2010)
46. A. Salimnia, N. Nguyen, M. Nadeau, S. Petit, S. Chin, and R. Vallee, "Writing optical waveguides in fused silica using 1 kHz femtosecond infrared pulses," *J. Appl. Phys.* 93, 3724 (2003).
47. S. Eaton, H. Zhang, P. Herman, F. Yoshino, L. Shah, J. Bovatsek, and A. Arai, "Heat accumulation effects in femtosecond laser-written waveguides with variable repetition rate," *Opt. Express* 13, 4708 (2005).
48. T. Tamaki, W. Watanabe, H. Nagai, M. Yoshida, J. Nishii, and K. Itoh, "Structural modification in fused silica by a femtosecond fiber laser at 1558 nm," *Opt. Express* 14, 6971 (2006).
49. K. Itoh, "Nano- and microprocessing in glass using fs laser," *Proc. of SPIE* 4830, 550 (2003).

50. K. Yamada, W. Watanabe, T. Toma, K. Itoh, and J. Nishii, "In situ observation of photoinduced refractive-index changes in filaments formed in glasses by femtosecond laser pulses," *Opt. Lett.* 26, 19 (2001).
51. H. Guo, H. Jiang, Y. Fang, C. Peng, H. Yang, Y. Li, and Q. Gong, "The pulse duration dependence of femtosecond laser induced refractive index modulation in fused silica," *J. Opt. A: Pure Appl. Opt.* 6, 787 (2004)
52. J. Liesener, M. Reicherter, T. Haist, and H. J. Tiziani, "Multi-functional optical tweezers using computer-generated holograms," *Opt. Commun.* 185, 77 (2000).
53. S. Onda, W. Watanabe, K. Yamada, K. Itoh, and J. Nishii, "Study of filamentary damage in synthesized silica induced by chirped femtosecond laser pulses," *J. Opt. Soc. Am. B* 22, 2437-2443 (2005).
54. R. Osellame, N. Chiodo, G. D. Valle, S. Taccheo, R. Ramponi, G. Cerullo, A. Killi, U. Morgner, M. Lederer, and D. Kopf, "Optical waveguide writing with a diode-pumped femtosecond oscillator," *Opt. Lett.* 29, 1900- 1902 (2004).
55. R. Gattass and E. Mazur, "Femtosecond laser micromachining in transparent materials," *Nat. Photonics* 2, 219 (2008).
56. Kazuhiro YAMADA, Wataru WATANABE, Kenji KINTAKA, Junji NISHII and Kazuyoshi ITOH, "Volume Grating Induced by a Self-Trapped Long Filament of Femtosecond Laser Pulses in Silica Glass", *Jpn. J. Appl. Phys.* Vol. 42 pp. 6916–6919 (2003)
57. C. Hnatovsky, R. S. Taylor, E. Simova, V. R. Bhardwaj, D. M. Rayner, and P. B. Corkum, "High-resolution study of photon induced modification in fused silica produced by a tightly focused femtosecond laser beam in the presence of aberrations", *JOURNAL OF APPLIED PHYSICS* 98, 013517 (2005)
58. D. Liu, Y. Li, R. An, Y. Dou, H. Yang, Q. Gong, "Influence of focusing depth on the microfabrication of waveguides inside silica glass by femtosecond laser direct writing", *Appl. Phys. A* 84, 257–260 (2006)
59. Shijie Liang, Patricia J. Scully, Joerg Schille, John Vaughan, Mohammed Benyazzar, Dun Li and Walter Perrie, "Writing Parameters for 3D Refractive

- Index Structures in Polymethyl Methacrylate Using Femtosecond Radiation at 400 nm”, JLMN-Journal of Laser Micro/Nanoengineering Vol. 5, No. 1, (2010)
60. A. Baum, P. Scully, W. Perrie, M. Sharp, K. Watkins, D. Jones, R. Issac, and D. Jaroszynski, "NUV and NIR Femtosecond Laser Modification of PMMA," in LPM2007-the 8th International Symposium on Laser Precision Microfabrication, (2007)
61. W. Yang, P. Kazansky, and Y. Svirko, "Non-reciprocal ultrafast laser writing," Nat. Photonics 2, 99 (2008).
62. Dun Liu, "Femtosecond laser internal structuring of transparent materials using a spatial light modulator" University of Liverpool. Thesis (2011)
63. Chan J W, Huser T R, Risbud S H, Hayden J S and Krol D M, "Waveguide fabrication in phosphate glasses using femtosecond laser pulses", Appl. Phys. Lett. 82 2371, (2003)
64. Minoshima K, Kowalewicz A M, Hartl I, Ippen E P and Fujimoto, "Photonic device fabrication in glass by use of nonlinear materials processing with a femtosecond laser oscillator" Opt. Lett. 26 1516 (2001)
65. Y. Li, W. Watanabe, K. Itoh, and X. Sun, "Holographic data storage on nonphotosensitive glass with a single femtosecond laser pulse", Appl. Phys. Lett. Vol. 81, 1952(2002).
66. Chen Y, Sugioka K, Midorikawa K, Masuda M, Toyoda K, Kawachi M and Shihoyama K, "Three-dimensional micro-optical components embedded in photosensitive glass by a femtosecond laser", Opt. Lett. 28 1144 (2003)
67. J. A. Arns, W.C.Colburn and S.C. Barden, " Volume phase gratings for spectroscopy ultrafast laser compressors and wavelength division multiplexing" ,Proc. SPIE Vol. 3779, p313-323 (1999)
68. B. L. Volodin, S. V. Dolgy, E. D. Melnik, E. Downs, J. Shaw, and V. S. Ban, "Wavelength stabilization and spectrum narrowing of high-power multimode laser diodes and arrays by use of volume Bragg gratings," Opt. Lett. 29(16), 1891-1893 (2004)

69. A.L.Glebov, O.Mokhun, A.Rapaport, S.Vergnole, V.Smirnov and L.B.Glebov, "Volume Bragg gratings as ultra-narrow and multiband optical filters," Proc. SPIE Vol. 8428, 84280C, p1-11
70. M. Pasienski and B. Demarco, "A high-accuracy algorithm for designing arbitrary holographic atom traps," Opt. Express 16, 2176 (2008).
71. T. A. Shankoff, "Phase holograms in dichromated gelatin", Applied Optics 7, pp. 2101-2105, (1968)
72. O.M.Efimov, L.B.Glebov, L.N.Glebova, K.C.Ricahrdson and V.I.Smirnov, "high-efficiency bragg gratings in photothermorefractive glass", Appl. Opt. vol. 38(4) pp. 619-627, (Feb. 1999).
73. I.G. Ciapurin, L.B. Glebov, L.N. Glebova, V.I. Smirnov, E.V. Rotari, "Incoherent combining of 100-W Yb-fiber laser beams by PTR Bragg grating," Proc. SPIE 4974,209-219 (2003).
74. H. Kogelnik, "Coupled wave theory for thick hologram gratings," Bell Syst. Tech. J. 48, 2909 (1969).
75. M. G. Moharam, T. K. Gaylord, and R. Magnusson, "Criteria for Raman-Nath regime diffraction by phase gratings," Opt. Commun. 32, 19 (1980).
76. R. Osellame, S. Taccheo, M. Marangoni, R. Ramponi, P. Laporta, D. Polli, S. De Silvestri, and G. Cerullo, "Femtosecond writing of active optical waveguides with astigmatically shaped beams," J. Opt. Soc. Am. B 20, 1559 (2003).
77. Fei He, Haiyi Sun, Min Huang, Jian Xu, Yang Liao, Zenghui Zhou, Ya Cheng, Zhizhan X, Koji Sugioka, Katsumi Midorikawa, "Rapid fabrication of optical volume gratings in Foturan glass by femtosecond laser micromachining", Appl Phys A 97: 853–857 (2009)
78. K.-i. Kawamura, N. Sarukura, M. Hirano, and H. Hosono, "Holographic Encoding of Permanent Gratings Embedded in Diamond by Two Beam Interference of a Single Femtosecond Near-Infrared Laser Pulse," Jpn. J. Appl. Phys. 39, L767 (2000).
79. Christian Voigtländer, Daniel Richter, Jens Thomas, Andreas Tünnermann,

- Stefan Nolte, "Inscription of high contrast volume Bragg gratings in fused silica with femtosecond laser pulses" *Appl Phys A* 102: 35–38 (2011)
80. S. Hasegawa and Y. Hayasaki, "Holographic femtosecond laser processing by use of a spatial light modulator," *Proc. SPIE* 6458, 645815 (2007)+
81. D.Liu, W.Perric, Z.Kuang, P.J.Scully, A. Baum, S,Liang, S.P.Edwardson, E.Fearon, G.Dearden and K.G.Watkins, "Multi-beam second-harmonic generation in beta barium borate with a spatial light modulator and application to internal structuring in poly(methyl methacrylate)," *Appl.Phys.B* 107, 795-801, (2012)
82. U. Efron, "Spatial light modulators for optical computing and information processing," *System Sciences* 1, 416 (1989).
83. Y. Kozawa and S. Sato, "Optical trapping of micrometer-sized dielectric particles by cylindrical vector beams," *Opt. Express* 18, 10828 (2010).
84. J. Leach, G. Sinclair, P. Jordan, J. Courtial, M. Padgett, J. Cooper, and Z. Laczik, "3D manipulation of particles into crystal structures using holographic optical tweezers," *Opt. Express* 12, 220 (2004).
85. G. Sinclair, J. Leach, P. Jordan, G. Gibson, E. Yao, Z. Laczik, M. Padgett, and J. Courtial, "Interactive application in holographic optical tweezers of a multi-plane Gerchberg-Saxton algorithm for three-dimensional light shaping," *Opt. Express*, 12, 1665 (2004).
86. B. Sun, Y. Roichman, and D. Grier, "Theory of holographic optical trapping," *Opt. Express* 16, 15765 (2008).
87. N. Huot, N. Sanner, and E. Audouard, "Programmable focal spot shaping of amplified femtosecond laser pulses and their application to micromachining," *Proc. SPIE* 6400, 64000K (2006).
88. N. Sanner, N. Huot, E. Audouard, C. Larat, and J. Huignard, "Spatial beam shaping of femtosecond laser pulses application to micromachining and photowriting," *Lasers and Electro-Optics, 2005.(CLEO). Conference on* 3 (2005).
89. N. Sanner, N. Huot, E. Audouard, C. Larat, and J. Huignard, "Direct ultrafast

- laser micro-structuring of materials using programmable beam shaping," *Opt. Lasers Eng.* 45, 737 (2007).
90. N. Sanner, N. Huot, E. Audouard, C. Larat, J. Huignard, and B. Loiseaux, "Programmable focal spot shaping of amplified femtosecond laser pulses," *Opt. Lett.* 30, 1479 (2005).
91. A. Jesacher and M. J. Booth, "Parallel direct laser writing in three dimensions with spatially dependent aberration correction," *Opt. Express* 18, 21090 (2010).
92. C. Mauclair, A. Mermillod-Blondin, N. Huot, E. Audouard, and R. Stoian, "Ultrafast laser writing of homogeneous longitudinal waveguides in glasses using dynamic wavefront correction," *Opt. Express* 16, 5481 (2008).
93. Z. Kuang, W. Perrie, J. Leach, M. Sharp, S. Edwardson, M. Padgett, G. Dearden, and K. Watkins, "High throughput diffractive multi-beam femtosecond laser processing using a spatial light modulator," *Appl. Surf. Sci.* 255, 2284 (2008).
94. Z. Kuang, D. Liu, W. Perrie, S. Edwardson, M. Sharp, E. Fearon, G. Dearden, and K. Watkins, "Fast parallel diffractive multi-beam femtosecond laser surface micro-structuring," *Appl. Surf. Sci.* 255, 6582 (2009).
95. D. Liu, Z. Kuang, S. Shang, W. Perrie, D. Karnakis, A. Kearsley, M. Knowles, S. Edwardson, G. Dearden, and K. Watkins, "Ultrafast parallel laser processing of materials for high throughput manufacturing," in *LAMP2009 - the 5th International Congress on Laser Advanced Materials Processing*, (2009),
96. Z. Kuang, W. Perrie, D. Liu, S. Edwardson, J. Cheng, G. Dearden, and K. Watkins, "Diffractive multi-beam surface micro-processing using 10ps laser pulses," *Appl. Surf. Sci.* 255, 9040 (2009).
97. R. W. Gerchberg and O. Saxton, "A practical algorithm for the determination of the phase from image and diffraction plane pictures," *Optik* 35, 237 (1972).
98. R. Di Leonardo, F. Ianni, and G. Ruocco, "Computer generation of optimal holograms for optical trap arrays," *Opt. Express* 15, 1913 (2007).
99. J. E. Curtis, B. A. Koss, and D. G. Grier, "Dynamic holographic optical

- tweezers," *Opt. Commun.* 207, 169 (2002). J. Bengtsson, "Kinoform design with an optimal-rotation-angle method," *Appl. Opt.* 33, 6879 (1994).
100. S. Hasegawa and Y. Hayasaki, "Holographic Femtosecond Laser Processing with Multiplexed Phase Fresnel Lenses Displayed on a Liquid Crystal Spatial Light Modulator," *Opt. Rev.* 14, 208 (2007).
101. T. Haist, M. Schönleber and H. J. Tiziani, "Computer-generated holograms from 3D-objects written on twisted-nematic liquid crystal displays," *Optics Communications* 140 299-308 (1997)
102. F. D'Amore, M. Lanata, S.M. Pietralunga, M.C. Gallazzi and G. Zerbi, "Enhancement of PMMA nonlinear optical properties by means of a quinoid molecule" *Opt. Mat.* 24, 661-665 (2004)
103. Yoshio Hayasaki, Takashi Sugimoto, Akihiro Takita, and Nobuo Nishida, "Variable holographic femtosecond laser processing by use of a spatial light modulator," *APPLIED PHYSICS LETTERS* 87, 031101(2005)
104. Satoshi Hasegawa, Yoshio Hayasaki, and Nobuo Nishida, "Holographic femtosecond laser processing with multiplexed phase Fresnel lenses," *OPTICS LETTERS* Vol. 31, No. 11 1705 (2006)
105. H. Takahashi, S. Hasegawa, and Y. Hayasaki, "Holographic femtosecond laser processing using optimal-rotation-angle method with compensation of spatial frequency response of liquid crystal spatial light modulator" *Appl. Opt.* 46, 5917 (2007)
106. Dong Wang, Jian Zhang, Yang Xia and Hao Wang, "generation of spots in the 3D space domain with computer generated holograms written on a phase-only liquid crystal spatial light modulator" *J. Opt.* 14 105704 (10pp) (2012)
107. Roberto Di Leonardo, Francesca Ianni, Giancarlo Ruocco, "Computer generation of optimal holograms for optical trap arrays", Vol. 15, No. 4 / *OPTICS EXPRESS* 1913 19 February (2007)
108. M. Montes-Usategui, E. Pleguezuelos, J. Andilla, E. Martín-Badosa, "Fast

- generation of holographic optical tweezers by random mask encoding of Fourier components," *Opt. Express* 14, 2101–2107, (2006).
109. M. Reicherter, T. Haist, E.U. Wagemann, H.J. Tiziani, "Optical particle trapping with computer-generated holograms written on a liquid-crystal display," *Opt. Lett.* 24, 608-610 (1999).
 110. J. Liesener, M. Reicherter, T. Haist, H.J. Tiziani, "Multi-functional optical tweezers using computer-generated holograms," *Opt. Commun.* 185, 77-82 (2000).
 111. J.E. Curtis, C.H.J. Schmitz, J.P. Spatz, "Symmetry dependence of holograms for optical trapping," *Opt. Lett.* 30, 2086-2088 (2005).
 112. T. Haist, M. Schönleber, H.J. Tiziani, "Computer-generated holograms from 3D-objects written on twisted nematic liquid crystal displays," *Opt. Commun.* 140, 299-308 (1997).
 113. R.A. Fox, R.M. Kogan and E.J. Robinson, "Laser Triple-Quantum Photoionization of Cesium" *Phys. Rev. Lett.*, Vol.26, No.3, 1416, (1971)
 114. J. Curtis, B.A. Koss, D.G. Grier, "Dynamic holographic optical tweezers," *Opt. Commun.* 207, 169-175, (2002).
 115. M. Meister and R. J. Winfield, "Novel approaches to direct search algorithms for the design of diffractive optical elements," *Opt. Commun.* 203, 3949 (2002).
 116. M. Polin, K. Ladavac, S.H. Lee, Y. Roichman, D. Grier, "Optimized holographic optical traps," *Opt. Express* 13, 5831-5845, (2005).
 117. J. Curtis, C. Schmitz, and J. Spatz, "Symmetry dependence of holograms for optical trapping," *Opt. Lett.* 30, 2086 (2005).
 118. Uri Mahlab, Joseph Rosen, and Joseph Shamir, "Iterative generation of complex reference functions in a joint-transform correlator", *OPTICS LETTERS* / Vol. 16, No. 5 / March 1, (1991)
 119. Satoshi Hasegawa and Yoshio Hayasaki, "Second-harmonic optimization of computer-generated hologram" August 1, 2011 / Vol. 36, No. 15 / *OPTICS*

LETTERS

120. P. B. Corkum, Claude Rolland, and T. Srinivasan-Rao, "Supercontinuum Generation in Gases" *Phys. Rev. Lett.* 57, 2268–2271 (1986).
121. Alfano, R.R. Shapiro, S.L. "Emission in the region 4000 to 7000 via four-photon coupling in glass" *Physical Review Letters*, , 24(11):584-587 (1970)
122. R. L. Fork, C. V. Shank, C. Hirlimann, R. Yen, and W. J. Tomlinson, "Femtosecond white-light continuum pulses" *Optics Letters*, Vol. 8, Issue 1, pp. 1-3 (1983)
123. R. L. Fork, B. I. Greene, and C. V. Shank, Generation of optical pulses shorter than 0.1 psec by colliding pulse mode locking, *App. Phys. Lett.* 38, 671–672 (1981).
124. P. B. Corkum, Claude Rolland, and T. Srinivasan-Rao, "Supercontinuum Generation in Gases" *Phys. Rev. Lett.* 57, 2268 3 November (1986)
125. M. Bradler , P. Baum , E. Riedle , "Femtosecond continuum generation in bulk laser host materials with sub- μ J pump pulses" *Appl Phys B* 97: 561–574 (2009)
126. T. Imran, G. Figueira, "Efficient white-light continuum generation in transparent solid media using \sim 250 fs, 1053 nm laser pulses *Opportunities and technological Issues of the Extreme Light Infrastructure: LEI 2009*
127. G .Yang, Y.R. Shen, "Spectral broadening of ultrashort pulses in a nonlinear medium", *Opt. Lett.* 9, 510-512 (1984).
128. A.Brodeur and S.L.Chin," Band-Gap Dependence of the Ultrafast White-Light Continuum" *Phys.Rev.Lett.* Vol.80, No.20, (1998)
129. .Zakery A. ,Elliott S.R., *Optical Nonlinearities in Chalcogenide Glasses and their Applications*, , IX, 202p, Hardcover. ISBN: 978-3-540-71066-0 (2007)
130. Fujio Shimizu, "Frequency Broadening in Liquids by a Short Light Pulse" *Phys. Rev. Lett.* 19, 1097 – Published 6 November (1967)

131. N. N. Il'ichev, V. V. Korobkin, V. A. Korshunov, A. A. Malyutin, T. G. Okroashvili, and P. P. Pashinin, , *Pis'ma Zh. Eksp. Teor. Fiz.* 15, 191–194 (1972) [*JETP Lett.* 15, 133–135 (1972)]
132. Smith WL, Liu P, Bloembergen N, “Optical characteristics of supercontinuum generation” *Phys. Rev. A* 15 2396 (1977)
133. Gawelda.W, Puerto. D, Siegel. J, Ferrer. A, De La Cruz, A.R.Fernández, H, “Ultrafast imaging of transient electronic plasmas produced in conditions of femtosecond waveguide writing in dielectrics” *Applied Physics Letters*, 93(12) (2008)
134. P. L. Kelley, “Self-focusing of Optical Beam”, *Physics review letter*, Vol. 15, No. 26 P.1005 (1965)
135. J. H. MARBURGER, “SELF-FOCUSING: THEORY *Prog. Quant. Electr.*, Vol. 4, pp. 35-110. Pergamon Press, (1975)
136. E. L. Dawes, J. H. Marburge, “Computer Studies in Self-Focusing”, *PHYSICAL REVIEW VOLUME 179, NUMBER 3 15 MARCH* (1969)
137. A. Couairon, L. Sudrie, M. Franco, B. Prade, and A. Mysyrowicz, “Filamentation and damage in fused silica induced by tightly focused femtosecond laser pulses” *PHYSICAL REVIEW B* 71, 125435 s (2005)
138. M. Durand, A. Jarnac, A. Houard, Y. Liu, S. Grabielle, N. Forget, A. Dure'cu, A. Couairon, and A. Mysyrowicz, “Self-Guided Propagation of Ultrashort Laser Pulses in the Anomalous Dispersion Region of Transparent Solids: A New Regime of Filamentation, *PHYSICAL REVIEW LETTERS* , PRL 110, 115003 (2013)
139. D. C. Benito, D. M. Carberry, S. H. Simpson, G. M. Gibson, M. J. Padgett, J. G. Rarity, M. J. Miles, and S. Hanna, Constructing 3D crystal templates for photonic band gap materials using holographic optical tweezers, *Opt. Express* 17, 13005-13015 (2008)
140. J. A. Grieve, A. Ulcinas, S. Subramanian, G. M. Gibson, M. J. Padgett, D. M. Carberry, and M. J. Miles, Hands-on with optical tweezers: a multitouch interface for holographic optical trapping, *Opt. Express* 17, 3595-3602 (2009)

141. I. V. Ciapurin, L. B. Glebov, and V. I. Smirnov, "Modeling of Gaussian beam diffraction on volume Bragg gratings in PTR glass," Proc. of SPIE 5742, 183 (2005).
142. S.Tzortzakis, D.G.Papazoglou and I.Zergioti, "Long-range filamentary propagation of sub-picosecond ultraviolet laser pulses in fused silica" Opt.Lett. Vol.31, No.6,796-798 (2006)
143. R.W.Boyd, "Nonlinear Optics" (third edition), Ch.4, 207-252 (Academic press, Burlington MA, Elsevier (2008)
144. R.W.Boyd and G.L.Fischer," Nonlinear Optical Materials", Encyclopedia of Materials; Science and Technology p6237-6244 (Copyright Elsevier Science Ltd), 2001
145. R.M.Kogan, R.A.Fox, G.T.Burnham and E.J.Robinson, Bull. "Two-photon ionization of cesium "Amer. Phys. Soc. 16,1411 (1971)
146. S.Klarsfeld and A.Maquet, "Circular versus linear polarization in multiphoton ionization", Phys.Rev.Lett., Vol.29,No.2, (1972)
147. H.R.Reiss, "Polarization effects in high-order multiphoton ionization", Phys.Rev.Lett, Vol.29, No.17 1129-1131 (1972)
148. D.D.Venable and R.B.Kay, "Polarization effects in four-photon conductivity in quartz ", Appl.Phys.Lett. Vol.27, No.1, 48 (1975)
149. H.S.Carman and R.N.Compton, J.Chem. "High-Order Multiphoton Ionization Photoelectron Spectroscopy of Nitric Oxide," Phys. 90, (3) 1307 (1989)
150. V.V.Temnov, K.Sokolowski-Tinten, P.Zhou, A.El-Khamhawy and D.von der Linde, "Multiphoton Ionization in Dielectrics: Comparison of Circular and Linear Polarization," Phys. Rev. Lett. 97, 237403 (2006)
151. D.J.Little, M. Ams, P. Dekker, G.D.Marshall, J.M.Dawes and M.J.Withford, "Femtosecond laser modification of fused silica: the effect of writing

polarization on Si-O ring structure." Opt. Express Vol.16, No.24, 20029 (2008)